CHALMERS

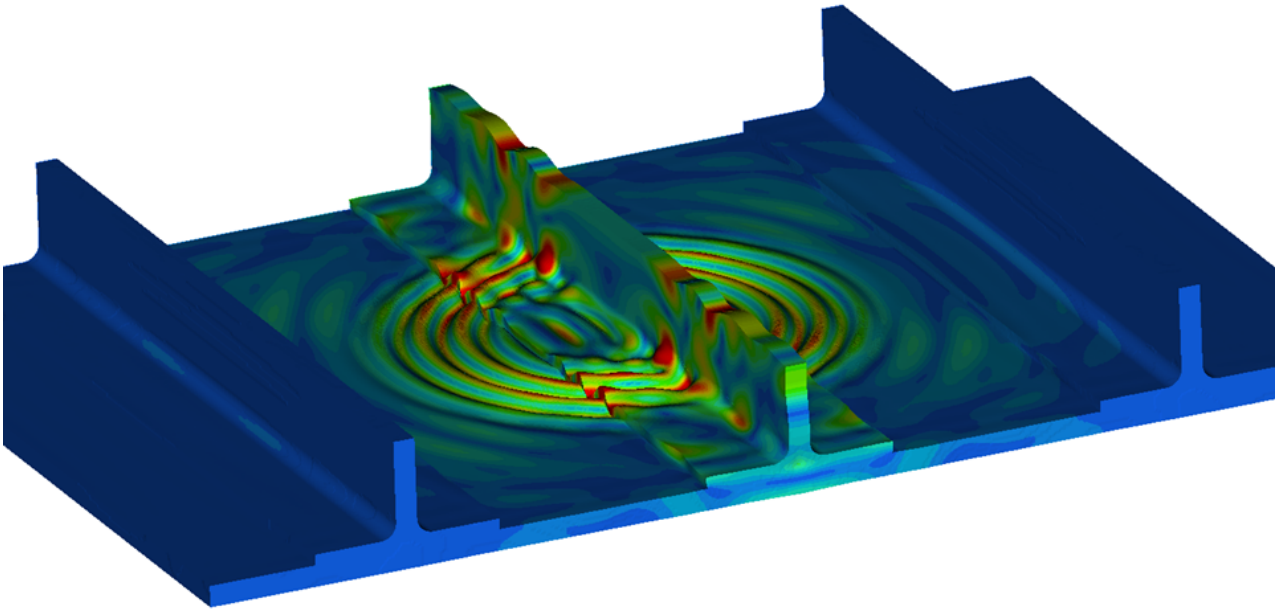

Structural Health Monitoring for Aerospace Composite Structures - an Investigation of the Potential Using the Finite Element Method

Master's thesis in Applied Mechanics

FREDRIK SLÄTTE
KRISTOFER JOVANOV

Department of Applied Mechanics
Division of Structural Dynamics
CHALMERS UNIVERSITY OF TECHNOLOGY
Gothenburg, Sweden 2012
Master's thesis 2012:61

MASTER'S THESIS IN APPLIED MECHANICS

Structural Health Monitoring for Aerospace Composite Structures - an Investigation of the Potential Using the Finite Element Method

FREDRIK SLÄTTE
KRISTOFER JOVANOV

Department of Applied Mechanics
Division of Structural Dynamics
CHALMERS UNIVERSITY OF TECHNOLOGY
Gothenburg, Sweden 2012

Structural Health Monitoring for Aerospace Composite Structures - an Investigation of the Potential Using the Finite Element Method
FREDRIK SLÄTTE
KRISTOFER JOVANOV

Master's thesis 2012:61
ISSN 1652-8557
Department of Applied Mechanics
Division of Structural Dynamics
Chalmers University of Technology
SE-412 96 Gothenburg
Sweden
Telephone: +46 (0)31-772 1000

Cover:
Ultrasonic wave propagation in a 3D finite element T-shaped stringer with the excitation frequency 100 kHz.

Chalmers Reproservice
Gothenburg, Sweden 2012

Structural Health Monitoring for Aerospace Composite Structures - an Investigation of the Potential Using the Finite Element Method
Master's thesis in Applied Mechanics
FREDRIK SLÄTTE
KRISTOFER JOVANOV
Department of Applied Mechanics
Division of Structural Dynamics
Chalmers University of Technology

Abstract

The growing demand of light-weight structures in the aerospace industry has made composites highly desirable. Real-time updates of the structural integrity can be achieved by a completely elaborated Structural Health Monitoring system. However, the inherent anisotropy of composites renders a mechanical behaviour that is difficult to predict. Hence an investigation has been performed in which the potential of Structural Health Monitoring for aerospace composite structures is evaluated by using the Finite Element Method.

The work is focused on an aerospace stringer component in a frequency range of 50 Hz – 1 MHz. In order to gain fundamental knowledge of the dynamic response for both high and low frequencies, a case study has been formulated based on a composite plate. Three different FE plate models were established and evaluated by their corresponding Lamb wave dispersion curves. Dispersion characteristics were obtained numerically for the composite plate by the Spectral Decomposition Technique and the Zero-Crossing Technique. Modelling issues and damage detection techniques were analysed, giving valuable input to the stringer modelling procedure. For the stringer, a sensitivity analysis has been carried out from which observations displayed how different defect types affect the structural behaviour. Conclusions were made for damage detection possibilities in terms of damage type and excitation/measurement configurations. In addition, the potential of time reversal imaging has been investigated. Different parameters contributions to multiple scattering were studied and how these parameters affected the spatial resolution.

Damage detection possibilities in the stringer proved to be substantial. As expected, a complex wave propagation pattern was observed due to complex geometric and material stringer properties. The sensitivity analysis showed that for all tested damage types, damage detection was possible, in particular for delaminations and inclusions. However the excitation and measurement positions had large influence on damage detectability. The concept of time reversal imaging shows great potential for model based damage detection. The location of damage can be pin-pointed with varying spatial resolution depending on (1) damage type, (2) TRM size, (3) TRM positioning and (4) length of the simulation.

A Structural Health Monitoring system possess the ability of damage detection and localization as long as the placement of the sensors are thoroughly motivated. Thus combining the results from the sensitivity and the time reversal imaging analysis ought to be given priority in future developments of Structural Health Monitoring systems when based on these concepts.

Keywords: Structural Health Monitoring, Lamb waves, Delamination, Finite Element Method, Composite modelling, Sensitivity analysis, Damage detection, Time reversal imaging

Acknowledgements

There is a saying: "Education is what remains after one has forgotten everything he learned in school". With this master thesis finished we find ourselves in a point in life where a lot has been accomplished, yet more is to be accomplished. We have spent several years together at Chalmers University of Technology, spending late nights in the classrooms before the exams, finishing assignments in the computer "dungeons" and enjoying coffee breaks with our friends. Our time at Chalmers has undoubtedly been challenging, but we both believe that the real challenges lie ahead. We both share keen interests in the aerospace industry and are convinced that the industry must adopt major changes in order to reach the requirements for a sustainable future. Needless to say, (1) reducing carbon-dioxide emissions, (2) removing disturbing noise and (3) ensuring the safety of the passengers are only a few objectives that must be dealt with. We are aware that these tasks can not bear fruit overnight and enormous efforts must be made on a global level. However, we are both ready to contribute and do our utmost to engage ourselves in careers that can counter these problems.

The opportunity to carry out our thesis at Creo Dynamics AB has provided us with new insights in the aerospace industry. Not only have we had the privilege to work among brilliant engineers, but we have also found that our ambitions and goals align with those of the company. This is an important incentive for our personal development as well as for the company's success. As a result from our performances during the thesis and the content shared among the staff members, we have both been offered positions in the company. We are happy to announce that as of January 2013 we will officially be working for Creo Dynamics AB.

We would like to direct our sincerest gratitude to our supervisors during this thesis: Dr. Christophe Mattei and Dr. Peter Davidsson at Creo Dynamics AB. Christophe is an experienced engineer in the field of experimental acoustics and non-destructive testing. We often received new inputs from Christophe in our work. New approaches, geometries, parameters and techniques to be studied and so on. Christophe has a very ambitious and innovative personality and it has been a pleasure working alongside him. Peter has many years of experience in the aerospace industry with projects in structural dynamics and numerical methods. He often contributed with new ideas and gave us (together with Christophe) a quick introduction course in acoustics, a topic we did not encounter during our years at Chalmers. Peter's positive attitude and his sense of humour seemed to reflect on the co-workers and the atmosphere at the office seemed a bit more pleasant with his presence. Both Peter and Christophe have inspired us and provided us professional guidance throughout the thesis and for that we are very grateful. They have devoted much attention to our progress and served as mentors. With them we would also like to thank our future co-workers at Creo Dynamics AB and our CEO, Gustav Kristiansson, for showing faith in us. Many thanks!

Further, we would like to express our appreciation to our examiner: Professor Anders Boström at Chalmers University of Technology. His advice and guidance was listened upon closely and it was always a pleasure to visit him at his office. Along with him we would also like to thank the staff at Chalmers, and especially the Applied Mechanics Department, who have taught us so much during the past five years. Thank you!

Joakim Truedsson at Altair Engineering Inc. deserves a special thanks for his support. During the initial stages of the thesis we experienced minor difficulties with the software platform: Hyperworks. Neither of us were familiar with this software during our time at Chalmers and naturally we encountered many error messages. Joakim never seemed to tire of our queries and taught us many new tricks in his field of expertise. He is a major reason for our success in this thesis. Thank you Joakim!

Last, but not least, we would like to thank our respective families. They have supported us from the very beginning and we would not be here today if it were not for their love and encouragement.

List of Abbreviations and Symbols

2D 2-dimensional
3D 3-dimensional
CFRP Carbon Fibre Reinforced Polymer
CLT Classical Lamination Theory
DOF Degree of Freedom
FE Finite Element
FEM Finite Element Method
FFT Fast Fourier Transform
fd product Frequency-thickness product
GUW Guided Ultrasonic Waves
iFFT inverse Fast Fourier Transform
IP In Plane
NDT Non Destructive Testing
OOP Out Of Plane
PZT Piezoelectric ceramic
SDT Spectral Decomposition Technique
SHM Structural Health Monitoring
STFT Short-time Fourier Transform
TRI Time Reversal Imaging
TRM Time Reversal Mirror
ZCT Zero Crossing Technique

ω	$\rightarrow$	angular frequency	$[rad/s]$
c_T	$\rightarrow$	shear wave velocity	$[m/s]$
c_L	$\rightarrow$	longitudinal wave velocity	$[m/s]$
k	$\rightarrow$	wave number	
d	$\rightarrow$	plate thickness	$[m]$
c_g	$\rightarrow$	group velocity	$[m/s]$
c_p	$\rightarrow$	phase velocity	$[m/s]$
E	$\rightarrow$	elasticity modulus	$[Pa]$
ν	$\rightarrow$	Poisson′s ratio	
ρ	$\rightarrow$	density modulus	$[kg/m^3]$

Contents

1 Introduction

Fibre reinforced materials have received an increased amount of attention in recent years. Their superior characteristics, in terms of specific strength, have made them highly desirable in the aerospace industry where there is an increasing demand of light-weight structures [1]. However, their complex mechanical behaviour, as opposed to metallic materials, leaves question marks and new challenges that need to be addressed.

Composites are composed of different phases of material (fibre and matrix), rendering the structure a heterogeneous set-up with anisotropic material properties. These attributes make them prone to sustaining *internal damages*. Internal damages within composite structures can be featured as (1) *fibre breakage*, (2) *matrix cracking*, (3) *debonding* (separation of fibres from the matrix) or (4) *delaminations* (failure of bonding between adjacent composite plies), to name a few. These defect types can cause severe degradation of the mechanical properties and lead to critical failure if not discovered in time.

One type of internal defect that deserves special attention is delamination. A delamination is present when the adhesive of two adjoining plies fail. This usually occurs during impacts on the structure and is caused by high interlaminar stress levels. A drawback that follows with delaminations lies within the inability to detect the damage with schedule-based visual inspections. Traditional ultrasonic inspection techniques (such as C-scans) have proven effective in detecting internal damages, but the interval time between the inspections can at times be insufficient and these methods are costly and time ineffective. Further, the parts chosen for inspection need to be reassembled and assessed individually.

Manufacturers in the aerospace industry aim to replace traditional materials with light-weight composites in coming years. To ensure that damages do not go undetected it is very important to get a real-time update of the structural integrity. Is there a damage in the structure? Can it be located? What type of damage is it and will it cause critical failure? These questions, among others, can be answered by implementing *Structural Health Monitoring* (SHM).

There are many ways of defining SHM in the literature. [2] describes SHM as: "... a continuous, autonomous in-service monitoring of the physical condition of a structure by means of embedded or attached sensors with a minimum manual intervention, to monitor the structural integrity of the aircraft". Another way of defining SHM is [3]: "... a system with the ability to detect and interpret adverse "changes" in a structure in order to improve reliability and reduce life-cycle costs".

The concept of SHM is not restricted to a specific industrial sector, but can be applied for buildings, bridges, oil-drilling facilities, windmills and other structures. The possibilities with this concept seem immense. Nevertheless, many SHM systems rely on evaluation models for damage localization techniques and extensive numerical analysis during the design process. Numerical modelling plays therefore a key part of SHM in the process of damage analysis. Numerical models will allow for a better understanding of the physical phenomena that occurs when ultrasonic waves interact with damages and how to use the acquired information to successfully assess the structural integrity.

1.1 Structural Health Monitoring

To get a more lucid understanding of the concept of SHM it might be advantageous to first describe *Non Destructive Testing* (NDT), as these two areas are closely related. NDT techniques have been developed continuously throughout the years with the objective to detect anomalies in structures caused by impacts, fatigue, corrosion or other unforeseen conditions. The main NDT techniques are [1]: visual inspection; optical methods; eddy-current (electro-magnetic testing); ultrasonic techniques (including laser ultrasonics, phased-array, Lamb wave techniques, etc..); acoustic emission; vibration analysis; radiography and thermography. Some of these techniques will be reviewed in following chapters, with focus on Lamb waves.

The need from aircraft manufacturers to reduce maintenance costs has been pushing researchers in an attempt to integrate NDT technology in the aircraft structure itself [4]. By doing so, i.e. replacing conventional NDT with SHM systems, some major benefits that can be expected are [5]:

- Replacing schedule-based inspection/maintenance of a structure by condition-based maintenance.
- Significantly reducing life-cycle cost.
- Improving safety of new as well as aging aircraft, aerospace and civil structures.
- Elimination of component tear down.
- Reduced inspection downtime.
- Potential prevention of failure during operation.

A way to illustrate a SHM system is to compare it to the human nervous system. [4] explains: "The idea of SHM is to build a system that is similar to the human nervous system. It will work in the same manner but will differ in some cases: If you brake your leg, it may be that you do not notice it or there is only a slight pain. This is because the bones have no nerves, i.e. no "SHM System". In the case of aircraft, the sensors (that are the nerves) must be at the place where an area is to be monitored to ensure the structural integrity. In case of damage, the sensors directly identify the location and follow-up actions can be taken."

1.2 Project background

LOCOMACHS - Low-cost manufacturing and assembly of composite and hybrid structures, is an EU fincanced research project that aims to significantly reduce or eliminate the most time-consuming non-adding value operations in airframe assembly systems [6]. Such expensive operations include structural health inspections in order to maintain operational safety of the aircraft, and is today representing approximately one-third of the total costs for acquiring and operating composite structures [1]. Creo Dynamics AB has among a large number of aircraft industry companies, universities and research institutes been assigned to participate in and conduct LOCOMACHS within a period stretching from September 2012 to March 2016. Due to the magnitude of the project, roughly EUR 32.8 million in total budget [6], participating partners have distributed their efforts and resources within different areas of research. Consequently, Creo Dynamics AB has been commissioned for a number of objectives from which this thesis is defined.

On the behalf of Creo Dynamics AB, a thesis work has been formulated with focus on the development of model-based resonance inspection techniques for 3D composite aerospace components. The objective of the thesis is to establish a solid basis, develop and evaluate the potential in different damage detection techniques for a generic 3D aerospace structure based on numerical models. To construe the dynamical effects of an induced damage is the primary objective of the thesis, rather than designing a complete SHM system.

The area of research is restricted to the aerospace *stringer* component. A stringer is a supportive section of the aircraft skin whose fundamental function is to prevent buckling during compressive and shear loads, as well as to counteract against bending and axial loads. It can be found throughout the whole aircraft and varies in both shape and size. Figure 1.2.1 gives a clear and representative view of stringer components in the Boeing 787 Dreamliner.

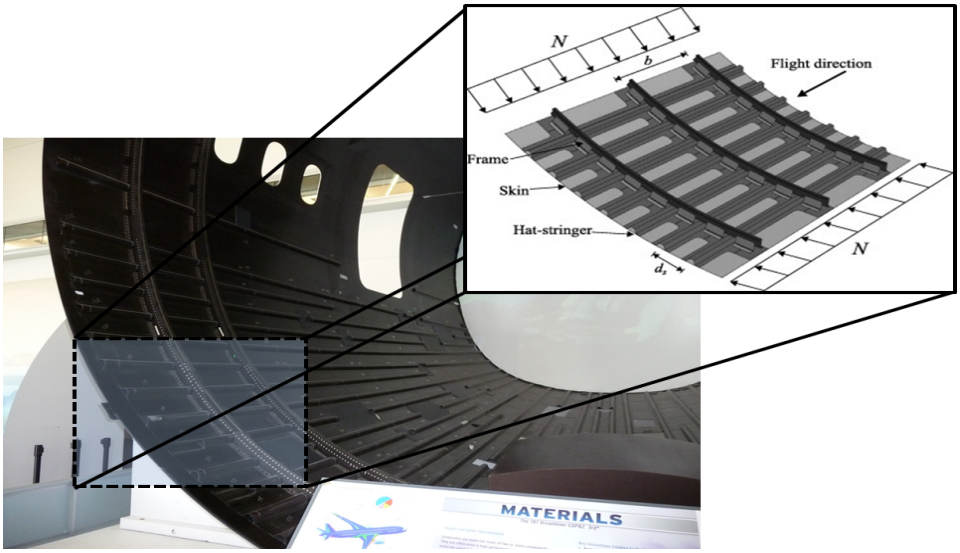

Figure 1.2.1: *Boeing 787 Dreamliner fuselage section. Used with authorization from Geoff Arnold (left) [7] and Kai-Uwe Schröder (right) [8].*

Harsh operating environments often expose the stringers to high stress levels that might inflict damages of varying types. In addition, as a result of their complex geometries, the presence of manufacturing-induced flaws are always an immediate risk [9]. These stringer attributes are aggravated when built out of a composite material. NDT is as previously mentioned a complicated process for composite materials much due to their propensity of sustaining internal damages. Adding complex geometries and high inaccessibility of the stringer to the equation, the difficulties in efficient health inspections and operational safety maintenance become apparent.

The duration of LOCOMACHS is after the finalization of this thesis another three years. Therefore, the work is conducted on the premise that the results should act primarily as a basis for further research within LOCOMACHS rather than as the establishment of an ideal SHM system.

1.3 Project definition and objective

Creo Dynamics AB is involved in the development of vibration and wave propagation based techniques for SHM of aerospace composite structures. The optimization and assessment of the sensitivity in SHM systems rely on the accessibility to relevant components with representative defect types which can be costly and impractical. An attractive alternative is to use numerical models to describe the dynamic response of a composite structure including defect modelling in order to assess the sensitivity of vibration and wave propagation based damage detection in a virtual environment.

The objective of this project is to describe the dynamic response of an aerospace stringer component in the frequency range 50 Hz – 1 MHz. The work relies on the development of a suitable FE model for the simulation of propagation of elastic vibrations in this frequency range. The model should describe the structure at a relevant level of detail for the study of transient wave propagation including the interaction with characteristic features and potential defects such as delaminations. The project will not address the simulation of real transducers or sensors in a more detailed way than necessary for reliable simulations and results.

The objectives of the project are:

1. To gather comprehensive knowledge of structural characteristics and emerged effects due to defects in a pre-defined frequency range of 50 Hz – 1 MHz, and to use this knowledge in the construction of a reliable FE stringer model.
2. To use the established model for studies of sensitivity in pre-defined excitation and detection configurations through processing of time signals.

3. To use the model to investigate the potential of one or several damage detection techniques from a SHM perspective.

1.4 Project approach

The geometrical dimensions of the stringer are to say the least complex. Variations of thickness, different curvature radii and material property variations are some among a number of stringer characteristics that makes it difficult to analyse. The structural behaviour, at both low and high frequencies, is thus hard to predict. How will an induced longitudinal or shear wave propagate in the stringer? Will other sound wave modes be present? How will the stringer behave when excited by relatively low frequencies, i.e. what features will the mode shapes and *frequency response functions* (FRF) inherit? In particular, how will a damage influence the abovementioned characteristics of the stringer and what conclusions can be drawn from these observations in terms of damage size, damage location and damage type?

In order to improve the prospects of making an accurate interpretation of the observed dynamic response of the stringer, a case study is formulated. This study enables observations of the structural behaviour in a more comprehensive manner, and conclusions can thus be drawn which later will be applied to the complex stringer geometry. The case study is performed on a quadratic plate with geometrical dimensions and material properties that are thoroughly defined. The case study also enables comparison of results to the literature which helps in the verification process of examined modelling issues. Overall, the objective of the study is to evaluate structural characteristics from which conclusions can be drawn and thereby enable the stringer to be modelled in a prosperous way. Answers to the following issues are sought, among others.

- What low frequency characteristics does the plate inherit and are these affected by the presence of damage? These questions can be narrowed down to the following:

    1. Are plate eigenfrequencies and mode shapes influenced by a defect and if so, can conclusions be drawn regarding the relation between damage size and emerged frequency shifts/mode shape differences?
    2. Does the through-thickness and IP location of a damage influence the eigenfrequencies and the mode shapes?
    3. What conclusions can be drawn by comparing the FRFs of a damaged and an undamaged plate regarding damage size, location and severity?

- What high frequency characteristics, i.e. sound wave propagation, are observed in the plate? Also this question is narrowed down to the following:

    1. How does the velocity of the propagating wave vary depending on frequency content and geometrical dimensions?
    2. What features are observed in a sound wave – damage interaction? Does the through-thickness location of a defect influence this interaction?
    3. What is the relation between spatial and time resolution to frequency content of the propagating wave and what type of time integration scheme, i.e. explicit or implicit transient analysis, is appropriate to obtain a stable result?

- What modelling detail level is necessary for reliable results? Can a homogenization procedure be implemented to save computational time without compromising the accuracy of the results?

- How well does known and examined damage detection techniques and measuring/sensing configurations show the presence of induced damage?

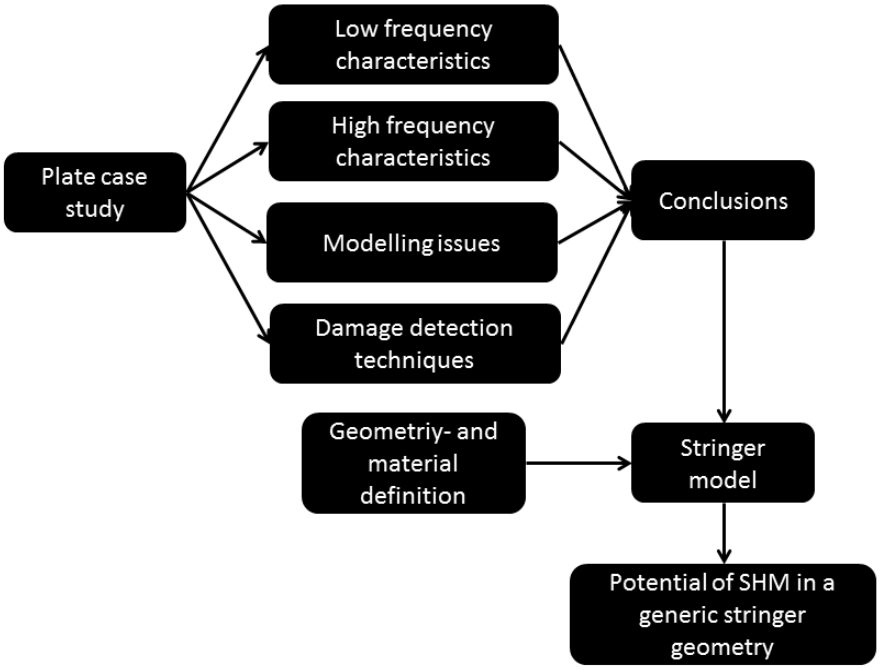

Figure 1.4.1: *Principle scheme for project approach.*

Observations and conclusions in the case study serve as a base for what choices to be made in the stringer analysis. By applying underlying theories and evaluating modelling issues on a plate geometry, essential knowledge of the structural behaviour is gained for low as well as for high frequency scenarios.

The Hyperworks platform developed by Altair Engineering Inc. is used in this thesis. Hypermesh in the pre-processing, Radioss as the solver and Hyperview in the post-processing. Matlab has also been used in the post-processing of the results.

1.5 Lamb wave theory

Guided Ultrasonic Waves (GUW) and their applicability in SHM systems have shown significant improvements in recent years. There exists a wide variety of wave types with the ability to propagate through solid media, yet some have displayed more desirable features in NDT and deserve therefore to be reviewed more closely.

A vital aspect to be considered in NDT is the geometry of the specimen in question. Depending on the geometry, different wave types can be induced in the structure. For instance, when waves propagate through an infinite solid medium the wave types present in the structure are longitudinal waves, shear waves, or a combination of both. However, due to the presence of boundaries in finite structures such as plates and stringers, other wave types will emerge and become dominant. Since much research have been focused on locating defects in thin plate-like structures, such as laminates, the wave types that will be discussed in detail are *Lamb waves*.

Lamb waves are waves that occur in a free plate with traction-free boundaries on the upper and lower surface of the plate [10]. Lamb waves have the advantage of propagating through long distances in plates with low attenuation and are sensitive to small defects which makes them ideal in NDT applications.

1.5.1 Governing equations

When a plate is subject to a high frequency excitation several Lamb wave modes can propagate simultaneously with different velocities and particle motion characteristics. This is known as the *multimodal* phenomenon in wave propagation. What mode types that are present depend heavily on the product of the frequency content of the wave and the plate thickness, i.e. the *fd* product. A high *fd* product will trigger higher modes (including modes that emerge at lower frequencies), whereas a low *fd* product will trigger lower modes only. Ultimately,

all modes can be categorized into two infinite sets with respect to the oscillatory pattern of the upper and lower plate boundaries:

1. *Symmetrical* (extensional) modes
2. *Asymmetrical* (flexural) modes

The features of these mode types will be discussed in detail in the following sections. It is however important to mention that these mode types propagate with different velocities in plates. The governing equations that describe the relationship between wave motion velocity and frequency in isotropic plates, called the characteristic equation are:

$$\frac{\tan(qd/2)}{\tan(pd/2)} = -\frac{4k^2pq}{(q^2-k^2)^2} \quad \text{for symmetrical modes} \tag{1.5.1}$$

$$\frac{\tan(qd/2)}{\tan(pd/2)} = -\frac{\left(q^2-k^2\right)^2}{4k^2pq} \quad \text{for asymmetrical modes} \tag{1.5.2}$$

with p and q given by

$$p^2 = \frac{\omega^2}{c_L^2} - k^2 \tag{1.5.3}$$

$$q^2 = \frac{\omega^2}{c_T^2} - k^2 \tag{1.5.4}$$

(The symbols and their units are described in detail in List of Abbreviations and Symbols). The governing equations can be used to determine the velocity at which a wave with a particular *fd* product will propagate [10]. The equations can be solved numerically in an iterative process, resulting in the phase velocities from which the group velocities can be derived (see section 1.5.4 for group and phase velocity definition). *The Lamb Toolbox* [11] in Matlab is used to evaluate the velocities based on the governing equations throughout this thesis. These velocities are referred to as the theoretical velocities.

1.5.2 Symmetrical modes

Symmetrical Lamb waves move in a symmetrical fashion about the mid-plane of the plate [12]. The particle motion in these modes are dominated by IP displacements, whereas OOP displacements are equal to zero in the mid-plane and increase towards the boundaries. These modes usually propagate faster than asymmetrical modes and experience less attenuation. Symmetrical modes can be induced by applying a force parallel to the plate.

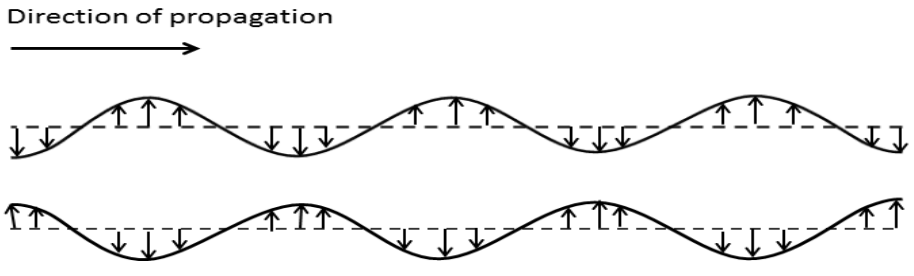

Figure 1.5.1: *Boundary particle motion of symmetrical Lamb waves.*

1.5.3 Asymmetrical modes

The particle motion of the asymmetrical Lamb wave modes is dominated by the OOP displacements. The IP displacements are equal to zero in the mid-plane and increase towards the boundaries. Asymmetrical modes experience higher attenuation in contrast to symmetrical modes and the propagation velocities tend to be lower. Asymmetrical modes can be induced by applying a force normal to the plate.

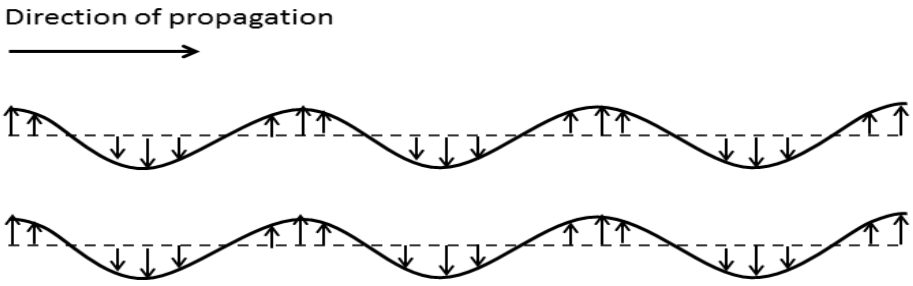

Figure 1.5.2: *Boundary particle motion of asymmetrical Lamb waves.*

1.5.4 Dispersion characteristics

As mentioned previously symmetrical and asymmetrical modes propagate with different velocities depending on the *fd* product. This attribute is what makes the Lamb waves *dispersive*. There are two different types of velocities with which a wave can propagate:

- *Group Velocity* c_g
- *Phase Velocity* c_p

The group velocity is the speed of the overall wave packet, whereas the phase velocity is the speed of the individual waves in the wave package. When the phase and group velocities coincide ($c_p = c_g$) no dispersion is experienced. The plate geometry, however, will prevent this scenario and the velocities will differ. Generally, the phase velocity tends to exceed the group velocity ($c_p > c_g$) and is denoted *classical* dispersion [10]. The waves appear to originate behind the wave packet, travel to the front, and disappear. In plates however, the opposite relation can be witnessed, i.e. $c_p < c_g$. This is called *anomalous* dispersion where the wave appear to originate at the front of the wave packet, travel to the rear, and disappear.

The velocities are often characterized in so called *dispersion curves* with the velocity on the vertical axis and the *fd* product on the horizontal axis (see Figure 1.5.3).

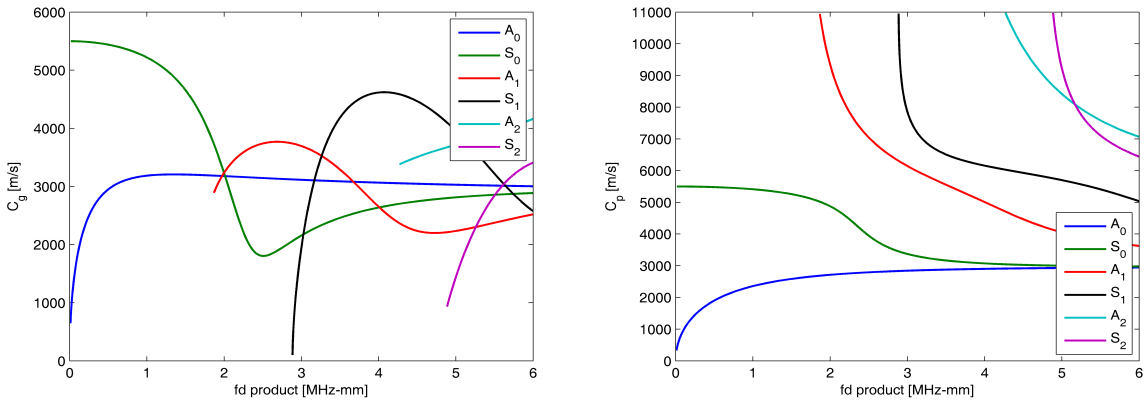

Figure 1.5.3: *Group velocities (left) and phase velocities (right) for an aluminium plate. Values obtained by [11].*

Many Lamb wave techniques in NDT for locating damages rely on phase and group velocities and it is therefore essential that the dispersion curves are known beforehand. Further, to avoid clutter in the signal response from multiple wave modes, simulations are usually performed by excitation of the first two Lamb wave modes, also known as the *fundamental modes*. These modes occur for all frequencies, as can be seen in Figure 1.5.3, and are denoted A_0 and S_0 [3]. It might therefore prove beneficial not to exceed to the cut-off *fd* product for the A_1 mode, so as not to trigger higher modes, if such a technique is implemented. The *fd* product for when a specific mode starts to propagate is denoted the cut-off *fd* product.

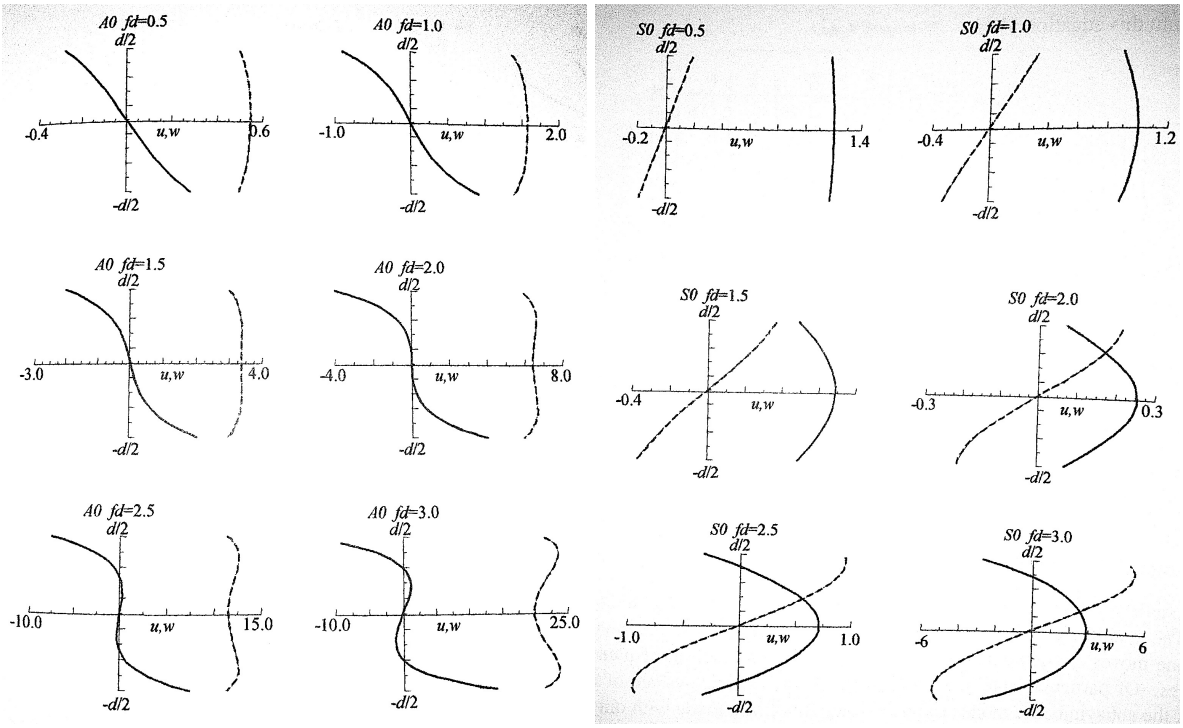

Figure 1.5.4: *IP and OOP displacements for A_0 mode (left) and S_0 mode (right) respectively for an aluminium plate. Solid lines represent IP displacements whereas dashed lines represent OOP displacements. Used with authorization from Professor Joseph L. Rose [10].*

The IP- and OOP displacements of the fundamental modes are presented in Figure 1.5.4. As depicted, increasing the *fd* product for the A_0 mode will not have a significant effect on the relationship between the displacements. The OOP displacement still remains dominant in higher *fd* regions. The S_0 mode, however, will behave differently. As the *fd* product increases the IP displacement will adopt a 180° arc feature and locally near the boundaries the OOP displacement will become dominant. This will have implications in performed numerical simulations in the following and will be explained more in section 2.4.2.

1.5.5 Lamb waves in composite materials

Lamb waves in composite plates have different dispersion characteristics than in isotropic materials as a result from the inherent material anisotropy, multi-layered construction and heterogenity of constituents [13]. The waves exhibit in general lower velocities than in isotropic plates and will differ depending on the laminate lay-up and direction of wave propagation. A unidirectional laminate will experience higher velocities in the fibre orientation compared to the transverse direction. This effect can be mitigated by choosing a quasi-isotropic laminate that "mimics" the extensional stiffness behaviour of an isotropic plate by equally distributing the fibre orientations, e.g. in the 0°,90°,45° and -45° -direction.

The group and phase velocities for composites are difficult to acquire through theoretically derived equations and The Lamb Toolbox can thus not be used for this purpose. To obtain dispersion curves for composite plates, FE models are used with different measurement techniques that will be discussed in section 2.3.

2 Plate case study

The plate case study serves as a base for what choices to be made in the stringer analysis. This chapter thoroughly explains regarded issues and necessary steps taken for establishing this base.

As a start, three composite plate models with varying complexity, in terms of model size and element type, are presented in section 2.1. The analogy of these models are at a later stage reviewed in order to determine the necessary level of detail for the stringer model. Further, excitation modelling is discussed covering input signal attributes, excitation methods and space and time discretization, section 2.2. Before the evaluation of the plate models, numerical techniques for wave velocity estimation are discussed in section 2.3. By comparing numerically obtained dispersion curves between the different FE - models, it is possible to outline what effects the meshing have on a propagating wave, see section 2.4.2. This comparison underlies the meshing of the stringer, thus reliable measuring techniques are of great importance. The techniques are at first applied to an aluminium plate to verify that the measurement techniques give accurate results in section 2.4.1.

The evaluation of the plate models is followed by section 2.5 treating different types of defects and how these are modelled in an appropriate way. Last but definitely not least, damage detection and localization techniques are studied. This section expands upon the low frequency behaviour of the plate models and observed structural changes caused by a damage. The interaction between a propagating wave and a defect is analysed. In addition, the concept of time reversal imaging for damage detection/localization is looked into.

2.1 Composite plate models

Three different composite plates are modelled in the case study - one 2D shell element model and two 3D solid element models of varying complexity. The models are established for two main reasons. Firstly, to observe the structural behaviour between models and secondly, to draw conclusions from these observations in order to determine what level of detail the stringer model ought to possess.

The modelled composite plate is a 200×200 mm, 16-layered quasi-isotropic CFRP with a $[0/90/-45/45]_{2s}$ stack-up. The plate in question is 2.08 mm thick, resulting in a ply thickness of 0.13 mm. A Rayleigh damping model is applied to the composite plates, defined as in equation 2.1.1, where ξ_i denotes the fraction of critical damping for mode i.

$$2\xi_i = \frac{\alpha}{\omega_i} + \beta\omega_i \tag{2.1.1}$$

α and β are specified by defining the frequency range of interest. Assuming ω_i to be 100 kHz and 300 kHz (transformed to rad/s) and a critical damping factor of 0.02 (2%) yields $\alpha = 9424.8$ rad/s and $\beta = 8 \cdot 10^{-9}$ 1/(rad/s). This model assumes that the damping matrix simply is a linear combination of the mass and stiffness matrices according to equation 2.1.2.

$$\mathbf{C} = \alpha\mathbf{M} + \beta\mathbf{K} \tag{2.1.2}$$

Typical values of the modal damping factor ξ are $0.01 \leq \xi \leq 0.1$ [14].

The space and time resolution is at a later stage altered with respect to the frequency content of the excitation signal and is not discussed in this section. Nevertheless, an IP element size of 0.5×0.5 mm is assumed in this section to enable just comparisons in terms of model sizes.

2.1.1 2D shell element model

The 2D shell element model is built in Hypermesh by CQUAD4 elements, i.e. 4-noded elements comprising three translational and three rotational *degrees of freedom* (DOFs) per node. This yields, for the given geometry and element size, a total of 160 000 elements or 964 830 DOFs.

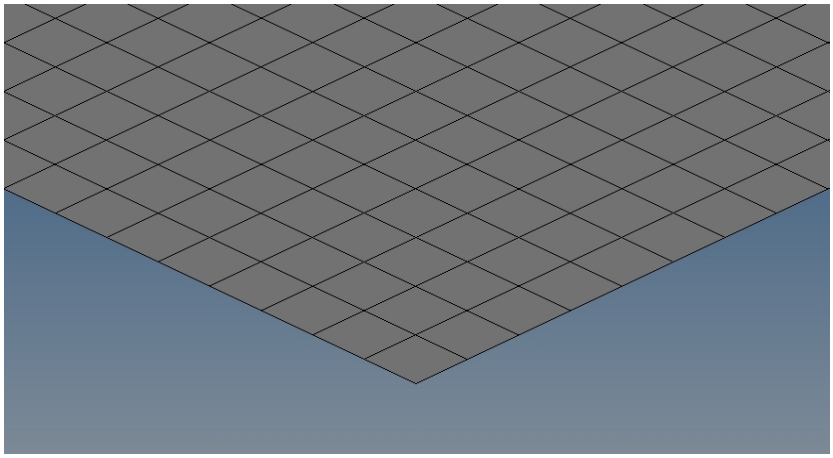

Figure 2.1.1: *2D shell element model of the composite plate.*

For the homogenization of the plate, *classical lamination theory* (CLT) is applied both in Matlab and in the Hypermesh module: *Hyperlaminate*. Briefly, CLT relates the strain at any point of the deformed plate to the displacements (u_0, v_0 and w_0) and curvatures (k_x, k_y and k_{xy}) of its geometric mid-plane according to equation (2.1.3).

$$\begin{Bmatrix} \epsilon_x \\ \epsilon_y \\ \gamma_{xy} \end{Bmatrix} = \begin{Bmatrix} \epsilon_x^0 \\ \epsilon_y^0 \\ \gamma_{xy}^0 \end{Bmatrix} + z \begin{Bmatrix} k_x \\ k_y \\ k_{xy} \end{Bmatrix} \tag{2.1.3}$$

where

$$\begin{Bmatrix} \epsilon_x^0 \\ \epsilon_y^0 \\ \gamma_{xy}^0 \end{Bmatrix} = \begin{Bmatrix} \frac{\partial u_0}{\partial x} \\ \frac{\partial v_0}{\partial y} \\ \frac{\partial u_0}{\partial y} + \frac{\partial v_0}{\partial x} \end{Bmatrix} \text{ and } \begin{Bmatrix} k_x \\ k_y \\ k_{xy} \end{Bmatrix} = - \begin{Bmatrix} \frac{\partial^2 w_0}{\partial x^2} \\ \frac{\partial^2 w_0}{\partial y^2} \\ 2\frac{\partial^2 w_0}{\partial x \partial y} \end{Bmatrix} \tag{2.1.4}$$

Note that the normal strains ϵ_z^0 are neglected in the CLT and that z represents the distance from the mid-plane to the point of interest. The intralaminar stresses are assumed to vary linearly and are calculated according to equation (2.1.5). $\left[\bar{Q}\right]_k$ denotes the lamina stiffness matrix which is unique in each ply. Subscript k refers to the ply number and should not be confused with the curvature of the plate.

$$\begin{Bmatrix} \sigma_x \\ \sigma_y \\ \tau_{xy} \end{Bmatrix}_k = \left[\bar{Q}\right]_k \left\{\varepsilon^0 + zk\right\} \tag{2.1.5}$$

A resultant force is now obtained by integrating the corresponding stresses over the thickness of the plate, equation (2.1.6)

$$\begin{Bmatrix} N_x \\ N_y \\ N_{xy} \end{Bmatrix} = \int_{-h/2}^{h/2} \begin{Bmatrix} \sigma_x \\ \sigma_y \\ \tau_{xy} \end{Bmatrix} dz = \sum_{k=1}^{n} \int_{h_{k-1}}^{h_k} \begin{Bmatrix} \sigma_x \\ \sigma_y \\ \tau_{xy} \end{Bmatrix}_k dz \tag{2.1.6}$$

The equivalent calculation is performed for the resultant moment M, with the exception that the variable z is included in the first integral of equation (2.1.6) in order to consider the torque. Combining equations (2.1.4) and (2.1.5) with equation (2.1.6), the total constitutive equation for the composite plate can be expressed by equation (2.1.7).

$$\begin{Bmatrix} N \\ M \end{Bmatrix} = \begin{bmatrix} A & B \\ B & D \end{bmatrix} \begin{Bmatrix} \epsilon^0 \\ k \end{Bmatrix} \tag{2.1.7}$$

where

$$A_{ij} = \sum_{k=1}^{n} (\bar{Q}_{ij})_k (h_k - h_{k-1}),\ B_{ij} = \frac{1}{2} \sum_{k=1}^{n} (\bar{Q}_{ij})_k (h_k^2 - h_{k-1}^2),\ D_{ij} = \frac{1}{3} \sum_{k=1}^{n} (\bar{Q}_{ij})_k (h_k^3 - h_{k-1}^3) \tag{2.1.8}$$

Matrix A is the *extensional stiffness matrix* which relates the resultant force to the mid-plane strain. The *coupling matrix* B holds information of the coupling between bending and extension of the plate while the *bending stiffness matrix* D relates resultant moments to plate curvatures [15].

Worth mentioning is that CLT holds information in the through-thickness location of each ply. This is realized when examining the derivation above and means that the outer plies have a more contributing effect on the bending stiffness matrix in contrast to the mid-plane plies.

To verify the accuracy of the homogenization in Hyperlaminate, CLT is implemented in Matlab and the outputs are compared in terms of the A, B and D matrices. The correlation between the Hyperlaminate and Matlab results is very accurate. The extensional and bending stiffness matrix are except for numerical round off errors identical for the two approaches. Since the composite plate is symmetric it is not exposed to any bending-stretching coupling and the coupling stiffness matrix therefore only contains zero entities. As a result from this verification the final 2D shell element model is homogenized in Hyperlaminate.

2.1.2 3D solid element models

Two 3D solid element plate models are built and compared. 8-noded hexahedron elements are used in both models, i.e. 8-noded elements with three translational DOFs per node.

The 3D non-homogenized solid element model possess a high level of complexity, and is the most detailed plate model created. Each composite layer is represented with a corresponding element layer, in which fibre directions and local material properties are taken into consideration.

In an effort to decrease model complexity a homogenization procedure is implemented. This procedure strictly calculates a mean stiffness matrix and applies it to the entire structure. Thereby, a fewer number of elements through the thickness of the plate can be used. Detailed description of the 3D homogenized and non-homogenized plate models are given below.

3D non-homogenized solid element model

The non-homogenized composite plate model comprise sixteen elements through the thickness of the plate, equivalent to one element layer per composite ply. Each layer is given a local coordinate system rotated an angle θ with respect to the global OOP-axis, where θ corresponds to the fibre direction of each respective ply.

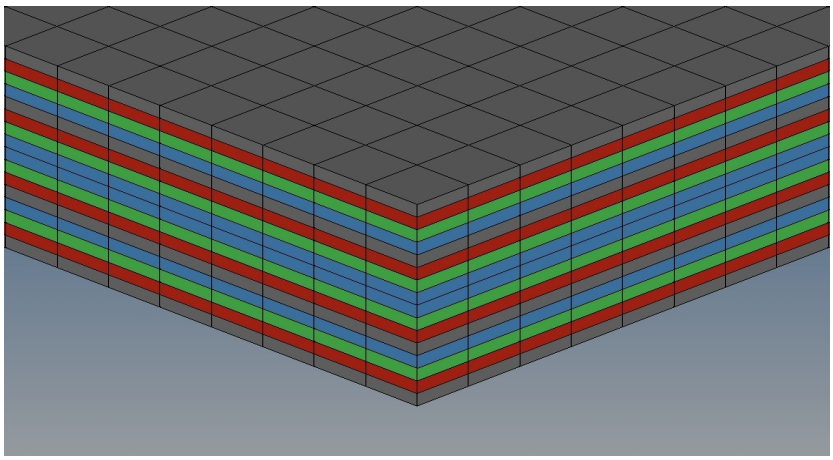

Figure 2.1.2: *Non-homogenized solid element model. One element layer per composite ply. Layers with same colour have identical fibre directions.*

The elastic properties of the given unidirectional composite with respect to the longitudinal, IP transverse and OOP transverse directions are defined. Note that these properties are equal for all plies. Finally, each ply property is referenced to its equivalent local coordinate system, resulting in a model where each ply, i.e. each element layer, have different elastic properties with respect to the global coordinate system (plies with identical fibre directions obviously yield identical elastic properties in the global system).

As a result of this high level of complexity, the number of elements are 2 560 000 or in total 8 200 863 DOFs.

3D homogenized solid element model

When modelling the composite plate using 3D solid elements, the extensive computational work that may be lie ahead in the solving process must be considered. This is especially the case when each ply is modelled by one layer of 3D hexahedron elements, resulting in no less than sixteen elements through the thickness of the plate. Thus a very large model is obtained even for such a small geometry like the plate in question. Adding the influence of the time integration, the computational calculations rapidly become very heavy. A way to avoid such large models is by homogenizing the composite plate. The material elastic properties, i.e. the composite stiffness matrix, for each ply will then no longer have to be accounted for, but instead as constant values in the homogenized parts. This enables the possibility to decrease the number of elements through the plate thickness and thereby decrease the number of DOFs, i.e. decrease the model size. In the homogenized model the entire plate is homogenized and represented by four element layers, see Figure 2.1.3.

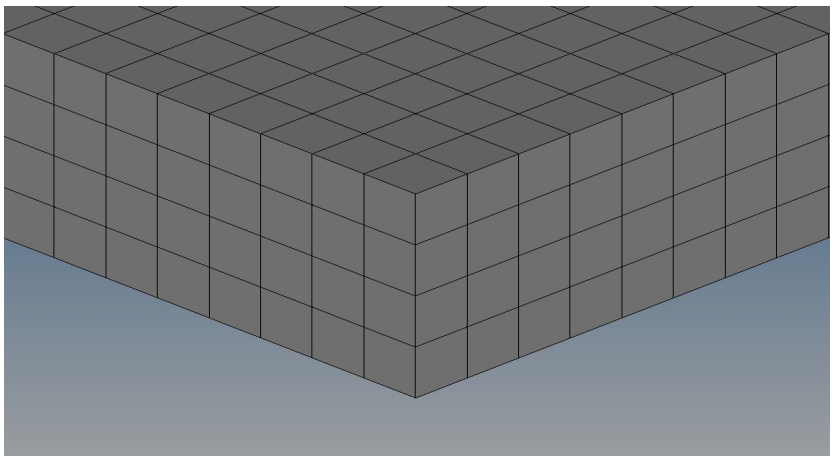

Figure 2.1.3: *3D solid element model built by 8-noded hexahedron elements.*

For a $200 \times 200\,\text{mm}$ plate with an IP element size of $0.5 \times 0.5\,\text{mm}$, the 3D homogenized plate comprises 640 000 elements and 2 412 027 DOFs.

The homogenization algorithm assumes that each ply of the composite material is orthotropic, meaning that the material exhibits symmetry in its elastic properties in three orthogonal planes [15]. The stress-strain relation for such a material is given by equation (2.1.9).

$$\begin{Bmatrix} \sigma_1 \\ \sigma_2 \\ \sigma_3 \\ \tau_{23} \\ \tau_{13} \\ \tau_{12} \end{Bmatrix} = \begin{bmatrix} Q_{11} & Q_{12} & Q_{13} & 0 & 0 & 0 \\ Q_{12} & Q_{22} & Q_{23} & 0 & 0 & 0 \\ Q_{13} & Q_{23} & Q_{33} & 0 & 0 & 0 \\ 0 & 0 & 0 & Q_{44} & 0 & 0 \\ 0 & 0 & 0 & 0 & Q_{55} & 0 \\ 0 & 0 & 0 & 0 & 0 & Q_{66} \end{bmatrix} \begin{Bmatrix} \epsilon_1 \\ \epsilon_2 \\ \epsilon_3 \\ \gamma_{23} \\ \gamma_{13} \\ \gamma_{12} \end{Bmatrix}, \; \boldsymbol{\sigma} = [Q]\,\boldsymbol{\epsilon} \tag{2.1.9}$$

Since the strains as a function of stresses are somewhat easier to derive than the opposite, the stiffness matrix $[Q]$ is calculated by first establishing the compliance matrix $[S]$ and inverting it to establish $[Q]$ according to equation (2.1.10),[16].

$$\boldsymbol{\epsilon} = [S]\,\boldsymbol{\sigma} \Longrightarrow \boldsymbol{\sigma} = [S]^{-1}\,\boldsymbol{\epsilon} = [Q]\,\boldsymbol{\epsilon} \tag{2.1.10}$$

where

$$[S] = \begin{bmatrix} \frac{1}{E_1} & \frac{-\nu_{12}}{E_1} & \frac{-\nu_{13}}{E_1} & 0 & 0 & 0 \\ \frac{-\nu_{12}}{E_1} & \frac{1}{E_2} & \frac{-\nu_{23}}{E_2} & 0 & 0 & 0 \\ \frac{-\nu_{13}}{E_1} & \frac{-\nu_{23}}{E_2} & \frac{1}{E_3} & 0 & 0 & 0 \\ 0 & 0 & 0 & \frac{1}{G_{23}} & 0 & 0 \\ 0 & 0 & 0 & 0 & \frac{1}{G_{13}} & 0 \\ 0 & 0 & 0 & 0 & 0 & \frac{1}{G_{12}} \end{bmatrix}, \quad \frac{\nu_{ij}}{E_i} = \frac{\nu_{ji}}{E_j} \ (i,\ j = 1,\ 2,\ 3) \tag{2.1.11}$$

Having knowledge of the elastic properties in the longitudinal (subscript 1), IP transverse (subscript 2) and OOP transverse (subscript 3) directions, the stiffness matrix for one ply is established. However, in order to perform the homogenization, the stiffness matrices for the plies have to be formulated with respect to the same global coordinate system. Stresses and strains therefore need to be transformed between local and global coordinate systems according to equation (2.1.12), which in the end results in a stiffness matrix $[C^*]$ expressed in terms of the global system.

$$\begin{Bmatrix} \epsilon_1 \\ \epsilon_2 \\ \vdots \\ \gamma_{12} \end{Bmatrix} = [T_\epsilon] \begin{Bmatrix} \epsilon_x \\ \epsilon_y \\ \vdots \\ \gamma_{xy} \end{Bmatrix}, \quad \begin{Bmatrix} \sigma_1 \\ \sigma_2 \\ \vdots \\ \tau_{12} \end{Bmatrix} = [T_\sigma] \begin{Bmatrix} \sigma_x \\ \sigma_y \\ \vdots \\ \tau_{xy} \end{Bmatrix} \tag{2.1.12}$$

$[T_\sigma]$ and $[T_\epsilon]$ are the stress and strain transformation matrices (see APPENDIX A) from the global to the local coordinate system and θ represents the angle between the global x-direction and the fibre direction of a specific ply.

By inserting equation (2.1.12) into equation (2.1.9), equation (2.1.13) is obtained including the stiffness matrix $[D]$ for one ply with respect to the global coordinate system.

$$\begin{Bmatrix} \sigma_1 \\ \sigma_2 \\ \vdots \\ \tau_{12} \end{Bmatrix} = [Q] \begin{Bmatrix} \epsilon_1 \\ \epsilon_2 \\ \vdots \\ \gamma_{12} \end{Bmatrix} = [Q]\,[T_\epsilon] \begin{Bmatrix} \epsilon_x \\ \epsilon_y \\ \vdots \\ \gamma_{xy} \end{Bmatrix} = [T_\sigma] \begin{Bmatrix} \sigma_x \\ \sigma_y \\ \vdots \\ \tau_{xy} \end{Bmatrix} \Longrightarrow$$

$$\begin{Bmatrix} \sigma_x \\ \sigma_y \\ \vdots \\ \tau_{xy} \end{Bmatrix} = [T_\sigma]^{-1}\,[Q]\,[T_\epsilon] \begin{Bmatrix} \epsilon_x \\ \epsilon_y \\ \vdots \\ \gamma_{xy} \end{Bmatrix} = [D] \begin{Bmatrix} \epsilon_x \\ \epsilon_y \\ \vdots \\ \gamma_{xy} \end{Bmatrix} \tag{2.1.13}$$

The actual homogenization is performed by integrating the stiffness matrix $[D]$ over the thickness of the plate, considering one ply at the time. Since all elastic properties are constant through the thickness of each ply, this integration turns out to be a simple summation of the ply stiffness matrices giving a mean stiffness matrix $\mathbf{D}$.

$$\mathbf{D} = \int_{-t/2}^{t/2} [D\,(z)]\,dz = \frac{1}{N} \sum_{k=1}^{N} [D]_k \tag{2.1.14}$$

The stiffness matrix $\mathbf{D}$ is now applied to the whole composite model. Unlike the 2D CLT, no consideration is taken to the through-thickness location of each ply. Naturally, this has an effect on the bending stiffness since information is lost regarding the fibre directions of the plies.

A summery of the created composite plate models are presented below.

Table 2.1.1: Comparison of plate models.

Model	Level of complexity	Pre - processing effort (modelling)	Computational effort (solving)	Number of DOFs
2D homogenized	Medium	Medium	Low	964 830
3D homogenized	Medium	Low	Medium	2 412 027
3D non-homogenized	Very high	High	Very high	8 200 863

To model the stringer in an appropriate way, a large number of FE issues are taken into account. The chosen strategy usually results in a compromise between computational effort (required pre-processing and solving time) and accuracy of the results. As mentioned, this chapter aims to resolve these issues and thus establish a solid basis for the stringer geometry analysis.

2.2 Excitation modelling

The excitation of the plate models can be conducted in a large variety of ways. To begin with, it has to be defined what the excitation ought to result in in terms of structural behaviour. For example, the excitation method required for a modal analysis differs significantly from the several methods available considering Lamb wave generation. This section is mainly focusing on the generation of GUW, in particular Lamb waves, rather than the comparatively simple excitation methods applied for low frequency spectra.

Prior to the discussion of different excitation methods, a brief review is given of the most frequently used signals in this project. Last but not least, the space and time discretization approaches are discussed which have large influence on the results.

2.2.1 Excitation signals

The characteristics of the transmitted signal is of great interest for several reasons. The wavelength, and indirectly the frequency content, is highly correlated to the ability to detect a structural defect. Waves with short wavelengths are more likely to detect defects than waves with larger wavelengths. This relation is discussed in section 2.6.3. The wavelength λ is calculated according to equation (2.2.1), where f is the frequency [Hz] and c_0 the wave speed [m/s] of the given wave mode obtained from the dispersion curves, see section 1.5.4.

$$\lambda = \frac{c_0}{f} \tag{2.2.1}$$

The bandwidth of the signal is related to the wavelength and is also very important. Should a broadband or a narrowband signal be emitted into the medium? The choice of bandwidth has a crucial effect on the wave propagation characteristics in plate-like structures. For a signal with narrow bandwidth, the energy is concentrated at the central frequency [17], keeping the signal relatively non-dispersive. This is generally speaking an advantage in SHM due to its minimization of dispersion [18]. A broadband signal, however, containing a large number of frequencies, tends to be stretched out in the time domain due to the dispersive characteristics of the plate. As discussed in section 1.5.4, high frequency signals in dispersive media have a different propagation velocity than low frequency signals. This means that for an excitation signal containing both low and high frequencies, different wavelets will propagate with different velocities, and the wave packet will thus be stretched out in the time domain. This may be problematic when interpreting an acquired signal. On the other hand, a broader bandwidth covers a larger part of the frequency spectrum which can be preferable due to the relation between defect size and wavelength discussed above.

In this project, two types of signals are mainly used — one narrow bandwidth signal and one broadband signal. The narrow band signal, from now on referred to as tone burst, is defined as a sine wave function acting over 5.5 periods and modulated by a Hanning time window. Its central frequency is easily altered and the frequency content is obtained by applying the *fast Fourier transform* (FFT). The number of periods also has an influence on the frequency content. A higher number yields a more narrow bandwidth but results at the same time in a signal with a longer duration in the time domain. Once again, this can be problematic and a 5.5 tone burst is thus considered to be a good compromise. Figure 2.2.1 below shows the 5.5 tone burst used throughout this project including its frequency content. The central frequency of this specific signal is 200 kHz.

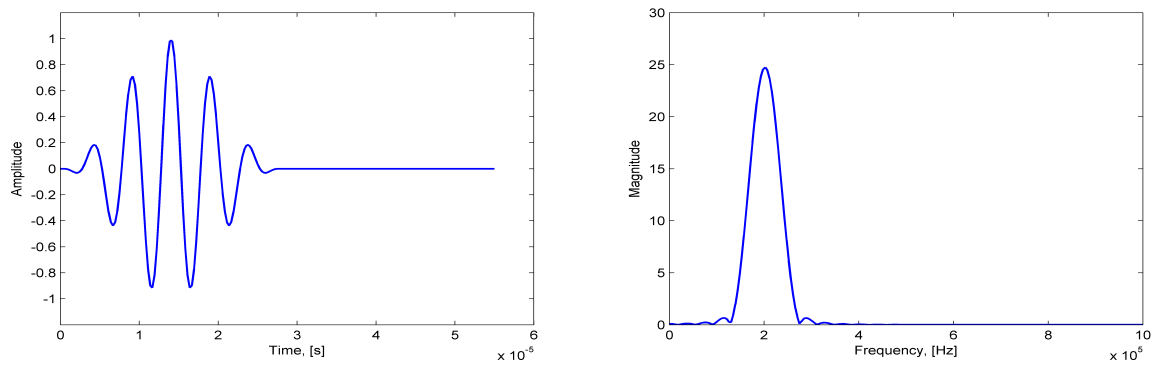

Figure 2.2.1: *200 kHz 5.5 tone burst in time and frequency domain.*

The broadband signal, from now on referred to simply as the pulse, is constructed more or less in the same way as the tone burst, but with the exception that it only has a duration of 1 period. The central frequency is similarly to the tone burst 200 kHz and as can be seen in Figure 2.2.2 the frequency spectrum is clearly broadened.

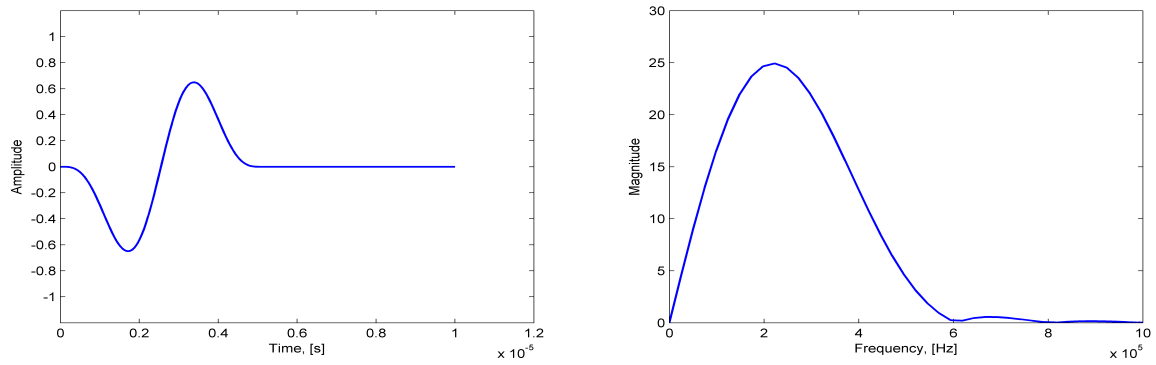

Figure 2.2.2: *200 kHz pulse in time and frequency domain.*

It should be mentioned that the central frequency, both for the tone burst and the pulse, is varied throughout the project, and that the 200 kHz central frequency here only is given as an example.

2.2.2 Transmission and reception

The selection of transducer type must be performed in a proper way and suited for the application. Frequency content and bandwidth ought to be considered parallel to optimization procedures of inspection capabilities [12]. As stated in section 1.3, the project will not address the simulation of real transducers or sensors in a more detailed way than necessary for reliable simulations and results. Focus is instead to model the transducer in such a way that it excites realistic and representative sound waves. However the fundamental characteristics of the chosen transducer type need to be taken into consideration such as force input and deformation pattern.

Today, piezoelectric ceramic (PZT) discs are the most widely used acoustic transducers due to their wide frequency responses, excellent mechanical strength, low power consumption and low cost [12],[19]. PZT discs operate on the piezoelectrical principle of direct transformation of electric energy into elastic energy and vice versa by coupling the electrical variables (electrical field and electrical displacement) to the mechanical variables (mechanical strain, mechanical stress) in the discs. The discs are strongly coupled with the structure by an adhesive bond and excite/sense the Lamb waves in the structure directly through IP strain coupling [20].

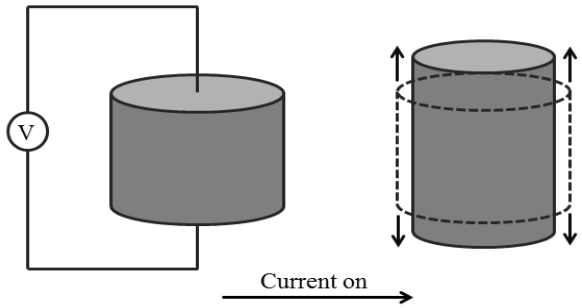

Figure 2.2.3: *Principle of PZT discs [12].*

The PZT discs are modelled as circular geometries by 2D shell elements attached to the surface of the structure. Perfect bonding between disc and structure is assumed and the force/displacement input is applied in the radial direction. The input type (force or displacement) and magnitude is varied throughout the project and presented in each separate section. Note that mechanical forces/displacements are modelled, not the electric-elastic energy transformation. Circular discs are modelled in order to achieve homogeneous wave propagation in all directions.

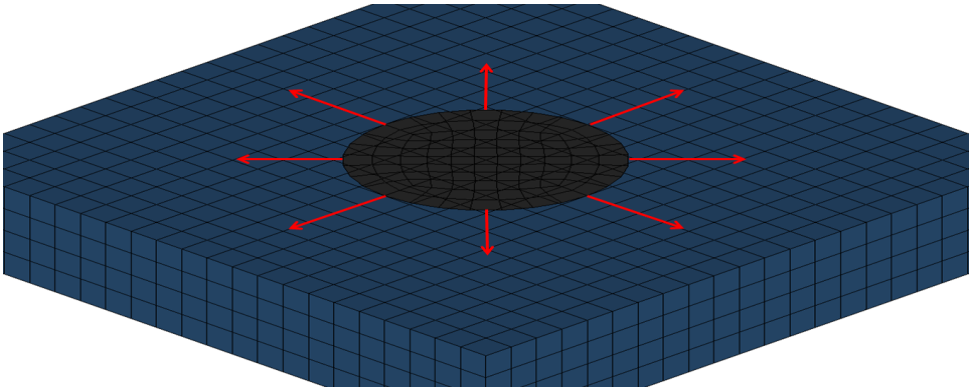

Figure 2.2.4: *Modelled PZT disc (dark gray) attached to structure (dark blue), red arrows indicate force/displacement input direction.*

The structures, in particular the plates, are also in some cases excited by predefined displacements of nodes in the through-thickness direction. Two excitation patterns are here applied, both as predefined OOP displacements. This excitation procedure has no physical counterpart and is conducted during the establishment of dispersion curves, see sections 1.5.4 and 2.3.

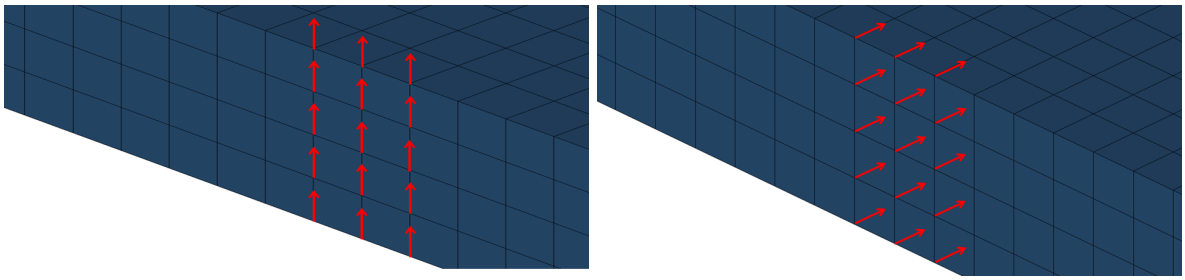

Figure 2.2.5: *Asymmetric- and symmetric mode excitation patterns during the establishment of dispersion curves.*

The idea behind these two excitation patterns is to imitate, and thus trigger, the particle motion of the A_0 and S_0 Lamb wave modes to enable accurate and representative measurements.

The red arrows in Figure 2.2.4 and Figure 2.2.5 represent the unit vectors of the excitation. These vectors are related to the desired excitation signal, see section 2.2.1, meaning that the excitation will be in the

opposite direction for negative amplitudes of the time signal.

2.2.3 Space and time discretization

In order to resolve all frequencies present in a propagating wave, the mesh size needs to be considered with caution. Usually 8-10 elements per wavelength is sufficient while larger elements will give rise to reflections of the input signal at the mesh boundaries [18]. This needs to be avoided since it falsely indicates the presence of a structural defect. Combining equation (2.2.1) with the 8-10 elements per wavelength relation, the mesh size of the model is defined as:

$$l^e \leq \frac{\lambda}{8} = \frac{c_0/f}{8} \tag{2.2.2}$$

Equation (2.2.2) proves that knowledge of the frequency content in the transmitted signal is of great importance. Consequently, the mesh size needs to be adjusted to the highest frequency of the propagating wave.

A transient response analysis is used to calculate the response of a structural system that is exposed to time-dependent loads such as those presented in section 2.2.1. For the transient analysis used in this project, the Newmark-β method is applied, i.e. an implicit and unconditionally stable time integration scheme.

The discrete equation of motion for the Newmark-β method is enforced at the time step t_{n+1} and requires that [14]:

$$\mathbf{M}\ddot{\mathbf{u}}_{n+1} + \mathbf{C}\dot{\mathbf{u}}_{n+1} + \mathbf{K}\mathbf{u}_{n+1} = \mathbf{p}_{n+1} \equiv \mathbf{p}\left(t_{n+1}\right) \tag{2.2.3}$$

where

$$\dot{\mathbf{u}}_{n+1} = \mathbf{u}_n + \left[(1-\gamma)\,\ddot{\mathbf{u}}_n + \gamma\ddot{\mathbf{u}}_{n+1}\right] h \tag{2.2.4}$$

and

$$\mathbf{u}_{n+1} = \mathbf{u}_n + \dot{\mathbf{u}}_n h + \left[(1-2\gamma)\,\ddot{\mathbf{u}}_n + 2\beta\ddot{\mathbf{u}}_{n+1}\right] \frac{h^2}{2} \tag{2.2.5}$$

The constant h is the time step size given as input in Radioss. γ and β are parameters that weights the contributions from the current and the previous time step. Newmark proposed that for an unconditionally stable solution, $\gamma = \frac{1}{2}$ and $\beta = \frac{1}{4}$ [14]. Inserting equations (2.2.4) and (2.2.5) into equation (2.2.3) yields:

$$\left[\mathbf{M} + \gamma\mathbf{C} + \beta h^2\mathbf{K}\right] \ddot{\mathbf{u}}_{n+1} = RHS_n \tag{2.2.6}$$

where

$$RHS_n = -\mathbf{K}\mathbf{u}_n - \left(\mathbf{C} + h\mathbf{K}\right)\dot{\mathbf{u}}_n - \left[h(1-\gamma)\mathbf{C} + \frac{h^2}{2}\left(1-2\beta\right)\mathbf{K}\right]\ddot{\mathbf{u}}_n \tag{2.2.7}$$

By inserting equation (2.2.7) into equation(2.2.6) and solving the equation for the second derivative in time step $n+1$, based on displacements, velocities and accelerations from time step n, displacements and velocities in time step $n+1$ can be evaluated by implementing equations (2.2.4) and (2.2.5). This is a step-wise process that loops through all time steps. The number of time steps is given as input to Radioss. An unconditionally stable scheme yields stable results for any value of the time step size h. However, in order to avoid aliasing, the time step size (thus indirectly the sampling frequency) needs to be at least two times the Nyquist frequency, i.e. two times the highest frequency of the signal. This criterion is easily fulfilled in all simulations since the excitation signals are defined with very small time steps. For example, the 200 kHz tone burst presented in Figure 2.2.1 is defined by 100 time steps, resulting in a time step size of $2.75 \cdot 10^{-7}$ s and thus a sampling frequency of approximately 3.6 MHz, i.e. high above the Nyquist criteria.

2.3 Numerical techniques for velocity estimation

The dispersive characteristics of the composite plate models need to be known prior to damage detection analysis. Several aspects that influence the selection of damage detection techniques are connected to the dispersion curves of the composite. However, to obtain dispersion curves analytically for laminates can prove to be a difficult challenge. Consequently, different measurement techniques for velocity estimation are instead employed on time-domain signals generated with FE models and verified against the Lamb Toolbox results in Matlab.

The Lamb Toolbox does, however, only evaluate dispersion characteristics for isotropic materials, which results in a verification procedure involving the creation of an isotropic aluminium FE-model with the identical material properties as the given input to the Lamb Toolbox. This section describes the numerical techniques for group and phase velocity estimation, whereas the credibility of the techniques and verification procedure is presented in section 2.4.1.

2.3.1 Spectral Decomposition Technique for group velocity estimation

The *Spectral Decomposition Technique* (SDT) calculates the group velocity of the Lamb waves in a number of signal processing steps. Initially, the signal response at two separate locations (with given distance in between) is measured and the frequency contents are obtained by applying the FFT. Secondly, the frequency spectra of the two aquired signals are filtered by a Gaussian filter in order to obtain velocities corresponding to the right frequencies. The filtered signals are then transformed back to the time domain using the *inverse Fast Fourier transform* (iFFT) and the envelope of the signals are calculated with the Hilbert transform. Finally, the time delay between the two reconstructed signals is estimated by cross correlation and the group velocity is thus obtained. The algorithm presented in [21] is given below.

1. Two acquired signals at different locations are selected;
   $u_x(t)$ and $u_{x+\Delta x}(t)$.
2. The frequency spectra of these two signals are calculated using the FFT;
   $U_x(f) = FT[u_x(t)]$ and $U_{x+\Delta x}(f) = FT[u_{x+\Delta x}(t)]$.
3. The frequency spectra are filtered using a Gaussian filter;
   $U_{x,F}(f) = U_x(f) \cdot H(f)$ and $U_{x+\Delta x,F}(f) = U_{x+\Delta x}(f) \cdot H(f)$,
   where $H(f) = e^{-K(f-fn)^2}$, K is the coefficient which defines the bandwidth of the filter and f_n is the central frequency of the filter.
4. The filtered signals are reconstructed using the iFFT;
   $u_{x,F}(t) = FT^{-1}[U_{x,F}(f)]$ and $u_{x+\Delta x,F}(t) = FT^{-1}[U_{x+\Delta x,F}(f)]$.
5. The envelopes of the signals are calculated using the Hilbert transform;
   $u_{x,FH}(t) =\mid Hilbert[u_{x,F}(t)]$ and $u_{x+\Delta x,FH}(t) =\mid Hilbert[u_{x+\Delta x,F}(t)]$.
6. The time delay between two envelopes is estimated using a cross-correlation;
   $t_{\Delta x} = \underset{t}{argmax}\{corr[u_{x,FH}(t), u_{x+\Delta x,FH}(t)]\}$.
7. The group velocity is estimated;
   $c_g = \Delta x / t_{\Delta x}$.

The algorithm may be applied with different central frequencies and bandwidths. However, since the signals in the simulations already posses narrow bandwidth due to a tone burst excitation, see section 2.2.1, only one central frequency per simulation is applied. This implies that even though several group velocities can be measured from one simulation, only the velocity corresponding to the central frequency of the transmitted tone burst is calculated. The bandwidth of the Gaussian filter may also be varied. [22] recommends a bandwidth for A_0 of 75 kHz and for S_0 170 kHz. In this investigation, for the given plate thickness, a bandwidth of 90 kHz for A_0 and 140 kHz for S_0 turned out to give good results.

Since the central frequency for each simulation in this case is set to the central frequency of the excitation pulse, steps 2, 3 and 4 may be neglected in the algorithm, and the Hilbert transform can instead directly be

applied to the measured responses. This gives more or less the same results as performing all seven steps in the algorithm. The reason for exciting the plate models with a tone burst and not a pulse is to, hopefully, minimize the numerical errors that arise from the FFT. Consequently, a higher number of simulations is required.

2.3.2 Spectral Decomposition Technique – with STFT for group velocity estimation

An alternative method for estimating the Lamb wave group velocity can be achieved by tuning the excitation signal in such a manner that it covers a wide spectrum of frequencies. Unlike in the previous section for group velocity estimation, a chirp signal (see Figure 2.3.1) is set in motion instead of a tone burst. The chirp signal can be adjusted to cover a set of frequencies of choice, e.g. 80 – 800 kHz.

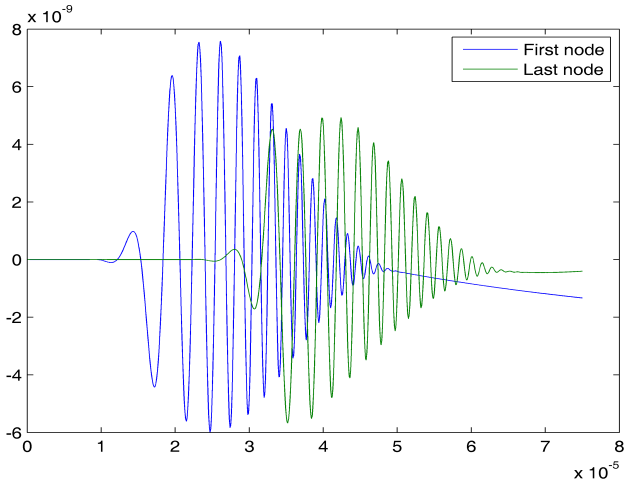

Figure 2.3.1: *Chirp signals.*

The group velocity is estimated for a specific frequency in the pulse, however this can not be accomplished in the frequency domain by FFT due to the broadband nature of the pulse. An additional parameter must be added in terms of the time domain [23], introducing time-dependency in the Fourier transform. Instead of performing the FFT over the entire time-span, the signal is pre-windowed into narrow time frames, Δt, and the FFT is computed for each time frame respectively. This procedure is known as *short-time Fourier transform* (SFTF). The length of the time frames determines the resolution of the STFT. A high resolution requires many time frames and Δt decreases in time, whereas for a low resolution it is sufficient with a small amount of time frames and thus the length of Δt will increase. The three-dimensional representation of a signal is denoted a *spectrogram*, with the signal energy density (dB) as the dependent variable and the time (s) and frequency (Hz) as the independent variables (see Figure 2.3.2).

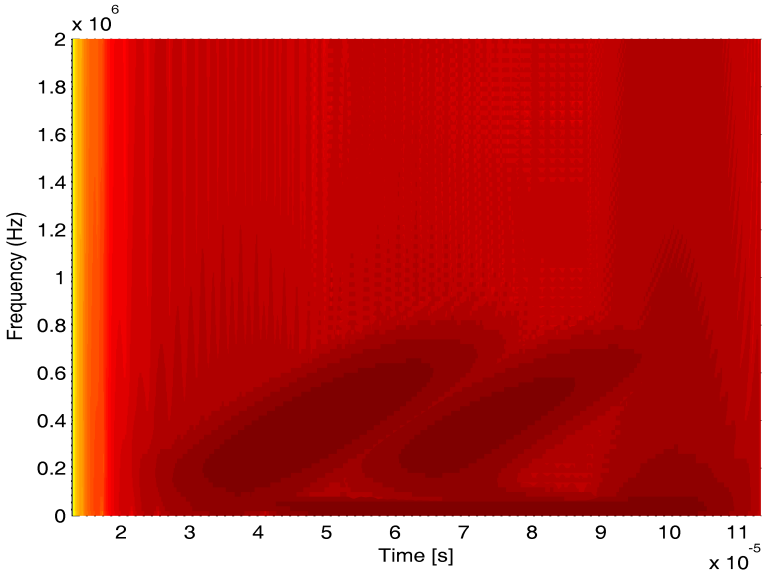

Figure 2.3.2: *Spectrogram.*

With a spectrogram at hand, a certain frequency will inherit two peaks in the time domain corresponding to two different measurement locations. The difference in time between these two peaks is the same time for which it takes that frequency content to propagate between the measurement locations. With the time difference and distance as known variables, it remains a simple matter to estimate the velocity.

This method for evaluating the group velocity is beneficial from a "computational effort"-point of view. Since the excitation signal contains a wide spectrum of frequencies the acquired data can prove to be sufficient with only one or two simulations of the FE model. The group velocities for all frequencies can then be estimated with the implementation of STFT. There is however a drawback with this technique. The time-frequency resolution is fixed, i.e. the time frames and the frequency frames are constant, which will affect the resolution of the spectrogram. Low frequencies will be subject to poorly estimated velocities for small Δt and good quality in velocities for large Δt, whereas the opposite relation will apply for high frequencies.

To use this method and receive accurate velocities the time resolution has to be taken into consideration. It might prove necessary to narrow down the frequency spectrum of the chirp signal in order to decrease the deviation in velocity that results in high and low frequencies for a fixed Δt. Further, it might be proper to use an intermediate value of Δt that will yield adequate results for both high and low frequencies.

2.3.3 Zero-Crossing Technique for phase velocity estimation

The technique presented in [22] for the phase velocity estimation requires extensive post – processing in Matlab since the response at a high number of nodes needs to be acquired. The reason for this is explained further down in this section.

The *Zero-Crossing Technique* uses the response at each node in a spatial interval along the plate. This enables the creation of a B-scan image within the chosen time- and space interval, as illustrated in Figure 2.3.3.

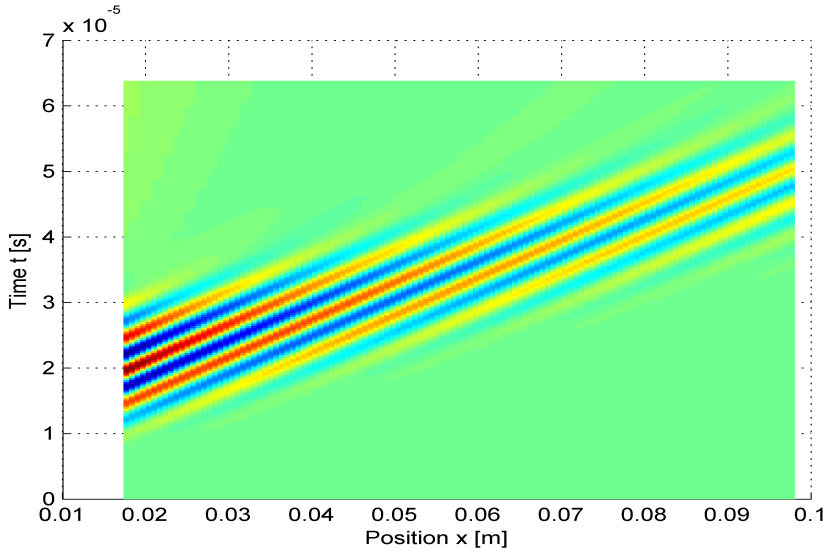

Figure 2.3.3: *B-scan, 200 kHz asymmetrical mode.*

By defining a threshold value U_{thr} the approximate position of the wave in the time domain is determined. This threshold value is arbitrary, but a value is set such as U_{thr} "cuts" the signal the same number of times as the desired number of so called zero-crossing points. Due to attenuation, this threshold value needs to be fitted to the signal at each separate position in space. To clarify, this is visualized in Figure 2.3.4 where the threshold value is set to 60 % of the maximum response at a certain position. The zero crossing points are easily found since it is known where the threshold value "cuts" the signal. Note that this procedure is performed for each position in the spatial domain. Information is thus obtained at what time instants the four zero-crossing points occurs for each position in the spatial domain.

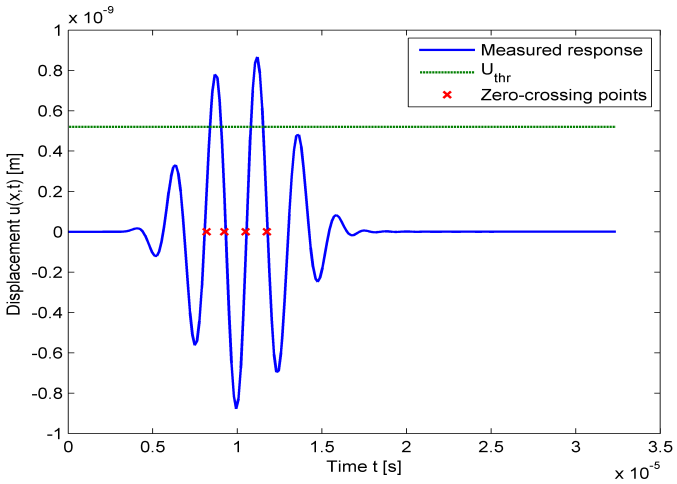

Figure 2.3.4: *Visualization of the displacement threshold value and the zero crossing points for a symmetric 400 kHz excitation.*

The idea behind the zero-crossing technique is to observe at what time instants the zero-crossing points occur, and to do this at each spatial measuring point. Consider for example the first (left) zero crossing point in Figure 2.3.4. This point occurs approximately at time $t = 0.8 \cdot 10^{-5}$ s for that specific measurement point. However, as illustrated in Figure 2.3.3 anomalous dispersion is exhibited, i.e. the phase velocity is lower than the group velocity. This is clear when examining an arbitrary half-period of the signal at two different positions. It can easily be seen how the half periods/wavelets travels "backwards" relative the propagating wave packet. This behaviour is also observed in Figure 2.3.3 where the half periods of the wave travel from the front to the

back, and while doing so, decrease in amplitude. Due to this attenuation of the half periods, it is clear that at a certain spatial position, the first "cut" between the threshold value and the signal that defines the first zero-crossing point will shift to the next half period. The linear relation between the propagation time and spatial position will therefore suddenly make a "jump" at this shift. This process is repeated a couple of times, i.e. the new half period defining the first zero-crossing point will travel slower than the wave packet/group velocity and attenuate until it is below the threshold value U_{thr}, and will be substituted by the half period in front which now defines the first zero-crossing point. These "jumps" that occur are visualized in Figure 2.3.5 and the number of jumps depends on the number of points used in the measurements.

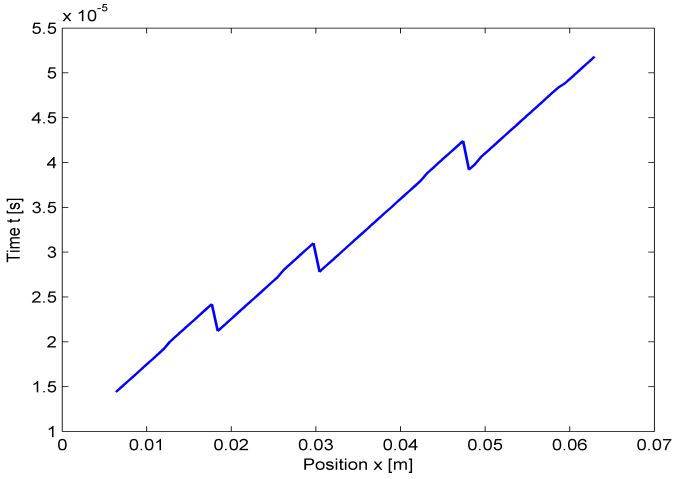

Figure 2.3.5: *Relation between spatial position and time of the third zero-crossing point.*

As described in [22], the distance between two jumps is important since it determines the spatial interval in which the phase velocity can be measured. Using two points within the same "jump interval" and their corresponding zero-crossing point time instants, the phase velocity is easily calculated. In [22] the most stable results are obtained using the third zero-crossing point for the phase velocity estimation. This is also the case for the models used in this investigation, even though the first and second zero-crossing points provide reliable results as well.

2.4 Evaluation of plate models

The composite plate models possess different levels of detail as discussed in section 2.1. What models to proceed from in the stringer geometry is a question of computational effort compared to accuracy of obtained velocities. A model with a very high level of detail may not be deemed necessary to use if the result is not distinguishable from that of a model which requires less computational effort. This fact enables for larger model geometries and a broader perspective of the structural behaviour of the stringer.

2.4.1 Validation of numerical techniques for velocity estimation

The techniques for group and phase velocity estimation in section 2.3 are verified before continuing the analysis in the stringer geometry. A problem that arises is the fact that the Lamb Toolbox is unable to calculate the dispersion curves for anisotropic materials. Thus an aluminium plate is chosen for measurement technique validation and the numerical velocity estimations are performed on an isotropic 3D solid element aluminium plate. The material properties for the aluminium plate are:

E [GPa]	ν	ρ [kg/m^3]
70.32	0.3354	2620.4

Spectral decomposition technique for group velocity estimation

This technique is used in the frequency interval 100 – 600 kHz. The excitation source is constructed by a 5.5 cycle sinusoid tone burst modulated by the Hanning window. In each simulation the central frequency is increased by 100 kHz. This results in a total of 12 simulations, 6 simulations for each mode. The symmetrical mode is triggered by an IP displacement whereas the asymmetrical mode is triggered by an OOP displacement.

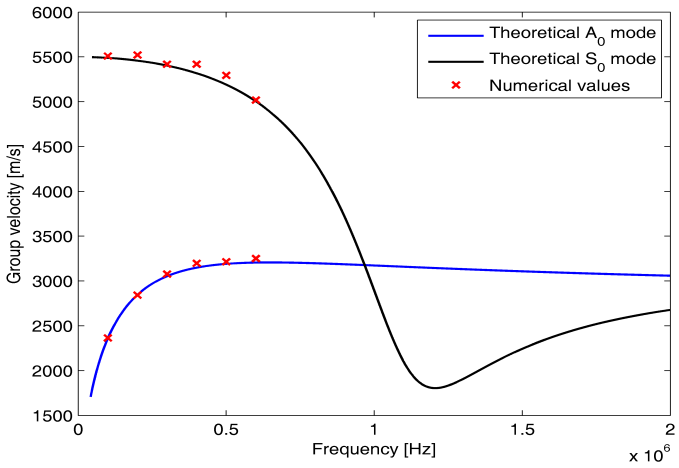

Figure 2.4.1: *Group velocity with Spectral decomposition technique.*

The response data is based on IP and OOP displacements for the symmetrical and the asymmetrical mode, respectively. The estimated results with SDT display good correlation to the theoretically obtained values as can be seen on Figure 2.4.1. The velocities deviate from the theoretical values with an estimate of 1.2% for the symmetrical mode and 0.8% for the asymmetrical mode.

Spectral decomposition technique – with STFT for group velocity

In this technique a chirp signal was used instead of a broadband sinusoid signal window much due to the difficulties encountered when interpreting the acquired data in a spectrogram. The frequencies vary from 80 – 800 kHz and only one simulation is required. The time resolution adopts three different values with a decreasing order (higher number results in lower resolution): 64, 256 and 512. The highest resolution, 64, yields good correlation for the velocities in the high frequency region of the signal. The lowest resolution, 512, shows the opposite effect with high accuracy for the low frequency velocities of the wave (see Figure 2.4.2).

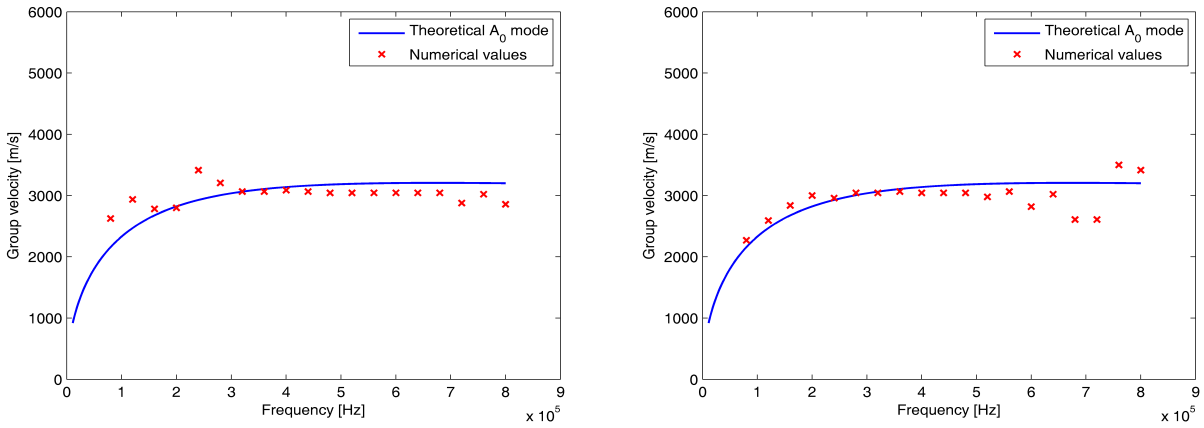

Figure 2.4.2: *Group velocities for a window length of 64 (left) and 512 (right).*

The high time resolution results in a 6.6% deviation whereas the low time resolution results in 6.8%. To optimize

the results an intermediate resolution of 256 is chosen that can capture the entire spectrum of frequencies (see Figure 2.4.3). The resulting deviation is now 4.8%.

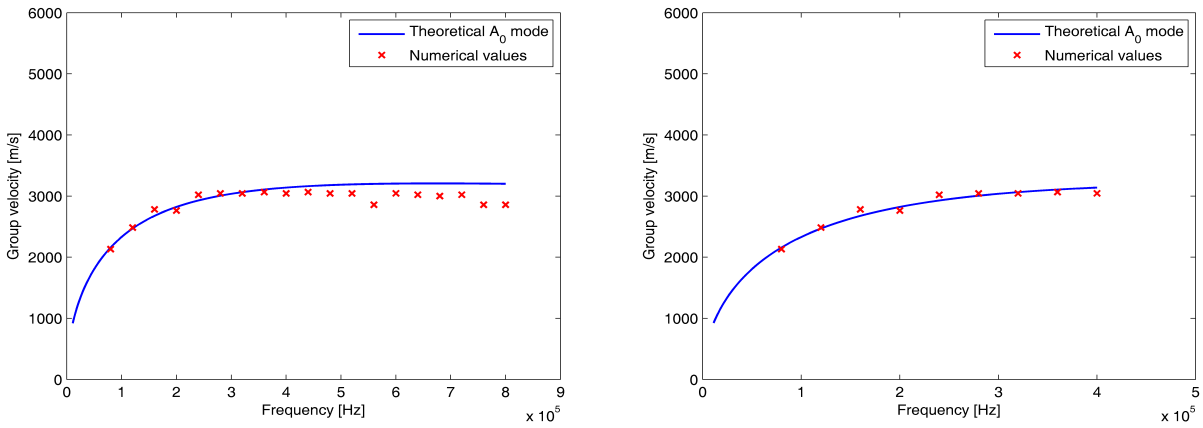

Figure 2.4.3: *Group velocities for a window length of 256.*

The results are yet to be improved by removing the values for the higher frequencies. A cut-off is made for frequencies above 400 kHz. This results in a deviation of 1.9% which can be compared to the results of the SDT for a tone burst signal.

Only the asymmetrical mode was taken into consideration for this technique since the chirp signal contains very high frequencies. The symmetrical mode is therefore not properly excited for higher frequencies and the method is not effective. The inaccurate results for the symmetrical mode in high frequency regions will be explained in section 2.4.2.

Zero crossing technique for phase velocity estimation

The set-up for this method is similar to that of SDT. However, ZCT requires several measurement points and different post-processing.

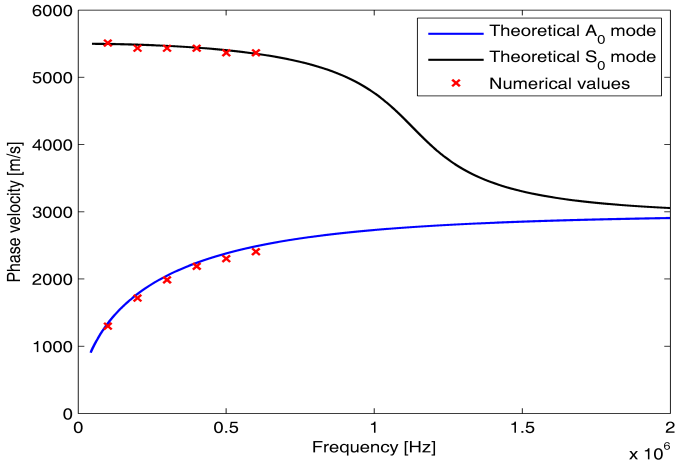

Figure 2.4.4: *Phase velocity using zero crossing technique (red crosses) and the Lamb Toolbox (blue and black lines).*

The results show good correlation to the theoretical values with only 0.5% deviation for the symmetrical mode and 3.1% for the asymmetrical mode.

2.4.2 Composite dispersion curves

The SDT and ZCT are the main tools for acquiring the dispersion characteristics of the composite plate. Dispersion curves are established for the 2D model, the 3D homogenized model and the 3D non-homogenized model respectively. The velocities for each *fd* product will be estimated for four different directions: 0°, 90°, 45° and −45°.

2D plate model

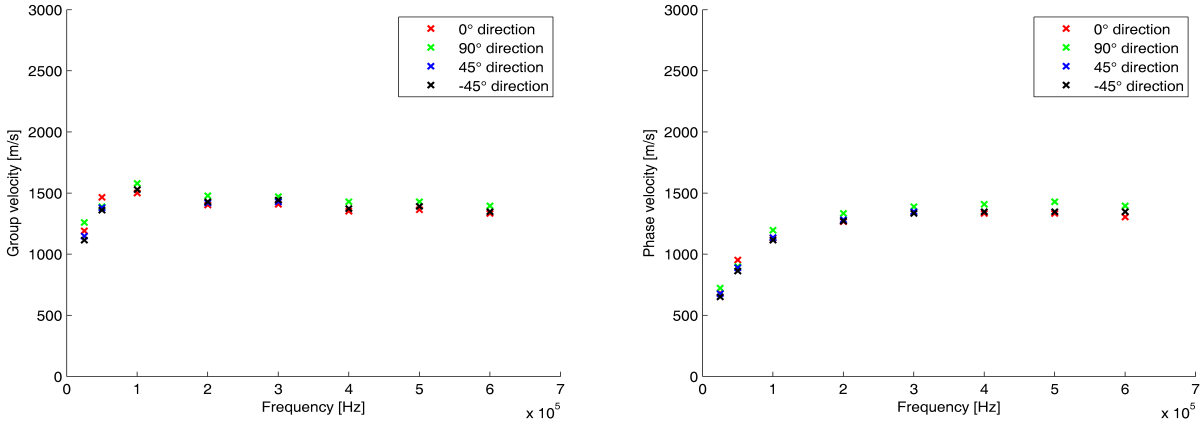

Figure 2.4.5: *Group velocity (left) and phase velocity (right) for A_0 mode.*

3D homogenized model

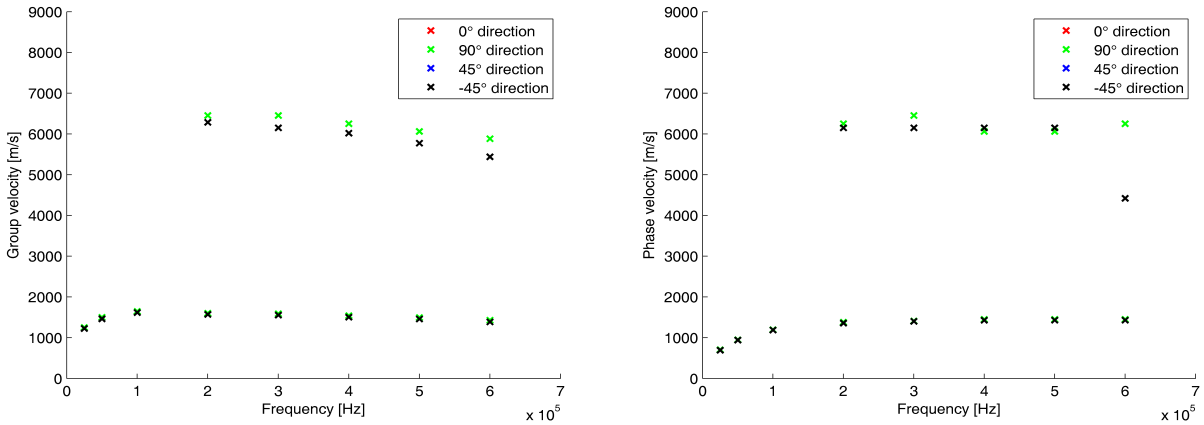

Figure 2.4.6: *Group velocity (left) and phase velocity (right) for the fundamental modes.*

3D non-homogenized model

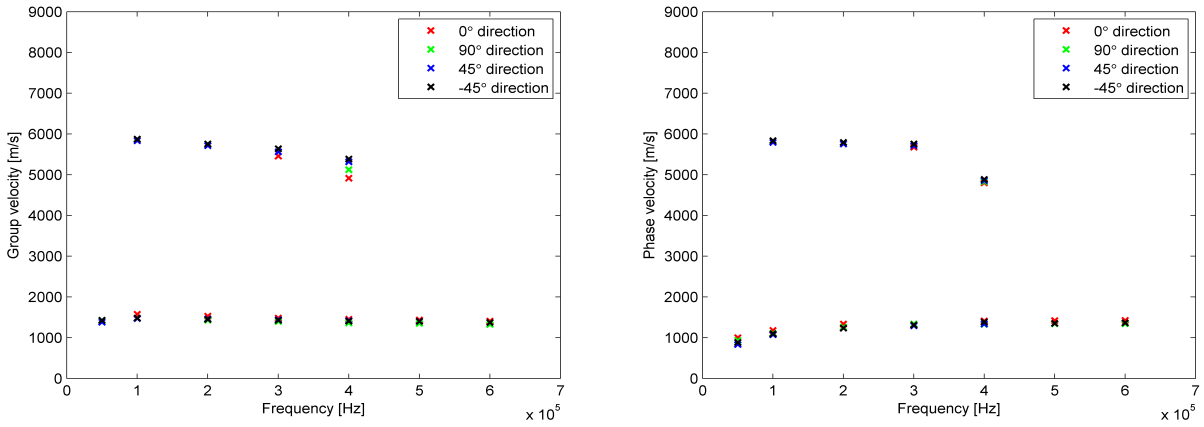

Figure 2.4.7: *Group velocity (left) and phase velocity (right) for S_0 mode.*

Conclusions

The difference in velocities between directions are very small and therefore negligible. The symmetric quasi-isotropic property of the laminate allocates the fibres in several directions and mitigates the effect that follows with anisotropy. For instance, the velocities would have been varying significantly for a $[+45_6/-45_6]_s$ laminate [13].

The comparison of results with the aluminium plate is notable. The S_0 mode possesses slightly higher velocities whereas the A_0 mode is nearly slower by a factor of 2. The difference between the models is very small, especially for the A_0 mode. The S_0 mode possesses different particle motion and for high frequencies (>400 kHz) the spread between the directions is getting higher, as illustrated in the figures. This error originates from the motion of excitation. The A_0 mode is excited by a OOP motion whereas the S_0 mode is triggered by an IP motion as discussed in section 2.2. The particle motion for higher *fd* products of the S_0 mode is, however, influenced by a large proportion of OOP motion in the vicinity of the boundaries (see Figure 1.5.4). This explains why the results deviate for higher *fd* products. To counter this problem the motion of excitation could be modified for higher *fd* product. However, the fact still remains that the particle motion for higher frequencies is an unknown variable and it is therefore not possible to accomplish by adjusting the excitation motion.

Further, it is shown that the 2D shell element model only estimates the A_0 mode (see Figure 2.4.5). The IP displacements that are set in motion to trigger the S_0 mode do not simulate the features of a symmetrical Lamb wave. Instead it appears to mimic the behaviour of a pure pressure wave. This can be connected to the fact that OOP strains can not be accounted for in 2D models.

The small variations in velocities between the different models for different modes show that an non-homogenized model might not be necessary to use since the computational effort is very high for this model. Instead, it might prove sufficient to use the homogenized model and the 2D shell element model. But the 2D shell element model is flawed for simulating symmetrical modes as described above. The model to be used in the stringer geometry is therefore the 3D homogenized model.

2.5 Damage modelling

The heterogeneous set-up and anisotropic material properties of a composite structure make it predisposed to many modes of defects. Delamination (separation of lamina), debonding (separation of fibres from the matrix material) and fibre breakage are some among a number of structural failures that in one way or another affect the performance of the laminated structure. The severity of a defect is a function of its type, size and location (among other attributes) and can in a broad sense be stated to have taken place when the structure ceases

to perform satisfactorily [15]. However, in the aerospace industry high requirements are specified in order to maintain operational safety of the aircraft. Therefore, unsatisfactorlly performance is considered already at relatively small defects. How to model these defects in a trustworthy and representative way is the topic of this section.

Three modes of failure are considered - delamination, inclusion and porosity. Modelling issues of these failure modes are discussed below.

2.5.1 Delamination

As mentioned in the introduction a delamination arises when the adhesive of two adjoining plies fails. It is mainly caused by impacts and is considered to be one of the most important modes of failure [1],[18]. Modelling a delamination can be achieved in various ways, e.g. by reducing element stiffness or introducing kinematic constraints in specified parts representing the delaminated area.

The *Duplicate Node Method* (DNM) is applied through its effective yet easy approach. DNM models the entire crack front using the concept of duplicate nodes, meaning that nodes representing the delamination are kept at the same position in space, but possess different DOFs. The method is visualized Figure 2.5.1.

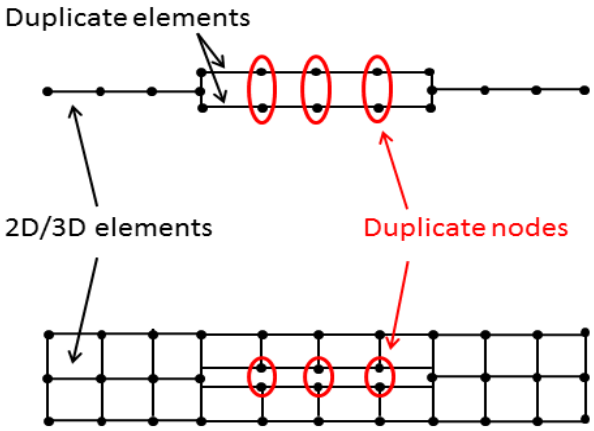

Figure 2.5.1: *Principle idea of the Duplicate Node Method, cross section view. Note that the duplicate nodes occupies the same location in space.*

DNM can easily be applied to both 2D and 3D models. The 3D approach is quite straightforward (separation of nodes) while the 2D approach in addition to duplicate nodes also requires duplicate elements at the area representing the delamination. By defining the thickness and offset of the elements above and below the damage respectively, both the IP and through-thickness location of the damage is defined.

The method gives a high bending-stretching coupling between the elements, which in turn induces mode conversion [18]. This is a great advantage when considering the possibility to detect damage and is therefore highly applicable in this project. The method also enables modelling of multiple delaminations and fibre breakage [18] by adjusting the positioning of the duplicate nodes.

2.5.2 Inclusion

An inclusion usually originates from mistakes during the manufacturing of composites such as accidental teflon inserts [9]. The ultrasonic inspection of inclusions might be difficult in the case of thin inserts, especially for polymer materials who possess similar acoustic impedance as composite materials [24].

The analysis of inclusions is restricted to teflon due to its frequent presence in this type of damage case. Its material properties are: $E = [410, 750]\,\text{MPa}$, $G = [110, 350]\,\text{MPa}$ and $\rho = [2150, 2200]\,\text{kg/m}^3$ [25]. In the inclusion analysis Young's modulus is set to $500\,\text{MPa}$ and the density to $\rho = 2200\,\text{kg/m}^3$. Poisson's ratio is assumed to be 0.25 and Rayleigh damping is assumed with a loss factor of $2\,\%$.

The inclusion is modelled by adjusting the material properties of certain elements to the properties defined above. Inclusion features, i.e. the shape and size, are thereby varied by defining the elements representing the defect.

2.5.3 Porosity

The presence of voids, e.g. air pockets, in the structure is defined as porosity and is measured in terms of volume fraction relative the volume of the entire structure. Voids have a large practical importance for composite structures and should in practice not exceed 5% [26]. Matrix-dominated- and OOP properties such as interlaminar shear strength and through-thickness tensile strength prove to have a higher sensitivity to porosity than longitudinal (fibre dominated) properties [27].

[27] presents an approach for porosity effects on mechanical properties based on the Mori-Tanaka theory. In [28], void characteristics are modelled considering (among others) volume fraction, length-width aspect ratios R_{lw} and width-hight aspect ratios R_{wh} of the voids. The FEA results are compared to an analytical model based on the Mori-Tanaka theory and correlated to experimental data [27],[28]. Without going into details, the investigation yields a relation between void content (volume fraction) and reduction of longitudinal, IP transverse and OOP transverse moduli as seen in Figure 2.5.2.

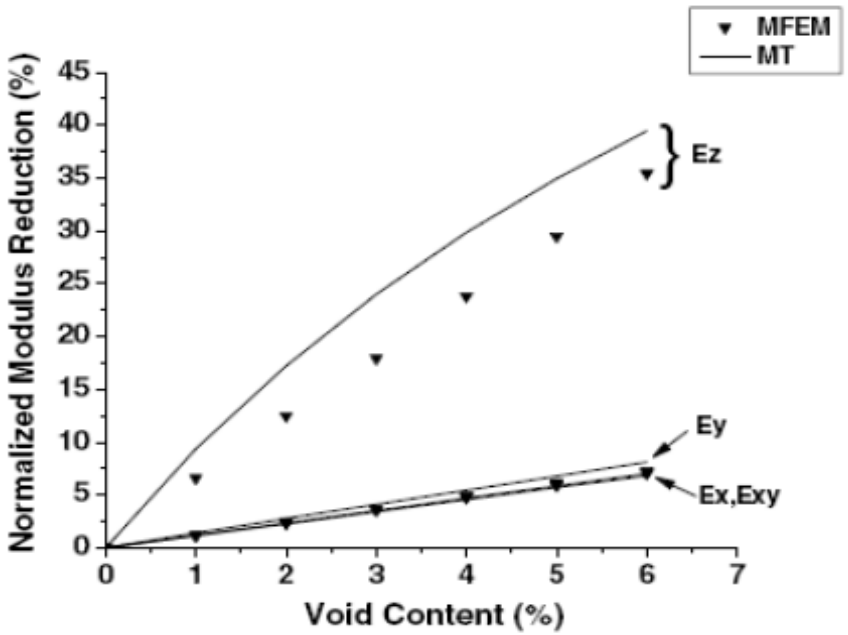

Figure 2.5.2: *Normalized modulus reduction as a function of void content, (MFEM = Numerically obtained values in [28], MT = Mori-Tanaka theory) for $R_{lw} = 6$ and $R_{wh} = 4$ [27]. Used with authorization from Prof. Adrian Mouritz (PhD thesis supervisor).*

A void content of 4% is assumed when analysing the influence of porosity. Based on Figure 2.5.2, this yields a reduction of 5% for the longitudinal (E_1) and IP transverse (E_2) moduli and a 25% decrease of the OOP transverse modulus (E_3).

Somewhat surprisingly, the IP transverse modulus reduction (E_y) is smaller than the OOP transverse modulus reduction (E_z) and is due to the fact that the R_{wh} factor is dominant and thus has a larger detrimental effect on (E_z) [27].

2.6 Damage detection and localization techniques

Structural damage detection techniques are usually divided into two separate categories, global and local damage detection. Global damage detection, meaning that the behaviour of the whole structure is analysed, is considered within the field of structural dynamics. The basic idea in global/vibration based techniques is that an induced damage will cause changes in the physical properties of the structure, e.g. reduction of mass, stiffness and damping, which in turn will affect modal parameters such as eigenfrequencies and mode shapes [29].

Vibration based techniques can be subdivided into modal, frequency, time and impedance domain analysis [30]. Sections 2.6.1 and 2.6.2 explores the potentials in these techniques, with focus on the modal and frequency domain analysis. By observing emerged differences between a damaged and an undamaged plate model, deliberate conclusions can be drawn on whether or not these techniques are reliable and thus justified to apply from a "SHM"-point of view.

The investigation is mainly conducted on the 3D non-homogenized composite plate model described in section 2.1.2. The dimensions of the model are $200 \times 200 \times 2.08$ mm and the element size is set to $2 \times 2 \times 0.13$ mm.

Important issues in local damage detection techniques (in particular wave reflections) are discussed in section 2.6.3, while the concept of time reversal imaging is presented in section 2.6.4.

2.6.1 Modal analysis

A modal analysis is initially performed on the undamaged plate (occasionally called bench model). Eigenfrequencies and modal displacements are extracted from the solution and compared to an analogous analysis of a damaged plate. By varying damage size, through-thickness and IP location, it is possible to investigate what effects a structural defect have on the modal parameters.

Damage size effects

Damage size effects on modal parameters are investigated by simulating delaminations of varying size (4×4 mm, 8×8 mm, 16×16 mm and 24×24 mm) between plies 15 and 16 in the composite plate model. For each separate case, a modal analysis is performed yielding eigenfrequencies and mode shapes for comparison to the bench model results. Table B.0.1, APPENDIX B gives the twenty first flexible eigenfrequencies obtained from this investigation. No rigid body modes are present due to clamped boundary conditions along the four sides of the plate.

It is clear from Table B.0.1 that a 4×4 mm, 8×8 mm or 16×16 mm delamination only causes fractional changes in the twenty first eigenfrequencies when compared to the bench model. However, for a 24×24 mm delamination, distinct frequency shifts occurs for modes above the sixth eigenfrequency. In addition, separate modes display high correlation in terms of eigenfrequencies in some cases. As an example, the thirteenth eigenfrequency of the 24×24 mm delaminated model correlates very well to the eleventh eigenfrequency of the undamaged plate. The appearance of additional modes, termed *delamination modes*, is explained by significant vibrational behaviour in the area of the delamination while the rest of the plate is relatively speaking in rest. The existence of delamination modes is corroborated by calculating the *Modal Assurance Criteria* (MAC) matrix. The MAC calculates the correlation between eigenvector i of the damaged model, ϕ_i^D, and eigenvector j of the undamaged model, ϕ_j^U, according to equation (2.6.1).

$$MAC_{ij} = \frac{\left(\left(\phi_i^D\right)^T \phi_j^U\right)^2}{\left(\left|\phi_i^D\right| \left|\phi_j^U\right|\right)^2} \tag{2.6.1}$$

A MAC_{ij} value of unity implies identical eigenvectors ϕ_i^D and ϕ_j^U, while a MAC_{ij} value of zero indicates orthogonality. The MAC matrix visualized in Figure B.0.1 APPENDIX B indeed verifies the existence of delamination modes (modes 7, 8, 9 and 12 of the 24×24 mm delaminated model). No delamination modes are identified for a 4×4 mm, 8×8 mm or 16×16 mm delamination based on an equivalent MAC investigation.

Aside from the triggered delamination modes, the MAC matrix shows that delaminations only give minor effects to the global mode shapes of the plate. However, distinct local vibrations are still observed, but does not affect the structural behaviour as a whole. The local effect arisen from a delamination is visualized in Figure 2.6.1 below for mode 11 of the undamaged model and mode 13 of the 24×24 mm delaminated plate.

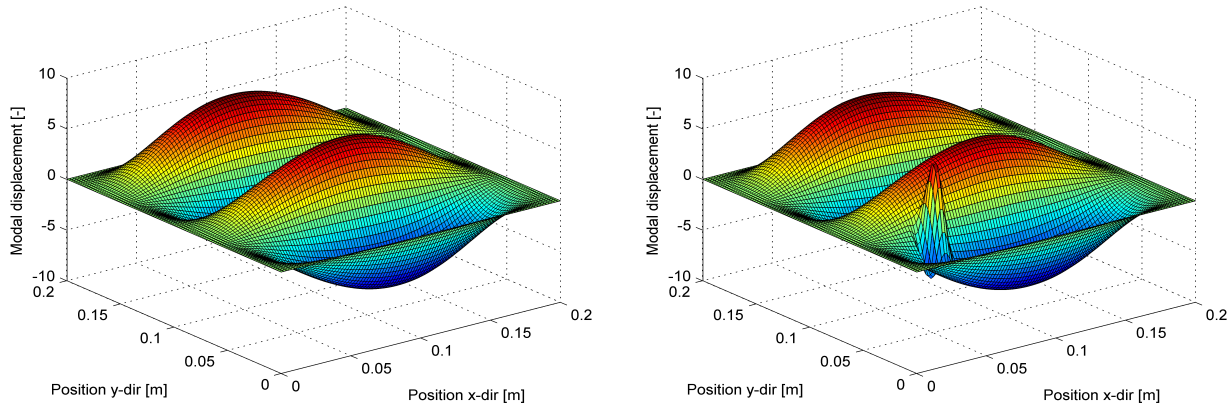

Figure 2.6.1: *Comparison of modes. Left: Mode 11, undamaged model. Right: Mode 13, damaged* 24×24 *mm delaminated model.*

The observation of an unchanged global behaviour during the presence of a delamination is also made in [30] where a composite beam is considered.

Through-thickness location effects

It is also of interest to examine what effects the through-thickness location of a delamination generates. It is at this point confirmed that the delamination size has an, at least local, effect on the mode shapes, and that shifts in eigenfrequencies occur for large damages. The literature states that a delamination close to the surface of the structure results in more irregular mode shapes than an internally located delamination tend to do [30]. To verify this, three separate 24×24 mm delaminatios are simulated with varying through-thickness locations. The IP positions of the delaminations are kept constant while the through-thickness location for each separate case is $z = 1.04$ mm (at the mid-plane), $z = 1.43$ mm (between composite plies 11 and 12) or $z = 1.95$ mm (between composite plies 15 and 16). Resulting eigenfrequencies for each damage case are presented in B.0.2 APPENDIX B

It is clear from Table B.0.2 that for a 24×24 mm delamination located either at $z = 1.04$ mm or $z = 1.43$ mm, no large frequency shifts nor delamination modes arise. Local effects on the other hand prove to be more pronounced. This is explicitly presented in Figure 2.6.2 and supports the statement of a relation between mode shape irregularity and through-thickness damage location.

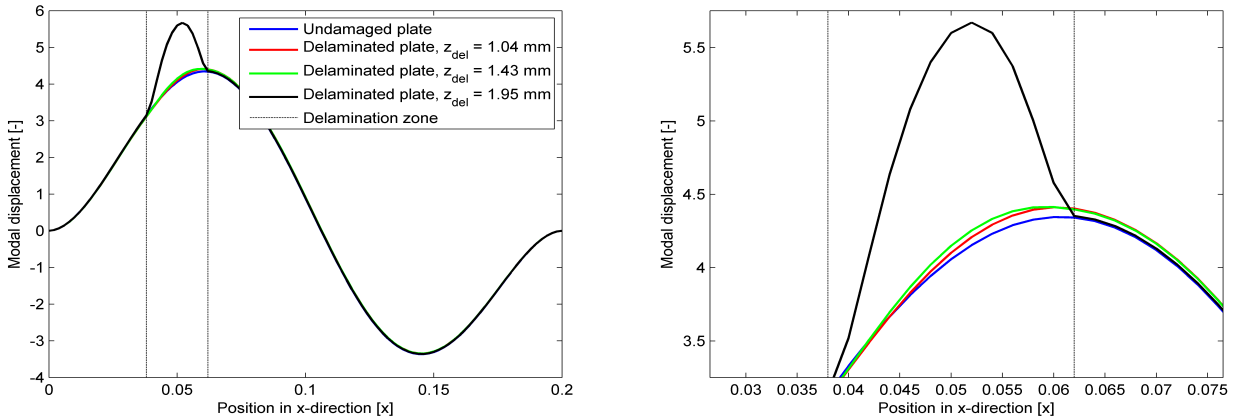

Figure 2.6.2: *Third mode curvature at $y = 0.05\,m$ for different through-thickness delamination positions. Left: Global view. Right: Zoom-in curvature difference.*

IP location effects

Further, the IP location of a damage and its effects on modal parameters are examined. Three locations of interest are defined and a defect is simulated for each separate case. Delaminations of $24 \times 24\,\text{mm}$ in size are (one at a time) induced at $z = 1.95\,\text{mm}$ and IP coordinates $(x, y) = (0.02, 0.05)\,\text{m}$, $(x, y) = (0.06, 0.05)\,\text{m}$ and $(x, y) = (0.1, 0.05)\,\text{m}$. Obtained eigenfrequencies are presented in B.0.3, APPENDIX B.

The results suggest that no direct relation exists between IP damage location and magnitude of the frequency shifts. Instead, a correlation between mode shape and damage position is found. The highest frequency shifts tend to occur in modes where the defect is located in a region of large modal displacements. This is also where the highest mode irregularities are observed as can be seen in Figure 2.6.3 (cross-sectional view of modes 3 and 5).

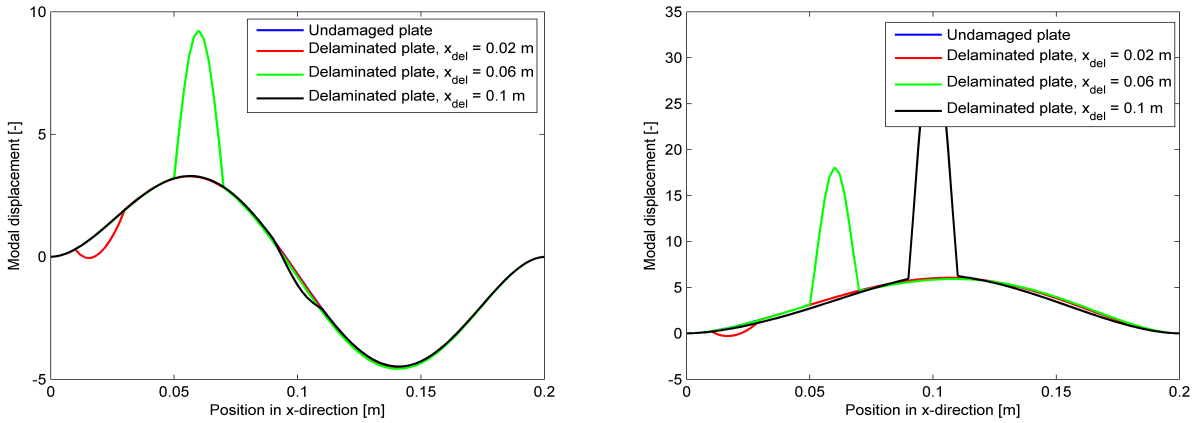

Figure 2.6.3: *Mode curvatures along $y = 0.05\,m$. Left: Third mode curvature. Right: Fifth mode curvature.*

[30] states that the effects of a delamination is stronger for high shear stress regions than high curvature regions. Keeping the results from the through-thickness investigation in mind, this statement is supported by the above presented observations. To clarify, even though a delamination is located in a region of high curvature, it is not a sufficient condition to result in a highly irregular mode shape. Thus the delamination must also be positioned close to the surface where the shear stresses are high.

Modal analysis - conclusions

From the modal analysis observations presented above a number of conclusions are drawn.

1. Delaminations do only have a local effect on the mode shapes.
2. The presence of delamination modes depends mainly on the through-thickness location and the size of the damage.
3. Mode shape irregularities depend heavily on the through thickness location of the delamination, i.e. delaminations closer to the surface yield greater curvature irregularities.
4. The IP location of a delamination determines what modes that give the highest frequency shifts and curvature irregularities. Damages located at a high curvature region (mode shape dependent) combined with a high shear region (through-thickness location) results in the largest frequency shifts and curvature irregularities.

Due to the local effects of a delamination, it is clear that in order to experimentally locate a delamination by just considering the mode shapes, a very fine spatial measurement resolution is necessary. If this is possible, e.g. by using a *Scanning Laser Doppler Vibrometer* [18], modal analysis may be sufficient as long as the delamination is located at a beneficial position. It is however necessary to make sure that the appropriate modes are excited, since detectability as stated above depends on a combination of damage location and high curvature/shear. This requires both an assumption of where the delamination might be located, as well as knowledge of what the mode shapes looks like. In other words, if the presence of a delamination is suspected at a specific position, the structure ought to be excited in such way that this position exhibits desired characteristics.

By considering just eigenfrequencies, it can be concluded that a delamination is present in some cases. Frequency shifts can imply a delamination if it is large enough to give rise to delamination modes and located close to the surface of the structure. Due to the insensitivity to internal damages, applying other damage indicators such as damping and anti-resonances may be a great advantage [31].

The implementation of a modal analysis in a SHM system is questionable. Even though the presence of damage may be detected under the right circumstances, it is not considered reliable enough for SHM in a broad sense. Therefore, no further investigation in terms of damage detection possibilities from a modal analysis is conducted.

2.6.2 Frequency domain analysis

In addition to the modal analysis, a frequency domain analysis is conducted. By analysing the FRFs for a damaged and an undamaged model, not only the dynamic behaviour at resonance frequencies are obtained, but also at other frequencies of interest. The same model is used as in the modal analysis and the analysed frequency range is $0-10\,\text{kHz}$ with a frequency step size of $4\,\text{Hz}$.

The FRFs are measured at nine different locations on the plate. As a start, a delamination of size $24 \times 24\,\text{mm}$ is simulated at position $(x, y) = (0.05, 0.05)\,\text{mm}$ between plies 15 and 16, visualized by a green dot in Figure 2.6.4. In order to assure that all modes are excited, the optimal excitation position is calculated by the *Method of Effective Independence* (EFI). The EFI iteratively calculates the location on the plate giving the best observability of the system based on a number of candidate nodes/sensors, and is thoroughly described in [32]. The EFI is also applied to find the best excitation position. In Figure 2.6.4, optimal excitation position, blue dot, and optimal sensor locations, red dots, calculated by the EFI are shown.

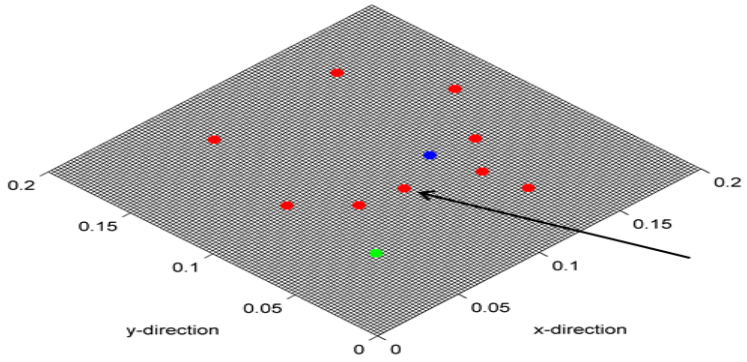

Figure 2.6.4: *Optimal excitation and sensor positions calculated by the EFI. Green dot represents center of delamination.*

The number of sensors has been restricted to ten and in order to increase the speed of the EFI iteration process, every tenth node (in both IP directions) on the upper surface is considered as a sensor candidate node.

The results of FRF analysis is visualized in Figure 2.6.5 below for the receptance (displacement per unit force) of the undamaged and 24×24 mm delaminated plate. The FRF presented are acquired from the fourth sensor pointed to by the arrow in Figure 2.6.4.

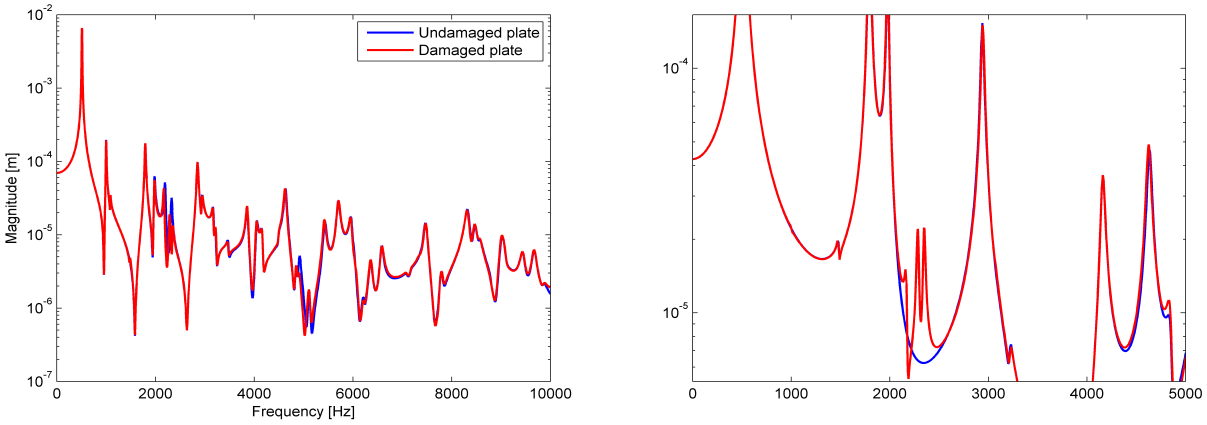

Figure 2.6.5: *Left: Frequency Response Functions for undamaged and delaminated plate, fourth measuring point. Right: FRF zoom-in.*

In Figure 2.6.5 the undamaged and damaged FRFs correlate very well for most frequencies. There is, however, an interesting behaviour in the frequency range between approximately 2000 Hz and 2500 Hz, where additional resonance frequencies seem to occur. This is in accordance to the observations concerning delamination modes presented in the modal analysis investigation. It is however only for the fourth and sixth sensor in the damaged FRF an additional resonance appears, even though the magnitude of these resonances are small. For all the other sensors, there are no additional delamination mode-resonances observed despite the fact that an eigenmode is triggered.

It is concluded in the modal analysis investigation that for delamination modes, significant vibrational behaviour is observed locally, while the rest of the plate relatively speaking is at rest. However, according to the FRF of sensor 4, a delamination mode can also result in resonances at locations not in direct contact to the delaminated area. The magnitude of these modes is, however, very small.

Frequency domain analysis - conclusions

In the frequency domain analysis, the FRFs display expected behaviour. Resonance frequencies are indeed equal to the eigenfrequencies obtained in the modal analysis. The main conclusions drawn from the frequency domain analysis are:.

1. The EFI should be applied prior the analysis to make sure that all modes of interest can be excited and measured.
2. It is clear that in order to detect delamination modes by just analysing the FRF of the plate, it has to be compared to the FRF of the undamaged model. In addition, delamination mode resonances are not visible in all damaged FRFs.
3. For the analysed plate, the most interesting behaviour occurs for frequencies between 2000 Hz and 2500 Hz. This is the area in which the delamination highly affects the FRF. Generally speaking, the maximum frequency shifts occurs in modes with a wavelength of the same size as the delaminated area [30]. This has, however, not been observed in the present investigation.

A frequency domain analysis confirms the conclusions drawn from the modal analysis, rather than yielding new valuable results that may be used in a SHM system. Therefore no efforts are from this point on made to improve the damage detection possibilities based on a frequency response analysis.

2.6.3 Wave reflection characteristics

Unlike vibration based methods, local damage detection comprises techniques referring to NDT such as ultrasonic methods (among those Lamb waves). These techniques focus on local responses instead of the vibrational characteristics in the entire structure.

Before proceeding it is important to distinguish the three following concepts commonly used in SHM, namely:

- Detection
- Localization
- Identification

Detection is merely a means of finding out whether or not damage is present in the structure and should not be mistaken for localization - the procedure to locate the spatial position of the damage. The most challenging concern in SHM is probably related to identification - the issue of determining damage type (delamination, fibre breakage, debonding etc.).

This section only covers damage detection and localization while identification issues are left for further studies. The behaviour of the plate model is examined under the influence of a simulated damage. Since Lamb wave based damage detection techniques utilize wave reflections caused by a damage to detect flaws, this section mainly covers issues related to wave reflective characteristics, e.g. mode conversion, and what modes to excite in order to obtain these. In other words, the ability to detect the presence and location of a damage when analysing reflected waves is investigated.

Mode conversion occurs when a Lamb wave mode hits a structural discontinuity in such a way that it triggers other modes [33]. As an example, asymmetric A_0 modes might hit a structural discontinuity in such a way that symmetric OOP displacements are triggered on adjacent nodes, and thus generate a symmetric S_0 mode. The effects of mode conversion are fundamental in Lamb wave damage quantification, however, mode conversion does not occur for damage that is symmetric through the thickness of the plate [18]. It has for example been shown that a delamination at a position exposed to zero shear stresses, e.g. in the mid-plane of a plate, does not affect a propagating S_0 Lamb wave [19], [1].

Prior to the analysis the relation between damage size and signal frequency content must be considered. Fulfilling equation (2.6.2) ensures an impedance mismatch, i.e. a wave reflection, at the damage boundary.

f represents the frequency content of the signal while c_0 denotes the wave speed and a the flaw size in the direction of the propagating wave.

$$f = \frac{c_0}{2a} \tag{2.6.2}$$

Keeping equation (2.6.2) in mind, the excitation frequency content needs to be adjusted to the flaw size.

The plate model used in this analysis is the homogenized 3D solid element model.

Transmitted A_0 Lamb wave

A delamination size of 5×5 mm is simulated between element layers 3 and 4 in the model, equivalent to a delamination between plies 11 and 12 in the plate. OOP measurements are performed at two separate positions as seen in Figure 2.6.6. OOP responses are acquired on the upper surface as well as on the lower. The plate is excited by predefined displacements described in section 2.2.2.

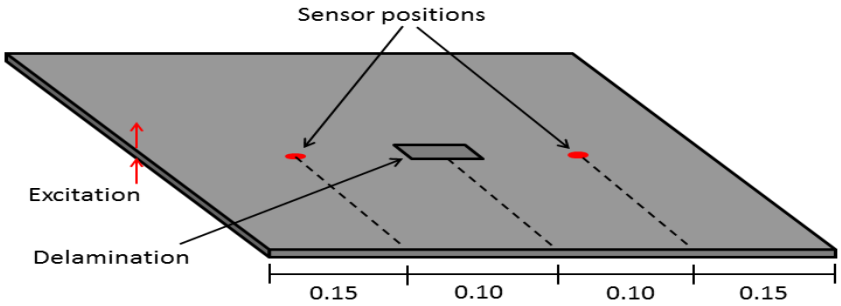

Figure 2.6.6: *Investigation set-up.*

Asymmetrical 5.5 tone bursts with central frequencies of 200, 400 and 600 kHz excite the plate one at a time. Figures 2.6.7 and 2.6.8 show acquired signals for a 200 kHz and a 400 kHz excitation. Measurements are conducted on the upper surface for the undamaged and damaged plate model. Note that the time resolution differs between the plots.

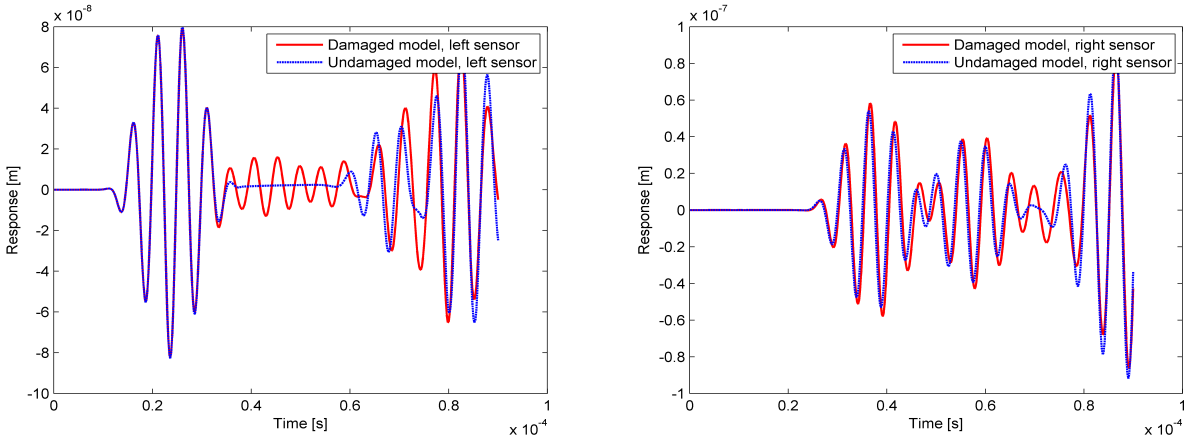

Figure 2.6.7: *OOP responses at the first (left) and second (right) sensor, 200 kHz excitation.*

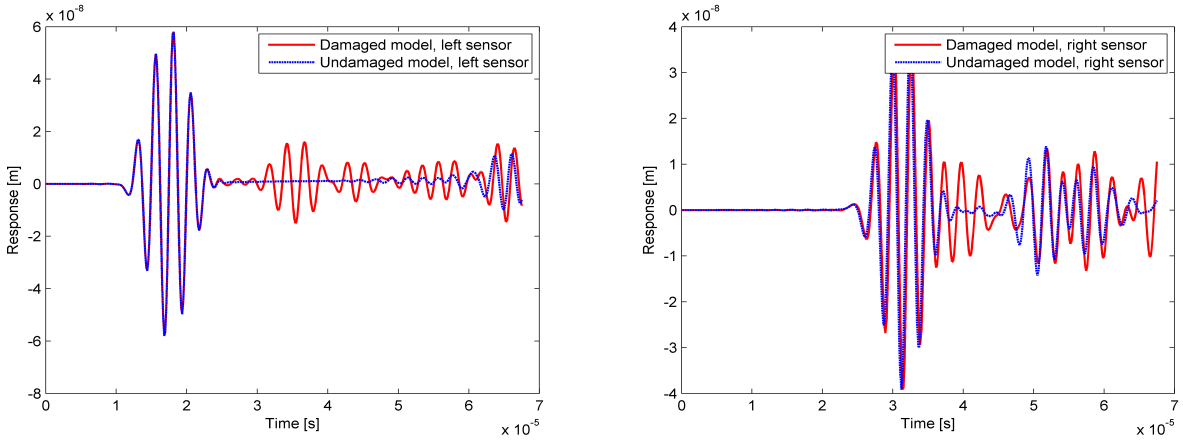

Figure 2.6.8: *OOP responses at the first (left) and second (right) sensor, 400 kHz excitation.*

A number of interesting observations can be made from the acquired signals. Considering the left plot in Figure 2.6.8 (400 kHz excitation, left sensor), the transmitted signal pass at an approximate time instant of $t = 1.5 \cdot 10^{-5}$ s. A reflected wave is subsequently received at approximately $t = 3.5 \cdot 10^{-5}$ s. This behaviour is observed for excitations of 200 kHz and 600 kHz as well. Thus a reflected wave is observed for all tested frequencies. Generally speaking, transmitted and reflected waves tend to mix up somewhat more in low frequency signals (such as a 200 kHz excitation) due to larger spread in the time domain. It is also concluded that for a delamination of size 2.5×2.5 mm, a 200 kHz transmitted signal is not able to detect the damage because of too large wavelengths relative the size of the flaw. In other words, no reflected waves are observed from the delamination. This confirms the relation stated by equation 2.6.2.

Another interesting observation is that mode conversion only seems to occur for an excitation of 600 kHz. This becomes extra clear in the right plot in Figure 2.6.9.

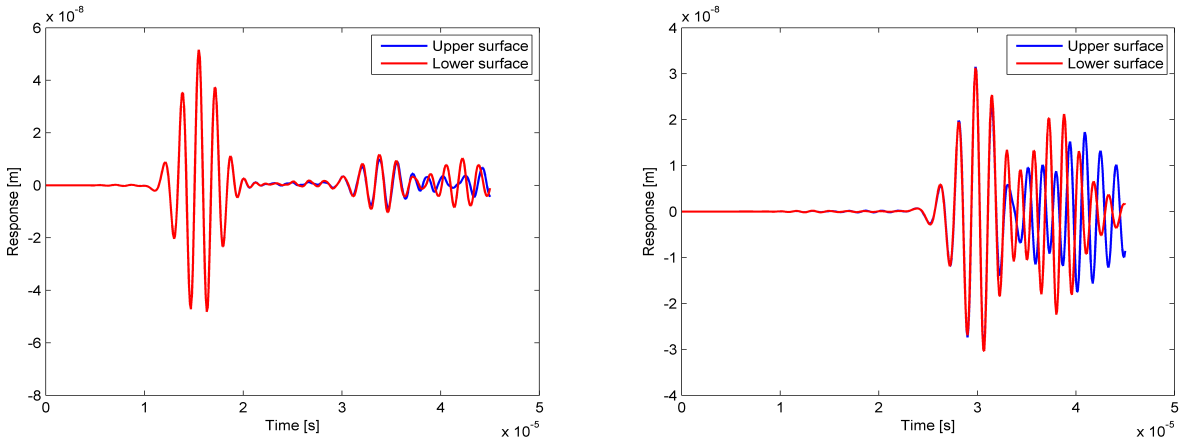

Figure 2.6.9: *OOP responses at the first (left) and second (right) sensor, 600 kHz excitation.*

After the transmitted signal has passed the sensor, waves reflected from the delamination are visible. These OOP displacements have opposite signs for the upper and lower surface, which clearly indicates the presence of a symmetric S_0 mode. The reason for this behaviour is explained by similar phase velocities of the A_0 and S_0 modes at 600 kHz. This is not the case for a 200 kHz or 400 kHz Lamb wave, which explains the absence of mode conversion. Equal phase velocity results in equal wavelengths for A_0 and S_0, i.e. good coherence in the OOP direction. The modes are thus close to each other in the $k - \omega$ domain at this frequency, and are therefore easy to excite simultaneously [9]. Note that this behaviour occurs at 600 kHz for a 2.08 mm thick plate and would consequently already be observed at 300 kHz for a plate with twice the thickness.

Transmitted S_0 Lamb wave

The model is further excited symmetrically with a 200 kHz 5.5 tone burst. A 24×24 mm delamination is modelled between element layers 3 and 4 (corresponding to composite plies 11 and 12). The simulations show no reflected waves neither in front of nor after the delamination. This is probably explained by the particle motion of the S_0 Lamb wave mode. For low *fd* products like in the present case (200 kHz, 2.08 mm thickness), the IP particle motions of a symmetric wave is more or less parallel, see section 1.5.4. Thus very low shear stresses are present. As mentioned earlier, a delamination positioned in a zero-shear stress region has no effect on a propagating S_0 Lamb wave which in a way is confirmed here.

In order to increase the shear stresses, and thus obtain wave reflections, the delamination is positioned between composite plies 15 and 16. This requires simulations in the 3D non-homogenized model. The investigation shows that reflected waves do occur both in front of and after the delamination. The amplitudes of these waves, however, are extremely small in comparison to the transmitted S_0 wave and the possibility to detect these reflections in an experimental set-up is therefore questionable.

To ensure that unsuccessful damage detection of internally located flaws is not caused by a too low excitation frequency, the homogenized 3D model is excited with a high frequency symmetric 5.5 tone burst of 600 kHz. A 6×6 mm delamination is simulated between element layers 3 and 4 and should be sufficiently large for detection. The results shows that reflected waves in fact are present to a greater extent than for the 200 kHz investigation, but still relatively small in comparison to the transmitted signal. However, it should be noted that the amplitude of a S_0 wave is smaller than for an A_0 wave when the same excitation force is applied.

Wave reflection characteristics - conclusions

The following conclusions are drawn from the investigation presented above.

1. For an asymmetric excitation, reflections are observed for all tested frequencies as long as equation (2.6.2) is fulfilled. However the reflected waves are easier to distinguish in higher frequency excitations due to a more narrow span in the time domain, i.e. a "mix" between transmitted and reflected waves is avoided. Therefore, low frequencies should only be used if relatively large damages are sought for, and the sensors are advantageously positioned at a distance from the suspected delamination position to increase measurement interpretation. If the presence of smaller damages is suspected, high frequency signals ought to be transmitted as a result of equation (2.6.2). This enables at the same time closer spatial measurements to be performed.

2. Mode conversion is only observed for an excitation frequency of 600 kHz, both in the asymmetric and symmetric case. This is due to good coherence in the OOP direction (and in the $k-\omega$ domain) between A_0 and S_0 at this frequency. The presence of mode conversion is fundamental when analysing measurement data, especially when the damage location is determined by the signals time of flight.

3. In the symmetric case no wave reflections are observed for a 200 kHz tone burst excitation and a simulated delamination between element layers 3 and 4. An analogous investigation for the 3D non-homogenized model, now with a delamination between composite plies 15 and 16, show on the other hand, the appearance of wave reflections. However, these have an amplitude that are considered too small to detect in an experimental NDT case scenario and is therefore not appropriate for damage detection.

The applicability of ultrasonic methods in SHM, particularly the Lamb wave based methods discussed here, show large potential. SHM issues treated in the stringer model are therefore concentrated to local damage detection techniques, rather the somewhat unreliable global techniques discussed in sections 2.6.1 and 2.6.2. It should, however, be mentioned that more complex wave propagation characteristics are to be assumed in the stringer. This assumption is based on two facts. First of all, the stringer comprises complex geometries. Such simple wave propagation patterns as those observed in the plate can therefore not be assumed. Reflections will be present to a much higher extent due to geometric boundaries and must be distinguished from damage generated reflections. Secondly, many parts of the stringer are, geometrically speaking, thick in comparison to the modelled plate. High *fd* products are therefore present already at excitations of say 200 kHz. Multi-modal behaviour (presence of A_1, S_1, A_2, S_2, etc.) is therefore to be assumed which aggravates the analysis significantly. These issues are further discussed when considering damage detection in the stringer model.

2.6.4 Time Reversal Imaging

The concept of time reversal imaging, as a means of detecting and locating damage, has many important applications in medicine, geophysics, NDT, underwater acoustics and wireless communications, to name a few [34]. The analysis of time reversal acoustics and its retro-focusing properties in solid specimens is very important for the development of new NDT techniques. Potential applications beside SHM for aerospace, spacecraft or infrastructure are biomedical diagnostic imaging and for medical therapeutic purposes.

To illustrate the procedure of time reversal image reconstruction an experiment is conducted with the aid of [35]. The procedure is split into two parts. The first part covers the actuation of the signal from a source, represented by vasculature. The signal is emitted and scattered in multiple directions. The *Time Reversal Mirror* (TRM), consisting of an array of transducers with the ability to both read and emit data, is placed conveniently in a circle confining the excitation source (vasculature) within its borders, see Figure 2.6.11 (left). The TRM collects data from the displacement vector for each transducer in the time domain and stores it for the second part of the process. Once a sufficient amount of data is accumulated it is time-reversed and remitted from the TRM, as illustrated in Figure 2.6.10. This will allow for a reconstruction of the excitation source from which the signal originated, see Figure 2.6.11 (right). The retro-focusing of the source takes place automatically since all the information about the the position of the source is encoded in the signal themselves as recovered in the first part. This is known as the *Time Reversal Process* (TRP) [36].

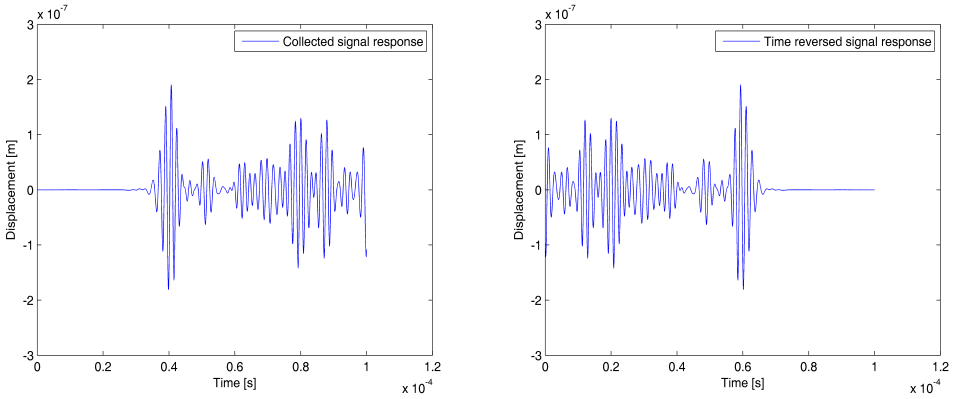

Figure 2.6.10: *Collected signal response from the transducers (left) and its respective time reversed signal response (right).*

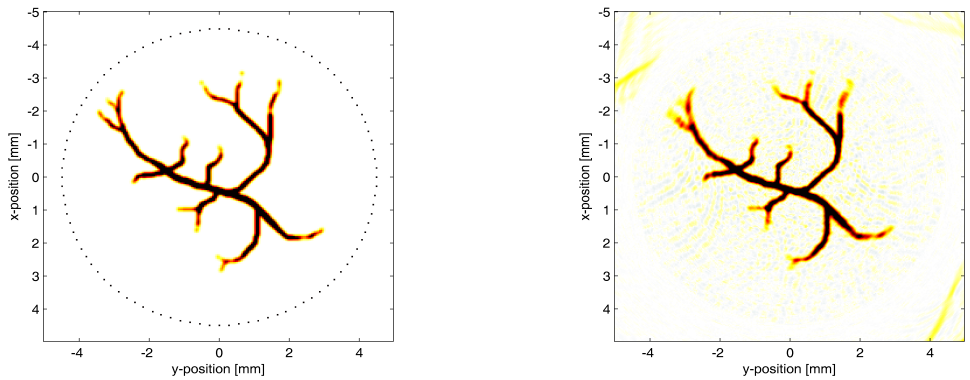

Figure 2.6.11: *Time reversal imaging with 100 transducers surrounding the source. The source actuation process (left) and the source reconstruction process (right) [35].*

A restriction for the spatial resolution in time reversal imaging is the TRM. Ideally, the TRP should reconstruct the source perfectly, would the TRM consist of an infinite set of transducers surrounding the source. In numerical calculations such as FEM the nodes can be replaced by transducers. There can, however, only exist

a finite size of elements and thus the loss of spatial information from the propagating waves increases with the element size of the FE-model. If the number of transducers decreases the TRP will still hold, but with decreased efficiency in terms of spatial resolution (see Figure 2.6.12).

The quality of retro-focusing is affected by the *aperture*. If the source is very distant from the TRM and would the TRM consist of a short length of transducers, then as a consequence the spatial resolution will decrease. In SHM applications, due to the small geometries of the specimens, it can at times only be possible to attach one or two PZT discs. This implies a negative effect on the spatial resolution. A way to counteract this is by recording the signal response for a longer period of time, such that multiple reflections or scattering reach the TRM. It has been shown that multiple scattering has a positive effect on the spatial resolution [37].

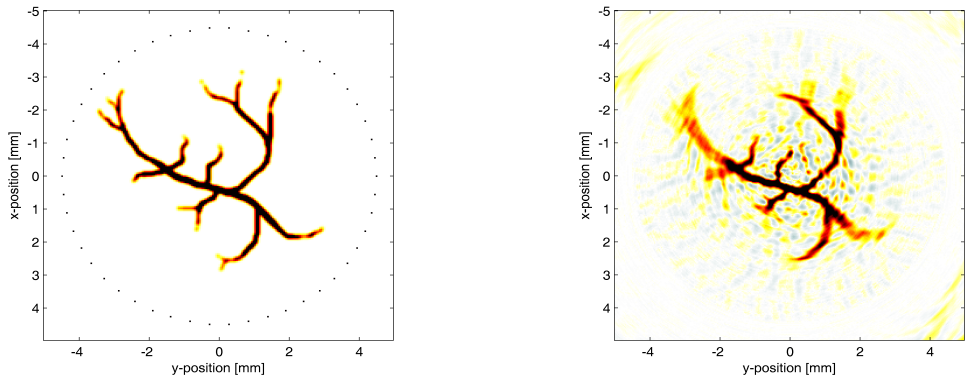

Figure 2.6.12: *Time reversal imaging with 40 transducers surrounding the source. The source actuation process (left) and the source reconstruction process (right) [35].*

In SHM the fact remains that the source (damage) location is considered to be unknown. When the source is reconstructed through the TRP knowledge of the location is already at hand and thus this approach of time reversal image reconstruction is not applicable in SHM. This is known as *active source imaging*. Suppose instead that the actuation source is not of main interest but the damage itself is. When the source signal interacts with the damage it will act as a secondary source, scattering the signal similarly to the primary source. This is known as *echo mode imaging* [37] and the location of the damage is not an issue any more. A requirement for this configuration is that the signal from the primary source must reach the damage before data can be collected in the TRM.

The method of echo mode imaging is different from that of active source imaging. Active source imaging is quite straightforward and has already been explained. Echo mode imaging requires a pristine (benchmark) model to recreate the damage. This will be explained in detail later. The downside to this approach is that the time when the retro-focusing converges on the secondary source (the damage) is not known since the location of the damage is considered to be unknown. The ideal is to find a method that extracts the time-frame for the exact moment when the waves retro-focus on the damage. This can be accomplished through calculating the *Shannon entropy* for each time-frame. The method of Shannon entropy is not analysed further and can be studied in [37].

A means to overcome the use of Shannon entropy is achieved by creating an envelope that extracts the time-frame with the maximum displacement for each individual node. A four-step algorithm derives the damage localization process through time reversal imaging with the use of a pristine model:

1. Excite the primary source (transducer) and collect displacement data $I(t)$ in TRM for a sufficient amount of time for the pristine model.
2. Repeat the first step but for the model containing damage. Collect the displacement data $V(t)$ in TRM.
3. Calculate the residual $R(t) = I(t) - V(t)$. $R(t) \neq 0$ indicates the presence of damage.
4. Time-reverse the residual, $R(T - t)$, and remit it through the TRM.

This method is also performed for a 2D composite plate model in Radioss to test its validity. The excitation source is the left boundary and an A_0 mode tone burst with a central frequency of 600 kHz is triggered. The TRM is defined by all the nodes in the left and right boundaries. A delamination with arbitrary size is simulated for the damaged model (see Figure 2.6.13).

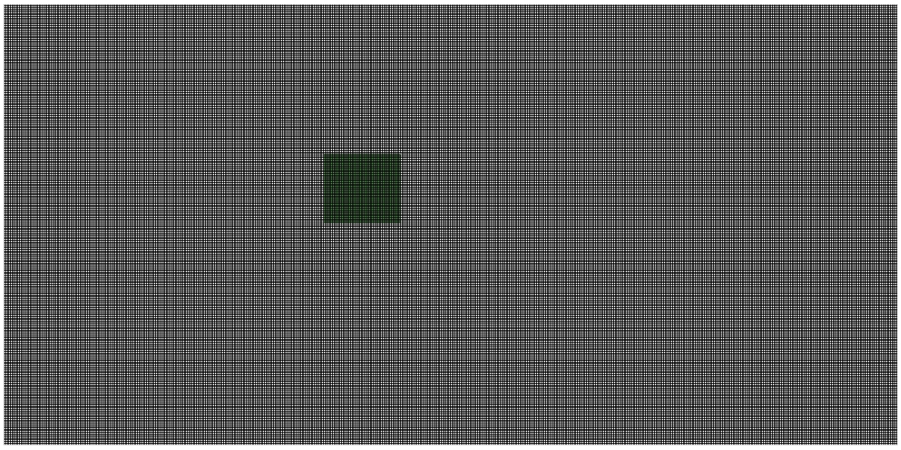

Figure 2.6.13: *Delamination (green square) in Hypermesh for a 2D composite plate model.*

The time-revered residual refocuses and creates maximum displacements at the location of damage. A tool in Hyperworks allows for plotting the maximum displacement for each node in the entire time domain (see Figure 2.6.14).

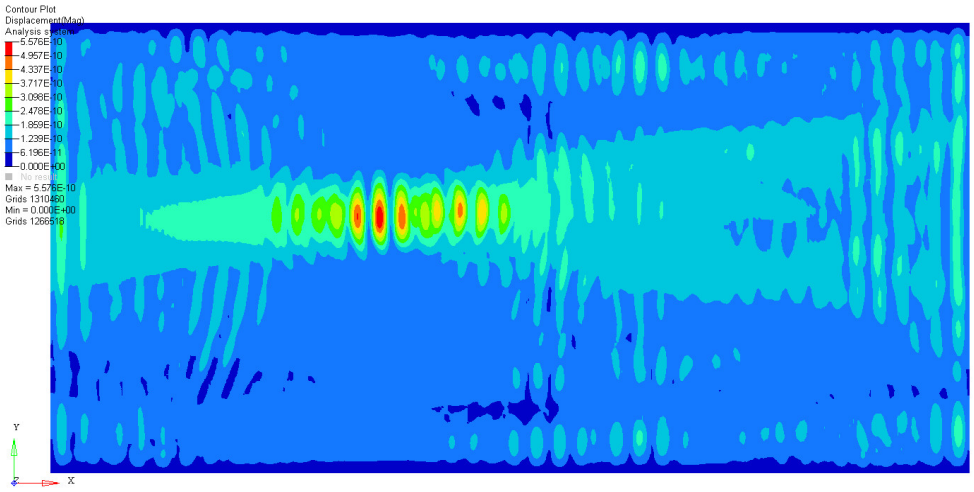

Figure 2.6.14: *Time reversal reconstruction in Hyperworks for a 2D composite plate model.*

This damage localization technique is tested for delaminations in several locations and for different types of defect. The reconstruction process shows positive results for each case.

3 Stringer model

Shapes and sizes of stringer components can be defined in numerous ways. Some aircraft utilize T-shaped stringers in the fuselage assembly, yet Z- and "hat"-shapes are often equally used.

The present work covers a T-shaped aircraft composite stringer. Geometric definitions and material properties are assumed generic and defined via expertise consultation [9]. From prescribed stringer attributes a 3D model is generated in Hypermesh, in which material properties and correct geometric shapes are defined. The model consists of four sections, see Figure 3.0.1.

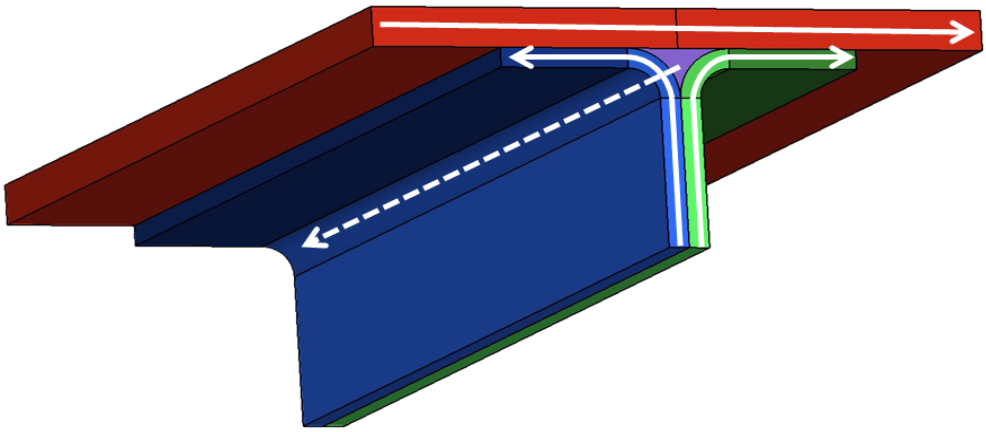

Figure 3.0.1: *Stringer component and governing fibre directions*

Top surface section

The top surface section (red) represents the fuselage. It is composed of an IP fibre stack-up of $[90/45/0/135]_{8s}$ and a total thickness of 8 mm. The governing direction (0°) is visualized by an arrow in Figure 3.0.1.

Left and right stringer sections

The left and right stringer sections (blue and green) are each 4 mm thick and stacked $[90/45/0/135]_{4s}$. The composite lay-up follows the curved section and perfect bonding is assumed between the top surface and the left/right stringer sections. Perfect bonding is also assumed in between the left/right sections. Two arrows represent the governing fibre directions of these parts in Figure 3.0.1.

Triangular/Bermuda triangle stringer section

The triangular stringer section (purple), from here on denoted the Bermuda triangle, is geometrically complex. Problematic manufacturing procedures and relatively weak material properties makes it prone to sustain flaws. These often emerge in the bond between the Bermuda triangle and the adjacent stringer parts.

Two cases for the Bermuda triangle are considered:

1. 0 % fibre volume, $V_f = 0$.
2. 25 % fibre volume, $V_f = 0.25$.

Unidirectional fibres are assumed in the direction of the dashed arrow, illustrated in Figure 3.0.1. The stringer model is built out of 3D homogenized solid elements based on the results presented in section 2.4.2.

3.1 Guided Ultrasonic Waves

The potential of GUW and their applicability in a SHM system proves to be vast. The plate case study explicitly demonstrates that delaminations encountered to an asymmetric A_0 Lamb wave generates wave scattering from which the presence of a defect can be assessed. Fundamental Lamb waves are transmitted in the stringer geometry in a bid to explore damage detection possibilities based on these observations. However, even though the stringer comprises many plate-like components, considerable differences in wave propagation characteristics are obtained. As stated in previous sections, complex wave patterns emerge for two main reasons - geometrically complex boundaries and component thickness variations. Pure A_0 modes are therefore very hard to generate and as a consequence the concept of ToF for damage localization turns out to be infeasible.

Due to the frequency-thickness relation in Lamb wave propagation, the generated composite dispersion curves are in fact not unique for the tested plates. The curves can easily be transformed into a frequency-thickness relation (under the condition that the exact same material and composite lay-up is applied), yielding a dispersion curve for the fundamental A_0 mode given below.

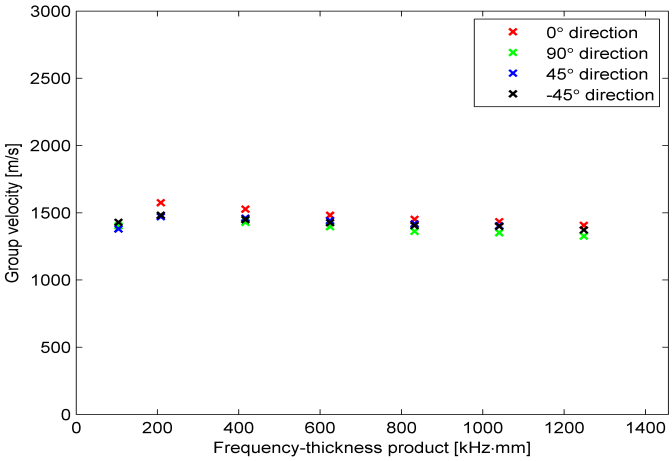

Figure 3.1.1: *Dispersion curve for 3D non-homogenized composite plate, A_0 mode, frequency-thickness dependency.*

Higher order modes are for the 2.08 mm examined plate obtained at approximately 600 kHz, or at a frequency-thickness product of 1.2 MHz-mm. An equivalent *fd* product for an 8 mm thick geometry, such as some plate-like parts of the stringer, is thus obtained already at approximately 150 kHz. This partly explains the observed multi-modal behaviour in the stringer. It should be mentioned that the defined element size primarily is adjusted to the (velocities of the) fundamental Lamb modes and to the pure longitudinal and shear wave velocities. The spatial resolution might therefore be too coarse to resolve all high order modes even though the *fd* product is sufficiently large.

Waves are also observed that may be interpreted as pure longitudinal or shear waves, especially for a top surface excitation right above the left and right stringer sections. It is, however, hard to distinguish these GUW from higher order Lamb modes as a result of similar wave velocities at certain frequencies.

Figure 3.1.2 visualizes the effects of non-parallel boundaries, where reflected waves simultaneously propagates in multiple directions (white dashed lines). In addition, as a result of different material properties (high matrix/epoxy content), impedance mismatch and thus wave reflections arise at the Bermuda triangle, even though they are small in comparison to damage generated reflections. Nevertheless, the fact remains that reflections do occur and has to be taken into consideration in the processing of acquired data. Assuming that measurements are taken at an arbitrary point on the upper surface, acquired data needs to be processed in such a way that it finds the originating source of the signal. Based on the multi-modal characteristics, complex geometries and "natural" impedance mismatches within the structure, the problematic nature of a ToF analysis for damage detection is obvious. Also, significantly higher wave velocities are observed in the IP

(fibre dominated) directions than in the OOP transverse (matrix/epoxy dominated) directions.

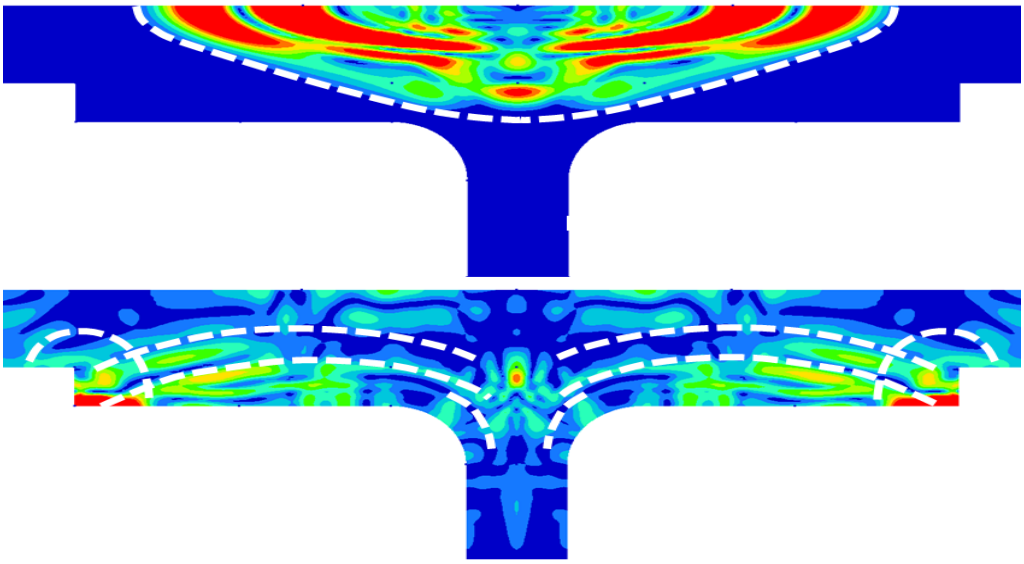

Figure 3.1.2: *Multi-directional wave scattering (magnitude) at time instant* $4.8 \cdot 10^{-6}$ *s (upper) and* $1.176 \cdot 10^{-5}$ *s (lower).*

Damage localization procedures such as the concept of ToF are beneficial in single mode scenarios, unfortunately, due to reasons just discussed, they are more or less impossible to implement in a complex structure for SHM purposes. Nevertheless, the established FE stringer model has proven to be a valuable tool in the continued work within LOCOMACHS and has contributed to great interpretation possibilities for future SHM issues.

3.2 Sensitivity analysis

Section 2.6.3 covers issues of symmetrical and asymmetrical Lamb wave propagation in a composite plate. In particular, conclusions are drawn regarding the interaction between a transmitted S_0/A_0 wave and a simulated delamination. Even though realistic simulations are managed in the case study, similar and equally straightforward results from a corresponding investigation in the stringer are hard to achieve. This assumption is based on the following two facts:

1. The stringer comprises a larger number of and more geometrically complex boundaries.
2. The stringer is generally speaking more complex in terms of thickness, curvature radii and material property variations.

These stringer attributes make the wave propagation characteristics difficult to predict. Non-parallel boundaries generates wave scattering in multiple directions. In addition, sudden changes in geometry thickness will cause shifts in the *fd* product of the plate-like stringer parts. Consequently, group and phase velocities differ between separate parts and thus complicate damage localization procedures, such as those practising the principles of Time of Flight (damage localization through known wave speed and propagation time). Nevertheless, wave propagation characteristics are analysed in the stringer in order to evaluate the potential of GUW in SHM. Section 3.1 highlights observed changes in signal response caused by a damage. General observations of physical features are here covered in a more "discussion-like" approach, where causes for emerged signal changes are explained.

It is of interest to analyse the stringer from a comprehensive perspective and see how different parameters affect the signal response. A sensitivity analysis is therefore performed in which the relation between excitation position, damage type and damage position is examined. Basically, a large number of simulations are conducted for a variety of parameter combinations and a *Damage Index* (DI) is estimated for each individual simulation. Measurements are acquired from the entire surface of the stringer, resulting in an overall picture of

parameter implications.

A sensitivity analysis is performed in order to curb the complex nature of the stringer. Without an extensive, structured and well planned inquiry the observed structural responses are very hard to interpret. The fundamental idea behind the analysis is to investigate the sensitivity of the stringer in terms of damage type, damage position, excitation position and excitation frequency (denoted variable parameters). By doing so, it enables an evaluation for what combination of parameters damage detection is possible. As an example, are the structural changes caused by an inclusion substantial enough to consider it detectable and if so, where should measurements be conducted to optimize detectability for a predefined transmission position? It is questions like these the sensitivity analysis ought to answer.

A schematic plan of the sensitivity analysis is given in Figure 3.2.1.

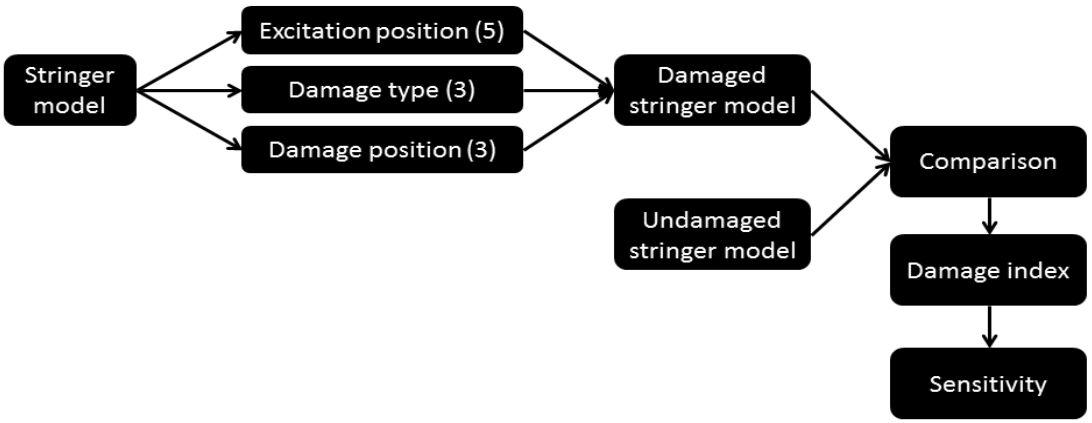

Figure 3.2.1: *Schematic plan for broadband sensitivity analysis*

The stringer model (occasionally denoted bench model) used in the sensitivity analysis is the 3D homogenized stringer model described in section 3. The stringer is excited by a broadband pulse as described in section 2.2.1 in order to cover a large frequency spectrum. Only a cross-section of two elements is used, thus translational DOFs in the y-direction are constrained to zero, see figure 3.2.2. This is of course not ideal in an "accuracy"-point of view. However, it should be mentioned that a total number of 50 simulations are required to complete the analysis (5 undamaged simulations + $5 \cdot 3 \cdot 3$ damaged simulations = 50 simulations). A compromise is therefore unfortunately necessary between accuracy of the results and modelling/solving time effort. Simulating wave propagation for a broadband excitation (frequency content up to 600 kHz) on a full scale stringer model would require approximately four days of computational calculations per simulation and is therefore not practicable. Maximum element side length is set to 0.25 mm, where consideration is taken of equation (2.2.2).

Excitation and defect set-up for the sensitivity analysis are visualized in Figure 3.2.2.

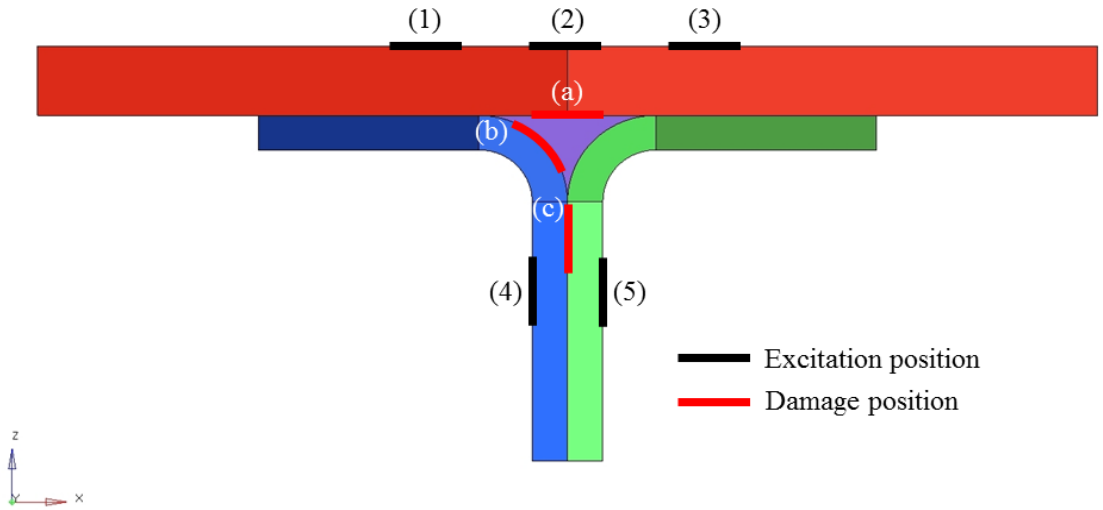

Figure 3.2.2: *Broadband sensitivity analysis set-up*

Three different types of damage are investigated — delaminations, inclusions and porosity, see section 2.5 for modelling procedure of each separate damage type. Porosities and inclusions are assumed to be 9 mm in length and 1 mm thick, while delaminations only yield a length-wise definition of 9 mm. For each parameter combination (45 combinations in total), the results are compared to an equivalent simulation of the bench model. In this analysis, results along the entire surface of the stringer are obtained.

Damage index

Damage severity can be measured in the time as well as in the frequency domain of the acquired signal. Numerous techniques are proposed in the literature, in which all in one way or another possess the ability of damage detection/classification. Here, a simple yet efficient procedure is applied for sensitivity measurements. The *Root-Mean-Square Deviation* (RMSD) is used in [39] to calculate the DI in a quasi-isotropic composite plate when excited and measured by *piezoelectric wafer active sensors* (PWAS). The sensitivity in node i is calculated by equation (3.2.1) and is as earlier mentioned obtained for each parameter combination.

$$DI_i = \sqrt{\sum_{j=1}^{N_{timesteps}} \frac{\{Re\,(t_j) - Re^0\,(t_j)\}^2}{\{Re^0\,(t_j)\}^2}} \tag{3.2.1}$$

$Re\,(t_j)$ denotes the OOP response at time step j for the damaged model, and $Re^0\,(t_j)$ the response of the undamaged bench model, both in node i. The RMSD is advantageously used for DI calculations since no preprocessing of acquired data is necessary [39].

3.2.1 Results

A sensitivity analysis is performed in which numerous parameter combinations are tested for. A large number of results are thereby obtained, however, not all of these are presented here. A representative collection of plots are chosen in an attempt to cover all types of detects (delaminations, inclusions and porosity), defect locations and excitation positions.

Two results per damage case are presented. Note that the DI bar differs in maximum values between the plots. Notations in figure captions (damage and excitation position) refers to Figure 3.2.2, section 3.2.

The DI's are calculated for 500 time steps out of a 1000 time steps simulation. Reasons for not including all time steps in the DI calculations are discussed in section 3.2.2.

Delamination

Delaminations affects the transmitted signal in a noticeable manner. For flaws located at position (a) or (b), large time signal differences are observed between the damaged and the undamaged stringer model. These effects become apparent especially in the left and right stringer sections for top surface excitations ((1),(2) or (3)).

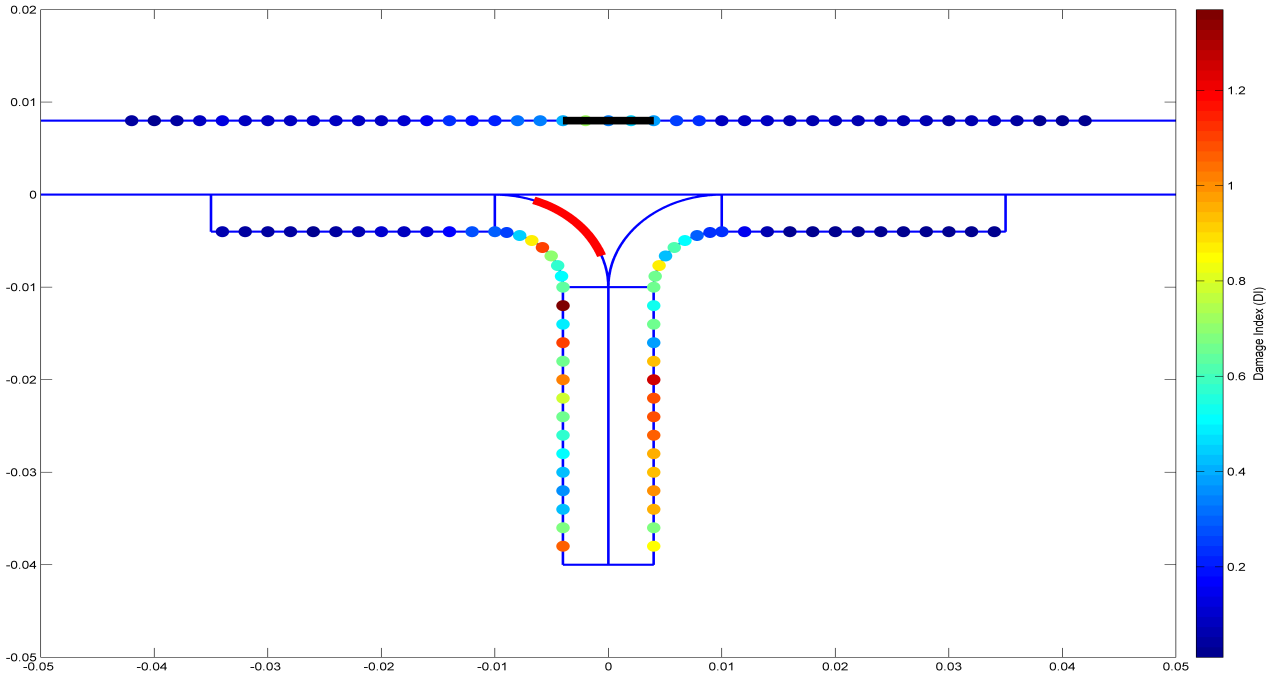

Figure 3.2.3: *Damage index for delamination, position (b), excitation in (2)*

Distinct wave scattering occurs in a perpendicular direction relative the modelled delamination. For instance, note the high DI's on the upper surface just above the modelled defect in Figure 3.2.4.

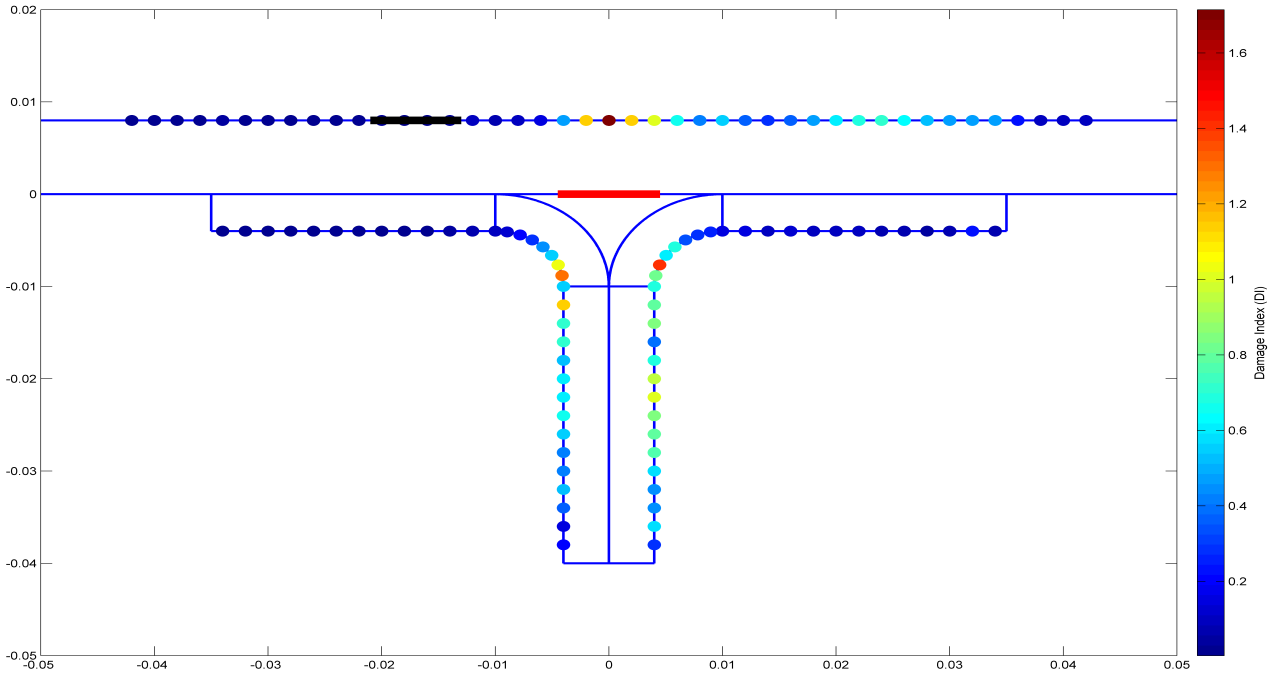

Figure 3.2.4: *Damage index for delamination, position (a), excitation in (1)*

Inclusion

Similar to delaminations, inclusions prove to have a large influence on the sensitivity. For the presented plots in this section, even higher DI's are obtained for inclusions than for delaminations. It should be mentioned that the teflon inserts comprise material properties that are significantly different from those of the composite material, thus a large impedance mismatch occurs which in turn generates wave reflections.

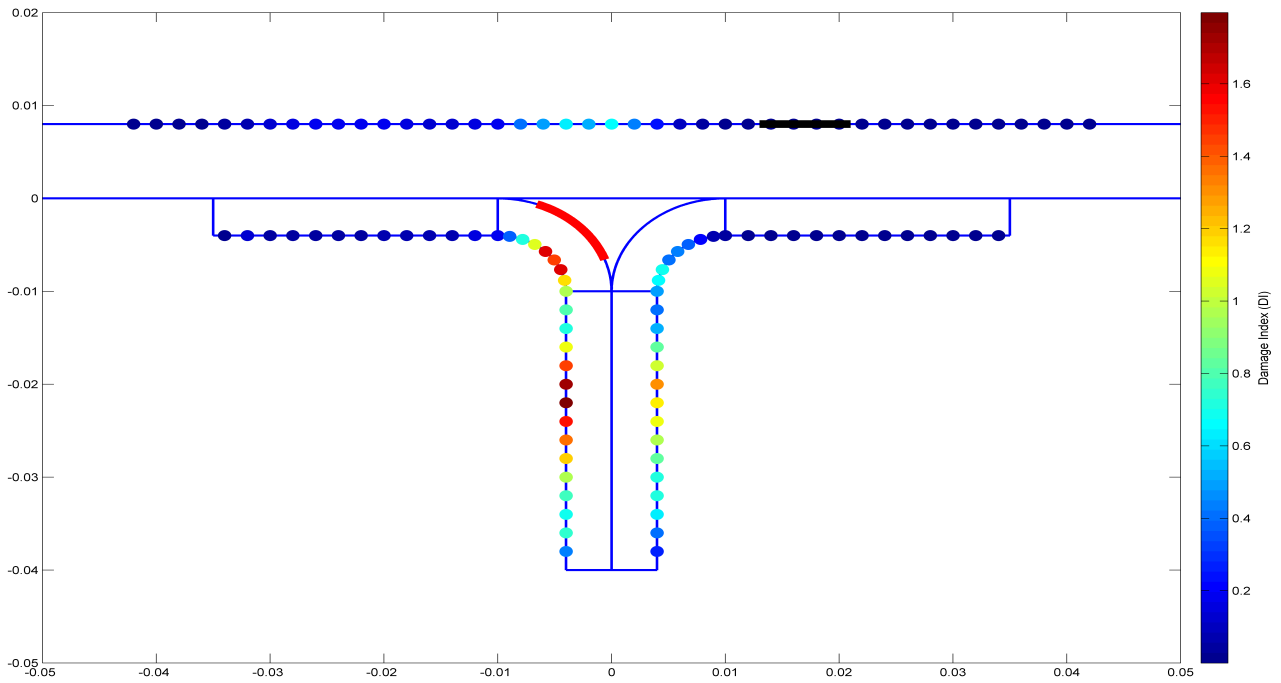

Figure 3.2.5: *Damage index for inclusion, position (b), excitation in (3)*

High DI's may also originate from the fact that the modelled inserts occupy a volume (9 mm length and 1 mm), in contrast to delaminations. As a combination of relatively low values of the engineering constants and considerable volume content, the sensitivity results seem logical.

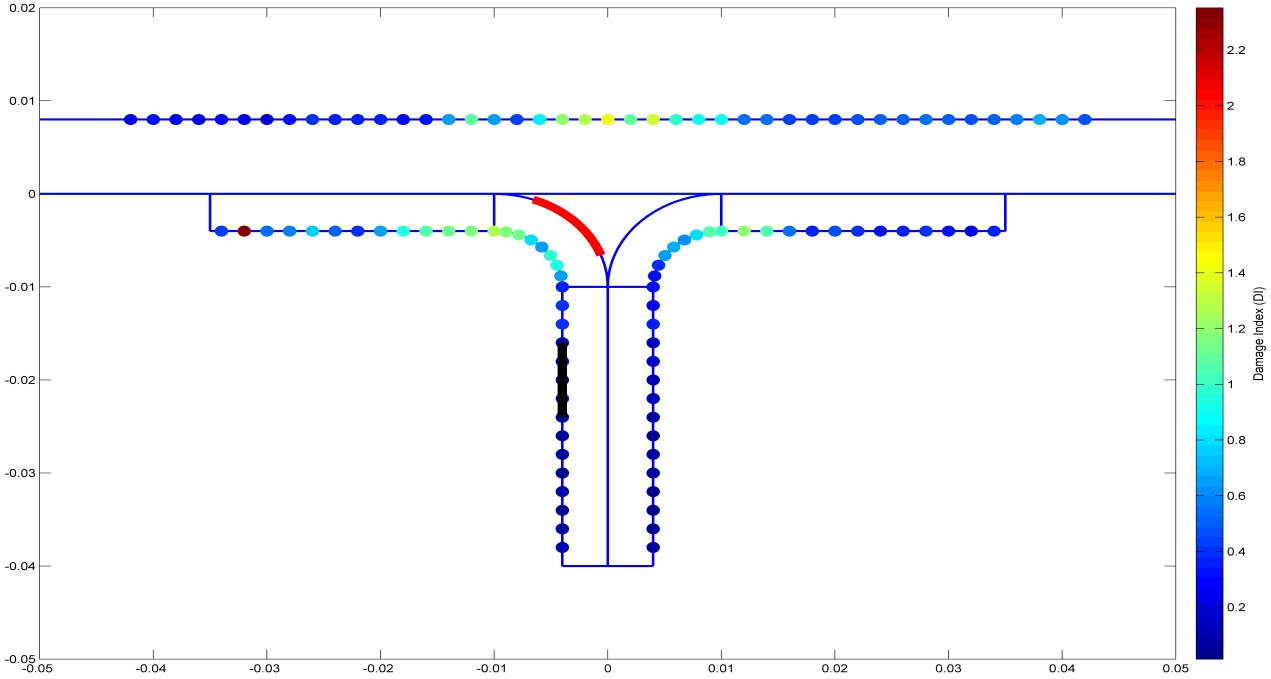

Figure 3.2.6: *Damage index for inclusion, position (b), excitation in (4)*

Porosity

Limited sensitivity to porosity is observed in the stringer. Except for local effects in the vicinity of the porous area, only small changes in the structural response appear to occur. This is particularly clear in Figure 3.2.7.

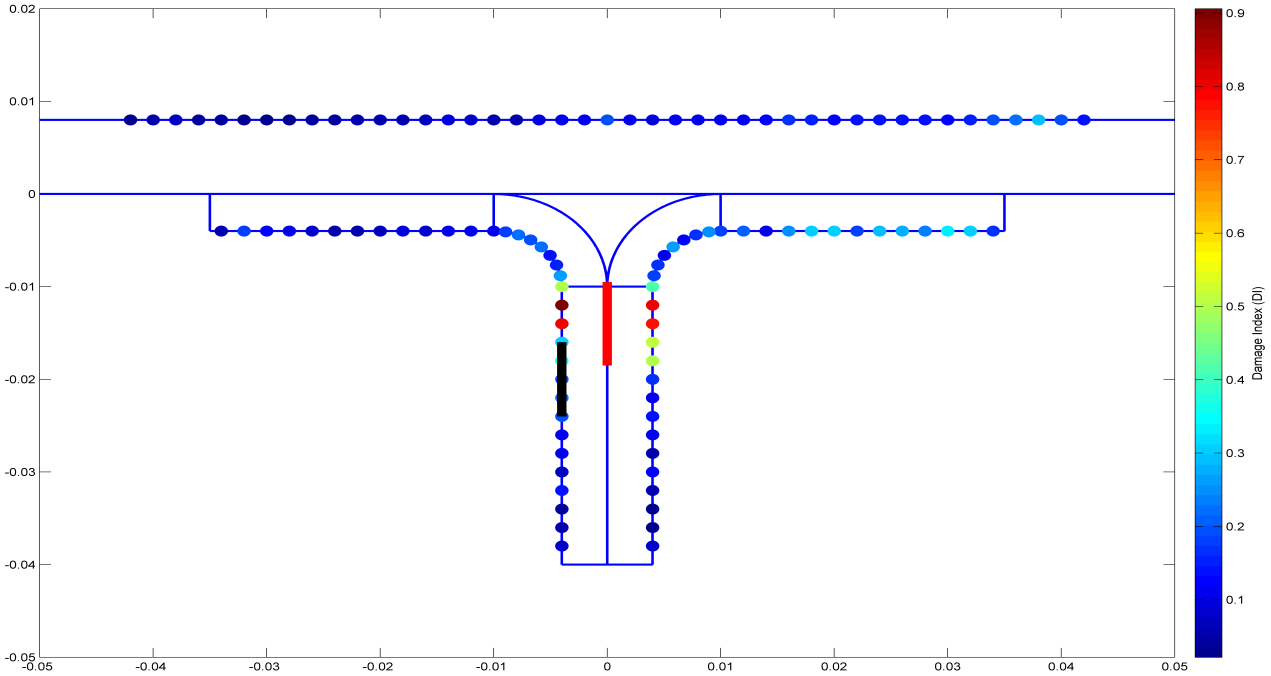

Figure 3.2.7: *Damage index for porosity, position (c), excitation in (4)*

More global porosity effects are observed in Figure 3.2.8. Here, wave packets propagating in the direction of the left/right stringer sections do to a large extent interact with the modelled porosity. High DI's are thereby obtained in conformity with Figure 3.2.3. The DI's, however, are significantly lower than those caused by an inclusion or a delamination.

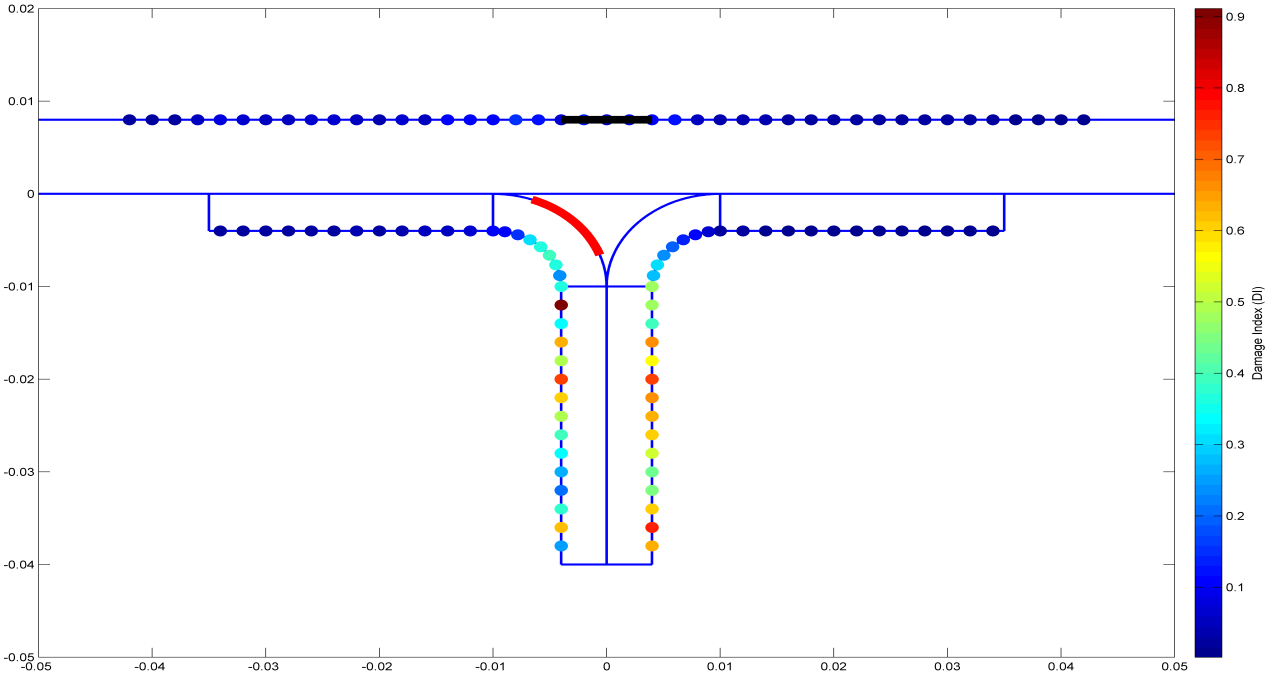

Figure 3.2.8: *Damage index for porosity, position (b), excitation in (2)*

Based on the results, the stringer proves to be less sensitive to porosity than to delaminations and inclusions. It is hard to draw any general conclusions since the results very much depend on the specified parameter combinations. Thorough discussions and concluding remarks are presented in section 3.2.2.

3.2.2 Discussion

The sensitivity analysis is justified by stringer attributes and wave propagation characteristics discussed in the previous section. It is also a means of analysing the stringer in a more engineering-like approach, where raw data is acquired and processed. Note that the main objective of the analysis is to investigate stringer sensitivity as a function of predefined parameters, rather than applying the concept to a SHM system. However, based on the obtained results, fundamental knowledge of stringer sensitivity is gained for a variety of damage types/positions and pitch-catch configurations which can be used in construction of SHM systems.

GUW in a 3D composite structure, such as the analysed stringer, are capable of damage detection for all tested defect types (delamination, inclusion and porosity). The stringer is less sensitive to porosity than to inclusions and delaminations. The modelling approach of porosity and inclusions may in fact be somewhat questionable, see section 4. A broadband signal is utilized in the sensitivity analysis in order to cover a wide frequency spectra, see section 2.2.1. The results show that the stringer sensitivity is highly correlated to the combination of tested parameters (damage type, damage position and excitation position). High sensitivity is in particular obtained for GUW-defect interactions in a perpendicular direction relative the damage. Simulations have been performed with low frequency, narrow band signals as well, and the results have shown that damage detection possibilities in general decreases for lower frequencies. This justifies the use of a broadband excitation, containing frequencies up 600 kHz.

A structural defect, e.g. a delamination, acts as a geometric boundary for a propagating wave. Unlike IP Lamb wave-defect interactions as those covered in the plate case study, structural defects in the 3D stringer can encounter GUW from all directions in space. In turn, wave scattering occurs in a 3D manner. Non-parallel interactions also prove to, generally speaking, affect the ultrasonic behaviour of the stringer in a more pronounced way. As an example, damages located at position (c) yield less structural changes than a defect located in (a) for a signal transmitted from position (2), see Figure 3.2.9.

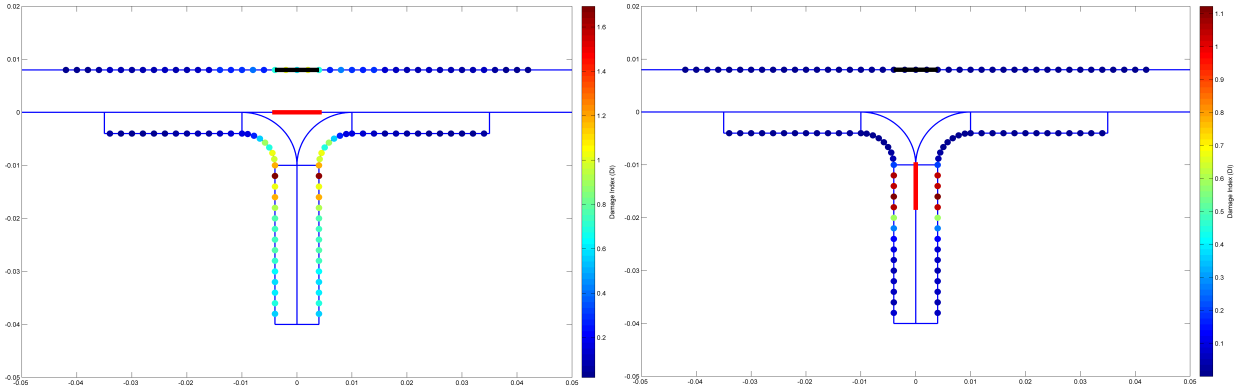

Figure 3.2.9: *Left: Excitation in (2), delamination in (a). Right: Excitation in (2), delamination in (c)*

Note that in Figure 3.2.9 (left), the entire left/right stringer section is affected by a delamination. This is not the case for a delamination at (c) (Figure 3.2.9 (right)), where only local effects are observed. It is concluded in section 2.6.3 that delaminations exposed to zero shear stress do not affect a propagating S_0 mode. Even though higher order modes are present in the case presented above, the same behaviour is observed. Stringer parts not adjacent to the defect prove to be more or less unaffected by the GUW-defect interaction presented in Figure 3.2.9 (right). In other words, no wave reflections tend to occur which has to be considered in an experimental SHM scenario.

The step-wise Newmark-β transient analysis is looped over 1000 time steps, with a step size of $3 \cdot 10^{-8}$ s. Only the first 500 steps are considered in the sensitivity analysis. The reason for not including all simulated steps in the calculation of the DI's is that the GUW, i.e. the acquired data, after a certain amount of time has been exposed to multiple scattering. The analysis primarily aims to examine the direct sensitivity of the stringer with minimized effects from multiple reflections (from boundaries). Meanwhile, a sufficient number of steps must be included such that the entire structure is occupied by GUW. Consequently, 500 time steps are included and regarded as a good compromise. This means that surface parts located far away from the excitation position naturally will result in a smaller sensitivity. On the other hand, high frequency damage detection (utilizing GUW) is defined as a local damage detection technique which means that the areas nearby the excitation are the most interesting in a SHM point of view.

3.3 Time Reversal Imaging

The four-step algorithm based on the TRP is a powerful tool for echo mode imaging. The stringer geometry is very different from a plate geometry. It inherits thickness variations and curvatures making the trajectory of the emitted wave hard to predict. ToF-based techniques are more or less impossible to implement in this context. Time reversal imaging, however, does not depend on the wave velocity and is therefore very handy for this geometry.

To emulate an experimental set-up, the nodes that are in contact with the PZT disc serve as the TRM. No PZT disc is modelled but the nodes will receive data independently of the neighbouring nodal displacements. The TRM has a width of 8 mm and is located on the top side above the Bermuda triangle. Further, the primary source is the node located at the centre of the TRM with a nodal displacement in the OOP direction (see Figure 3.3.1). To enable fast simulations and short processing time of the acquired signals, a cross-section of the 3D stringer model is analysed, i.e. one element and constrained DOFs in the y-direction.

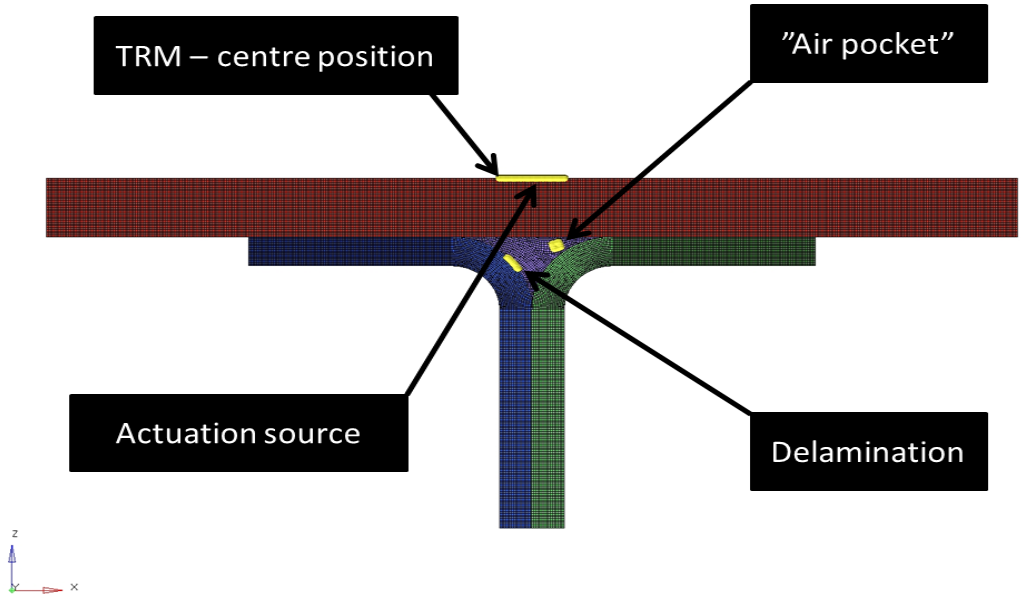

Figure 3.3.1: *TRM, actuation source and local defects in the stringer model.*

The element size is constant and set to 0.25 mm. The input signal is a 5.5 cycle tone burst modulated by the Hanning window with a central frequency of 500 kHz. The localization technique is tested for two types of damage: delamination and an ”air pocket”. The delamination is positioned between the bermuda triangle and the adjoining ply whereas the air pocket is located in the bermuda triangle itself. The model is also tested for different nodal distances in the TRM. The first configuration includes all nodes for data collection in the TRM. The second configuration only includes every fourth node in the TRM. This is designed to investigate the influence of aperture on the spatial resolution. Further, the time length of each simulation will be 300 and 1000 time frames respectively, with 0.1 μs /time frame. This equals 30 μs and 100 μs for each case.

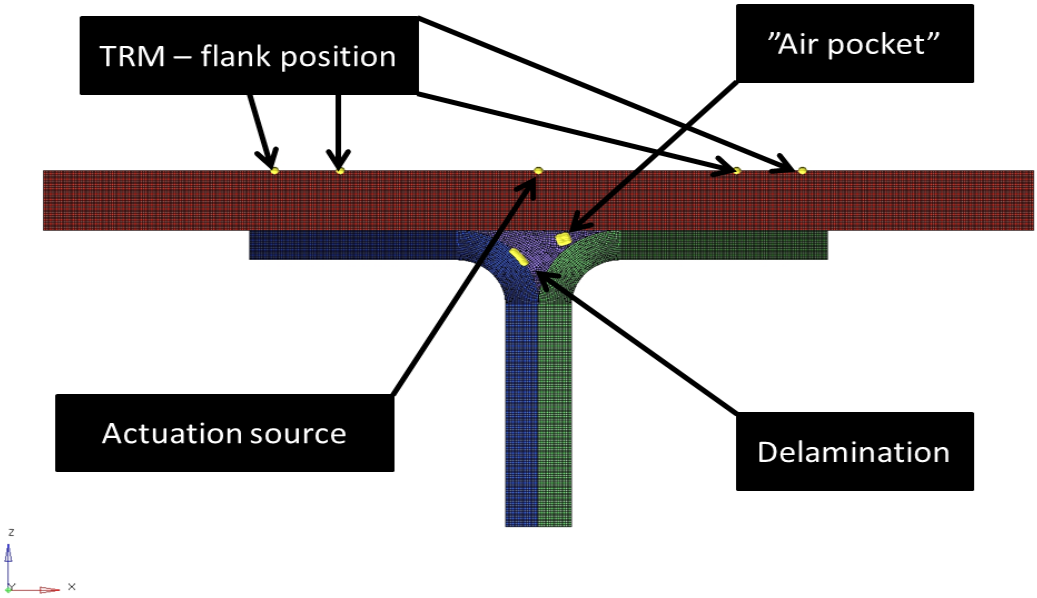

Figure 3.3.2: *TRM, actuation source and local defects in the stringer model.*

The PZT disc location might not be optimally placed precisely above the defect. Therefore, the TRM is set at two positions away from the middle of the stringer (see Figure 3.3.2). The shape of the TRM is different in that it only consists of two nodes for data collection. A PZT disc can only account for displacement change (or strain rate change) in one or two directions for the entire PZT. It is therefore not accurate to use each node under the PZT as individual data collector.

In summary the configurations tested, for air pocket damage and delamination, respectively, are:

1. TRM in centre location with every fourth node as data collector for 300 time frames
2. TRM in centre location with each node as data collector for 300 time frames
3. TRM in centre location with every fourth node as data collector for 1000 time frames
4. TRM in located on the flanks with only 2 nodes as data collector for 1000 time frames

Thus the position of the TRM, its aperture and the time period for data collection are three parameters that is taken under consideration. Further, the type of damage and the difference in response will be investigated.

3.3.1 Results

Air Pocket

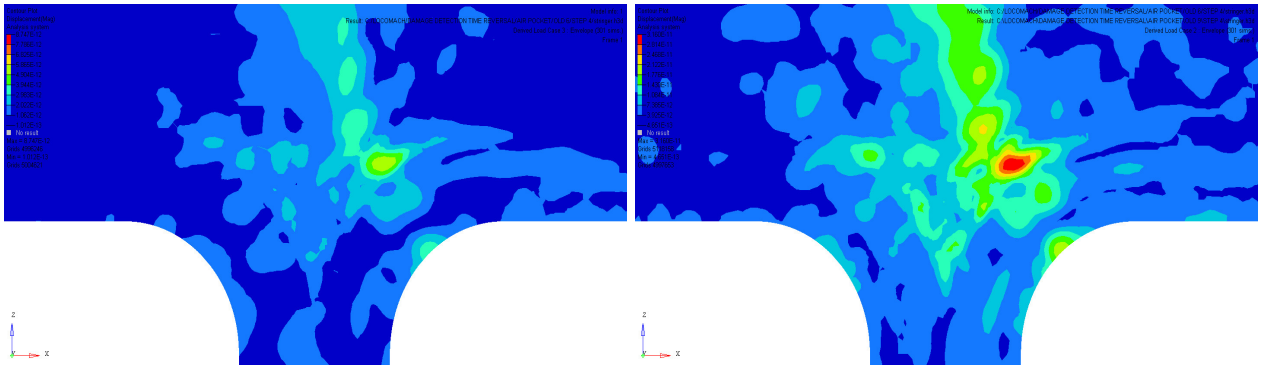

Figure 3.3.3: *Time reversal imaging for an air pocket. 300 time frames with every fourth node as data collector (left) and each node as data collector (right).*

The echo mode imaging for "air pocket"-type damage shows to have limited effect for 300 time frames. In contrast, when increasing the number of data collection nodes it is shown to have a positive effect and the damage can be pin-pointed (see Figure 3.3.3).

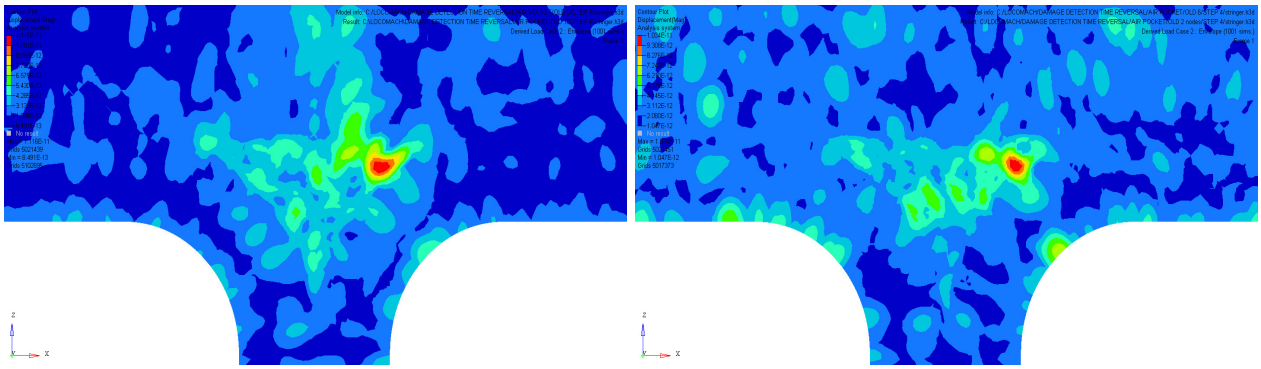

Figure 3.3.4: *Time reversal imaging for an air pocket. 1000 time frames TRM located in centre (left) and TRM located on the flanks (right).*

Longer time periods of data collection in the TRP have a positive effect on the result. By relocating the TRM to the flanks and adjusting its size (to two nodes) the result is continuing to display positive effects (see Figure 3.3.4).

Delamination

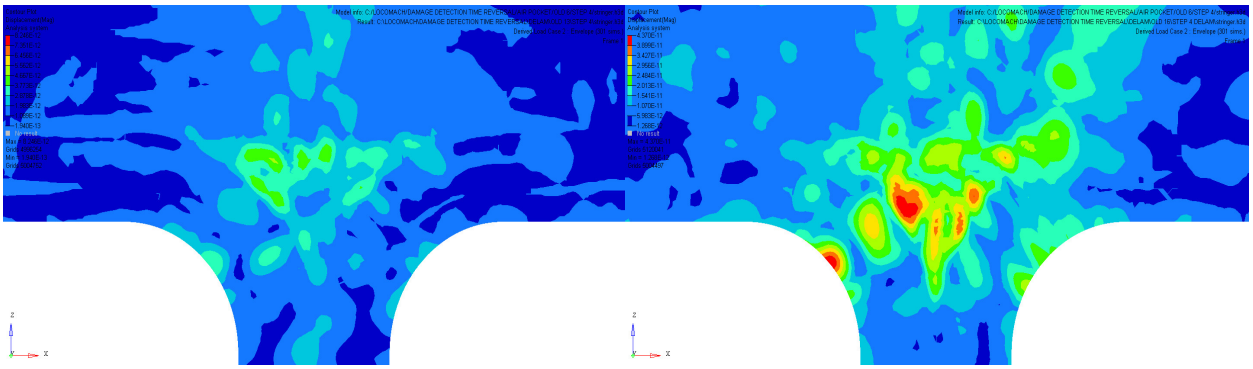

Figure 3.3.5: *Time reversal imaging for a delamination. 300 time frames with every fourth node as data collector (left) and each node as data collector (right).*

The echo mode imaging for delamination displays meagre quality for 300 time frames for both high and low aperture (see Figure 3.3.5). In the case for the high aperture TRM the displacement fields in the berumda triangle are high, but the high displacements are scattered and not concentrated to a point location.

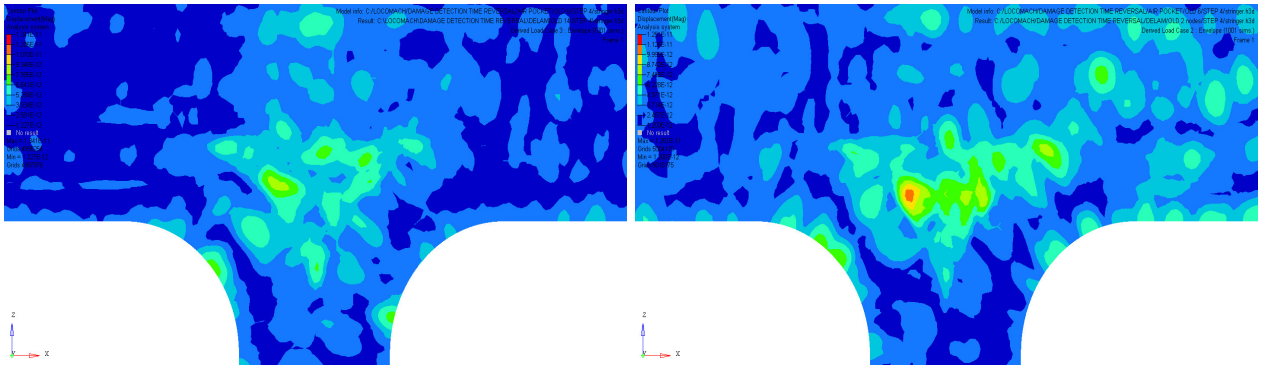

Figure 3.3.6: *Time reversal imaging for a delamination. 1000 time frames TRM located in centre (left) and TRM located on the flanks (right).*

Longer time periods of data collection in the TRP appear not to affect the result for the low aperture TRM with it being located in the centre. The result is poor and the defect location is hard to distinguish. When positioning the TRM on the flanks the result improves and the damage location can be distinguished (see Figure 3.3.6).

3.3.2 Discussion

Echo mode imaging has been performed for two types of damages: (1) air pocket and (2) delamination. The parameters that have been adjusted for each damage type to investigate the effects on the spatial resolution are: (1) the size of the TRM, (2) its position and (3) the length if the time period as previously discussed in section 3.3. A schematic is depicted in Figure 3.3.7 to illustrate the different simulations performed.

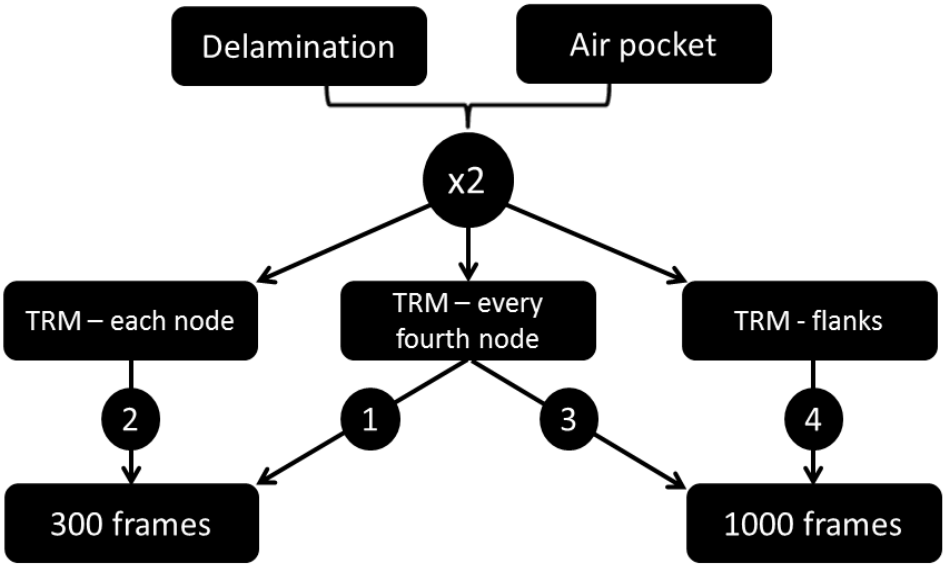

Figure 3.3.7: *Schematic of testing configurations.*

Time reversal imaging exhibits positive effect in terms of spatial resolution when the size of the TRM is increased. For instance, when "data-collecting" nodes increase in number, the spatial resolution improves. This is illustrated in Figure 3.3.3 and was reflected upon in section 2.6.4. Further, when the length of the time period used in the TRP increases, multiple scattering will occur when waves encounter with boundaries and the spatial resolution increases as a consequence. This can be seen by comparing Figure 3.3.3(left) to Figure 3.3.4 (left). Thus far the size of the TRM and the lenght of the time period show positive effects. It must be mentioned that the material itself can pose as a multiple scattering medium due to its composition of fibres and matrix. The different phases of materials can influence the propagating waves in a similar way as the boundaries. It has been shown that heterogeneous materials experience better results in spatial resolution compared to homogeneous materials when implementing time reversal techniques [34]. Whether this is the case for a composite stringer compared to an isotropic stringer remains to be tested.

When repositioning the TRM on the flanks and reducing the size of the TRM simultaneously the results are still very convincing. Through echo mode imaging it is still possible to pin-point the location of the damage, as illustrated in Figure 3.3.4 (right). Thus, repositioning the TRM might improve the spatial resolution. It is therefore not optimal to place the TRM precisely above the location of damage. Evidently, by placing the TRM on the flanks will give rise to improved multiple scattering and the spatial resolution increases, even in the case when the TRM is reduced to only two nodes.

What are the implications between different types of damage, i.e. how does delamination differ from the air pocket? It is apparent that delaminations do not scatter waves as efficiently as the air pocket when comparing the images. The inability to effectively scatter the waves makes the delamination a poor candidate for a secondary source in comparison to the air pocket. However, this result can prove useful in the damage identification process when evaluating what type of damage that is present in the structure. Different damages might have different refocusing point characteristics and this can be used to evaluate the type of damage.

4 Conclusions and Future Work

Two geometries have been studied: a laminate plate and a composite stringer. The latter was of main interest whereas the laminate provided the fundamental understanding of vibrational behaviour and Lamb wave propagation phenomena. Great effort was apportioned to the plate case and in retrospect this might not have been an ideal approach. Some of the theories surrounding Lamb waves in plates are not directly applicable in geometries such as the stringer. This is a restriction and many techniques can consequently not be implemented in the stringer. Nevertheless, the plate case served a valid purpose in determining the level of detail for the stringer in terms of element size and homogenization possibilities. A 2D model was initially constructed for the stringer, but since 2D plate theory does not account for through-thickness deformations (which occur in many multi – mode waves) it was soon omitted.

The evaluation of different plate models is considered essential for the efficiency of the project. Applying a non-homogenized approach to the stringer would have required an extreme amount of pre-processing and above all computational solving time. It would have been impossible to perform an extensive stringer investigation in such a short period of time, and with the dispersion curves at hand a homogenized structure proved to be adequate enough in terms of level of detail. Wave propagation does not exert the structure to any major deformations. if the structure had been subject to a static load or large deformations, e.g. during a modal analysis, then the homogenized model might not have sufficed. The plate model evaluation procedure required known dispersion curves, thus the numerical velocity estimations were necessary. In retrospect, an unnecessary amount of focus was directed to these estimations, and the Spectral Decomposition Technique with STFT should have been considered adequate enough.

The transmission of GUW in the plates as well as in the stringer is in some aspects questionable. For the generation of dispersion curves, pre-defined displacement patterns as those described in section 2.2.2 turned out to work well for some frequencies. However, problems were encountered above 400 kHz for symmetric excitations due to a rapid change in IP particle motions (high dispersion curve derivative). Nevertheless, good correlation was obtained between numerically estimated velocities and Lamb Toolbox outputs for A_0 which may justify the pre-defined displacement excitations. Regarding PZT disc modelling, only IP forces were applied. Expertise opinions [9] on the other hand have questioned this approach. Pure shear discs are commonly used in industry, with a large amount of energy concentrated to shear wave transmissions. Possibilities of OOP excitations (resulting in large energies for longitudinal wave generation) by utilizing probes (embedded PZT discs in a housing containing backing material) would therefore be interesting to investigate.

Delaminations were modelled in a sufficiently realistic way. Comparisons of results to the literature also confirmed this statement. Inclusion modelling on the other hand yields deficits that ought to be highlighted. In particular, the thickness of the modelled inclusion is unrealistically large (1 mm), and should at least be reduced to 0.25 mm. This will have effects in the sensitivity analysis when analysing inclusions, thus the high sensitivity observed may in fact be too high. Also the modelling of porosity could be improved. Composite stiffness properties are reduced based on the Mori-Tanaka theory as described in section 2.5.3. This is applicable for static conditions and low frequency excitations, but inherits limitations for higher frequencies (wave propagation), where the structural damping should be given a larger influence. Ultimately, visco-elastic damping can be applied, which should be considered in future work.

Global and local damage detection techniques are thoroughly investigated in section 2.6. In general, the low frequency (vibration based) analysis showed that global methods are very restricted, and that too many parameters (delamination size, IP location, and through-thickness location) have to coincide for a damage to be detectable. Nevertheless, the analysis resulted in a decision that vibration based techniques were to be omitted in the stringer analysis, thus the investigation is not conducted in vain. Wave reflection characteristics were also investigated, where relations between damage size and wave frequency content were confirmed. In addition, the analysis showed that asymmetric modes to a much larger extent possess the ability of damage detection. The analysis was valuable from an educational point of view, but did not yield any direct results that were later used in the stringer analysis (due to a much more complex geometry).

Time reversal imaging has proven to be a powerful tool for damage detection and localization. It displayed

positive results in tests performed on the stringer with varying efficiency when adjusting the TRM, its location and the time period. Although this method shows promise with the Finite Element Method it might have limitations in practical experiments. It remains a question whether PZT discs or other types of transducers, that represent the TRM, have the potential to refocus on the damage location. Further, the modelling of the PZT must be reviewed more closely. It can not be assumed that the nodes can remit the signal absent influence from the neighbouring nodes, as it has been in this thesis. Can several defects in the structure be located or does this method only show promise for single defect scenarios? How many PZT discs are required? These and other questions need to be considered in an experimental approach.

All analyses are performed on a cross-section of the stringer. This is obviously not ultimate in terms of accuracy in the results, but necessary due to lack of time. In an experimental SHM scenario, the third dimension must be taken into consideration. Therefore, analyses of full 3D models must be performed for more reliable results.

Optimal placements of the PZT discs is very important for the outcome of the time reversal techniques. Here, the sensitivity analysis might provide information for an optimal set-up of the transducers in order to reconstruct the damage through time reversal imaging with the highest spatial resolution possible.

For future work, a number of propositions are presented that ought to be given priority.

- Validation and calibration of stringer model.
- Validation and calibration of excitation and measurement procedure.
- Investigate the potential of OOP excitations using PZT probes.
- Combine sensitivity analysis results with further development of the time reversal imaging technique in order to optimize the spatial resolution in damage detection (numerically).
- Validation of the sensitivity analysis and time reversal imaging technique by an experimental investigation (experimentally).

A full 3D stringer model should be established based on a physical counterpart. A real stringer has unfortunately not been available at the time of this thesis, and therefore, no comparison was possible between the structural behaviour of the model and a physical stringer. Consequently, a system identification was not possible to carry out, which in other case would have brought further trust to the model. In particular, the damping of the model needs to be given additional consideration, thus a system identification could have served as a base for this in terms of model validation and calibration.

Also, as mentioned above, the modelling of PZT discs needs to be improved. The acquiring of data has been roughly simplified in this thesis. OOP measurements in a single node is not practicable in reality. In fact, PZT discs are often used as both signal transmitters and receivers. Hence, these discs covers an area which implies that not only one, but a number of node responses should be taken into consideration. Some sort of integration could for instance be performed over the area of the corresponding nodes. This is an important topic for future work.

Combining the time reversal imaging results with the observations made during the sensitivity analysis is of outermost interest. From the sensitivity analysis, a lucid overview of damage detection possibilities in the stringer was obtained. Numerous parameter combinations were examined and a fundamental understanding has been obtained in terms of GUW characteristics and how these interact with different types of damages. Consequently, for an arbitrary excitation position, knowledge was gained where an induced damage gave the highest sensitivity. This obtained information can be used when specifying the locations of the TRM's in the time reversal imaging procedure. This ought to be done on a numerical level prior to any experimental optimization procedure.

Finally, the sensitivity analysis and time reversal imaging technique should be validated to experimental data. This requires however that the model is validated as discussed above.

Bibliography

[1] K. Diamanti and C. Soutis. "Structural health monitoring techniques for aircraft composite structures". In: *Progress in Aerospace Sciences* 46 (2010), pp. 342–352.

[2] H. Speckmann and H. Roesner. "Proceedings of ECNDT, 9th European Conference on NDT, Berlin, Germany". In: *Structural Health Monitoring: A contribution to the Intelligent Aircraft Structure*. 2006.

[3] S. S. Kessler, S. M. Spearing, and C. Soutis. "Structural Health Monitoring in Composite Materials Using Lamb Wave Methods". In: *Progress in Aerospace Sciences* 46 (2010), pp. 342–352.

[4] H. Speckmann and H. Roesner. "Structural Health Monitoring: A contribution to the Intelligent Aircraft Structure". In: *Proceedings of ECNDT, 9th European Conference on NDT* (2006).

[5] H. T. Yolken and G. A. Matzkanin. "Recent Trends in Structural Health Monitoring Technologies". In: *AMMTIAC Quarterly* 3 (2009), pp. 3–6.

[6] SAAB. *EC RESEARCH PROJECT FOR LEAN AIRFRAM ASSEMBLY SYSTEMS*. Oct. 2012. URL: `http://www.saabgroup.com/en/About-Saab/Newsroom/Press-releases--News/2012---10/EC-research-project-for-lean-airframe-assembly-systems/`.

[7] US Venture Partners G. Arnold. *787 Fuselage Section*. Apr. 2009. URL: `http://geoffarnold.com/wp-content/uploads/2009/04/p1010272.jpg`.

[8] K. U. Schröder. *Stiffened composite aircraft fuselage shell with closed-profile hat-stringers*. 2010. URL: `http://ars.els-cdn.com/content/image/1-s2.0-S0263822310001480-gr1.jpg`.

[9] Linköping Sweden Dr. C. Mattei Creo Dynamics AB. Personal communication. 2012.

[10] J. L. Rose. *Ultrasonic Waves in Solid Media*. Cambridge University Press 1999, 1999. ISBN: 0-521-64043-1.

[11] J. L. P. Borges. *The Lamb Toolbox*. Aug. 2010. URL: `http://www.mathworks.com/matlabcentral/fileexchange/28367-the-lamb-toolbox`.

[12] NDT Education Resource Center. *NDT Resource Center*. 2001-2012. URL: `http://www.ndt-ed.org`.

[13] L. Wang and F.G. Yuan. "Group velocity and characteristic wave curves of Lamb waves in composites: Modeling and experiments". In: *Composites Science and Technology* 67 (2006), pp. 1370–1384.

[14] R. R. Craig Jr. and A. J. Kurdila. *Fundamentals of Structural Dynamics*. John Wiley & Sons, Inc., Hoboken, New Jersey, 2006. ISBN: 978-0-471-43044-5.

[15] B. D. Agarwal, L. J. Broutman, and K. Chandrashekhara. *Analysis and Performance of Fiber Composites, third edition*. John Wiley and Sons, Inc., 2006. ISBN: 978-0-471-26891-8.

[16] G. H. Staab. *Laminar Composites*. Butterworth-Heinemann, 1999. ISBN: 978-0-7505-7124-8, 0-7506-7124-6.

[17] X. Liu, C. Zhou, and Z. Jiang. "Damage localization in plate-like structure using built-in PZT sensor network". In: *Smart Strucures and Systems* 9 (2012), pp. 21–33.

[18] S. Gopalakrishnanl, M. Ruzzene, and S. Hanagud. *Computational Techniques for Structural Health Monitoring*. Springer-Verlag London Limited 2011, 2011. ISBN: 978-0-85729-284-1.

[19] N. Hu et al. "Locating Delamination in Composite Laminated Beams Using the A0 Lamb Mode". In: *Mechanics of Advanced Materials and Structures* 18 (2011), pp. 1–10.

[20] V. Giurfiutiu. "Tuned Lamb Wave Excitation and Detection with Piezoelectric Wafer Active Sensors for Structural Health Monitoring". In: *Journal of Intelligent Material Systems and Structures* 16 (2005), pp. 291–305.

[21] L. Draudviliene and L. Mazeika. "Investigation of the spectrum decomposition technique for the estimation of the group velocity Lamb waves". In: *ULTRAGARSAS (ULTRASOUND)* 64 (2009), pp. 13–16.

[22] L. Draudviliene and L. Mazeika. "Influence of the dispersion on measurement of phase and group velocities of Lamb waves". In: *ULTRAGARSAS (ULTRASOUND)* 64 (2009), pp. 18–21.

[23] C. A. Paget. "Active Health Monitoring of Aerospace Composite Structures by Embedded Piezoceramic Transducers". PhD thesis. Royal Institute of Technology SE-100 44, Stockholm, Sweden, 2001.

[24] S. Samanta and D. Datta. *Ultrasonic Detection of Inclusion Type Defect in a Composite Panel Using Shannon Entropy*. Tech. rep. Mechanical Engineering Department, Bengal Engineering and Science University, Shibpur.

[25] MATBASE a leap forward in material data. *Polymers: Engineering Polymers: PTFE*. 2009. URL: `http://www.matbase.com/`.

[26] J. Kastner et al. *Defect and Porosity Determination of Fibre Reinforced Polymers by X-ray Computed Tomography*. Tech. rep. Upper Austrian University of Applied Sciences.

[27] A. Kousourakis. “Mechanical Properties and Damage Tolerance of Aerospace Composite Materials Containing CVM Sensors”. PhD thesis. School of Aerospace, Mechanical, Manufacturing Engineering, College of Science, Engineering, and Technology, RMIT University.

[28] H. Huang and R. Talreja. “Effects of void geometry on elastic properties of unidirectional fiber reinforced composites”. In: *Composites Science and Technology* 65 (2005), pp. 1964–1981.

[29] W. Fan and P. Qiao. “Vibration-based Damage Identification Methods: A Review and Comparative Study”. In: *Structural Health Monitoring* 10 (2011), pp. 83–111.

[30] L. Tong Y. Zou and P. Steven. “Vibration-based model-dependent damaga (delamination) identification and health monitoring for composite structures - a review”. In: *Journal of Sound and Vibration* 230 (1999), pp. 357–378.

[31] H. Niemann et al. “Damage localization using experimental modal parameters and topology optimization”. In: *Mechanical Systems and Signal Processing* 24 (2010), pp. 636–652.

[32] T. Abrahamsson. *Calibration and Validation of Structural Dynamics Models*. Course literature in Structural Dynamics - Model Validation course, Chalmers University of Technology, Gothenburg, Sweden. Jan. 2012.

[33] C. Willberg et al. “The phenomenon of continous mode conversion of Lamb waves in CFRP plates”. In: *Key Engineering Materials* 518 (2012), pp. 364–374.

[34] M. Fink. “Time reversed Acoustics”. In: *Physics Today* 50(3) (1997), pp. 34–40.

[35] B. E. Treeby and B. T. Cox. *k-Wave: MATLAB toolbox for the simulation and reconstruction of photoacoustic wave-fields*. J. Biomed. Opt. vol. 15, no. 2, p. 021314, 2010.

[36] C. Prada, F. Wu, and M. Fink. “The iterative time reversal mirror: a solution to self-focusing in the pulse echo mode”. In: *JASA 90* (1991), 1119–1129.

[37] G. Derveaux, G. Papanicolaou, and C. Tsogka. “Time reversal imaging for sensor networks with optimal compensation in time”. In: *Journal of the Acoustical Society of America* 52 (2006), pp. 13–16.

[38] Morgan Technical Ceramics. *Guide to Piezoelectric & Dielectric Ceramic*. URL: `http://www.morganelectroceramics.com/resources/guide-to-piezoelectric-dielectric-ceramic/`.

[39] G. S. Bottai et al. *Damage Detection in Cryogenic Composites for Space Applications Using Piezoelectric Wafer Active Sensors*. Tech. rep. American Institute of Aeronautics and Astronautics.

[40] N. Dominguez, B. Mascaro, and V. Gibiat. “Method of imaging using topologic energy calculations”. Patent US 7,654,142 B2 (US). Feb. 2010. URL: `http://patft.uspto.gov/netacgi/nph-Parser?Sect2=PTO1&Sect2=HITOFF&p=1&u=/netahtml/PTO/search-bool.html&r=1&f=G&l=50&d=PALL&RefSrch=yes&Query=PN/7654142`.

A APPENDIX - Stress and strain transformation matrices

$$[T_\epsilon] = \begin{bmatrix} \cos^2\theta & \sin^2\theta & 0 & 0 & 0 & \cos\theta\sin\theta \\ \sin^2\theta & \cos^2\theta & 0 & 0 & 0 & -\cos\theta\sin\theta \\ 0 & 0 & 1 & 0 & 0 & 0 \\ 0 & 0 & 0 & \cos\theta & -\sin\theta & 0 \\ 0 & 0 & 0 & \sin\theta & \cos\theta & 0 \\ -2\cos\theta\sin\theta & 2\cos\theta\sin\theta & 0 & 0 & 0 & \cos^2\theta - \sin^2\theta \end{bmatrix} \tag{A.0.1}$$

$$[T_\sigma] = \begin{bmatrix} \cos^2\theta & \sin^2\theta & 0 & 0 & 0 & 2\cos\theta\sin\theta \\ \sin^2\theta & \cos^2\theta & 0 & 0 & 0 & -2\cos\theta\sin\theta \\ 0 & 0 & 1 & 0 & 0 & 0 \\ 0 & 0 & 0 & \cos\theta & -\sin\theta & 0 \\ 0 & 0 & 0 & \sin\theta & \cos\theta & 0 \\ -\cos\theta\sin\theta & \cos\theta\sin\theta & 0 & 0 & 0 & \cos^2\theta - \sin^2\theta \end{bmatrix} \tag{A.0.2}$$

B APPENDIX - Eigenfrequencies and MAC results

Table B.0.1: Eigenfrequencies for different delamination sizes in Hertz [Hz]

	Undamaged	4x4 mm	8x8 mm	16x16 mm	24x24 mm	$\Delta f_{24x24mm}$
Mode 1	510.86	510.86	510.86	510.85	510.81	0.05
Mode 2	1000.4	1000.4	1000.4	1000.3	1000.2	0.18
Mode 3	1083.6	1083.6	1083.5	1083.5	1083.4	0.18
Mode 4	1481.6	1481.6	1481.6	1481.5	1480.4	1.24
Mode 5	1793.4	1793.4	1793.4	1793.3	1792.6	0.76
Mode 6	1979.8	1979.8	1979.8	1979.8	1977.8	2.04
Mode 7	2193.2	2193.2	2193.2	2192.9	2169.6	23.62
Mode 8	2325.3	2325.3	2325.3	2325.1	2284.8	40.53
Mode 9	2851.8	2851.8	2851.8	2851.8	2347.9	503.91
Mode 10	2939.9	2939.9	2939.9	2939.3	2851.3	88.62
Mode 11	3170	3169.9	3169.9	3169.2	2942.9	227.01
Mode 12	3218	3218	3218	3217.8	3063.2	154.81
Mode 13	3475.8	3475.8	3475.7	3474.1	3166.9	308.89
Mode 14	3858.4	3858.4	3858.4	3857.9	3221.4	637.09
Mode 15	4047.9	4047.9	4047.8	4046.7	3469.1	578.81
Mode 16	4160	4160	4160	4159.8	3858.6	301.44
Mode 17	4494.5	4494.5	4494.4	4493.4	4043	451.42
Mode 18	4634.6	4634.6	4634.5	4632.6	4160.5	474.07
Mode 19	4848.7	4848.7	4848.7	4848.4	4495.2	353.50
Mode 20	4916.4	4916.4	4916.2	4911.1	4626.1	290.34

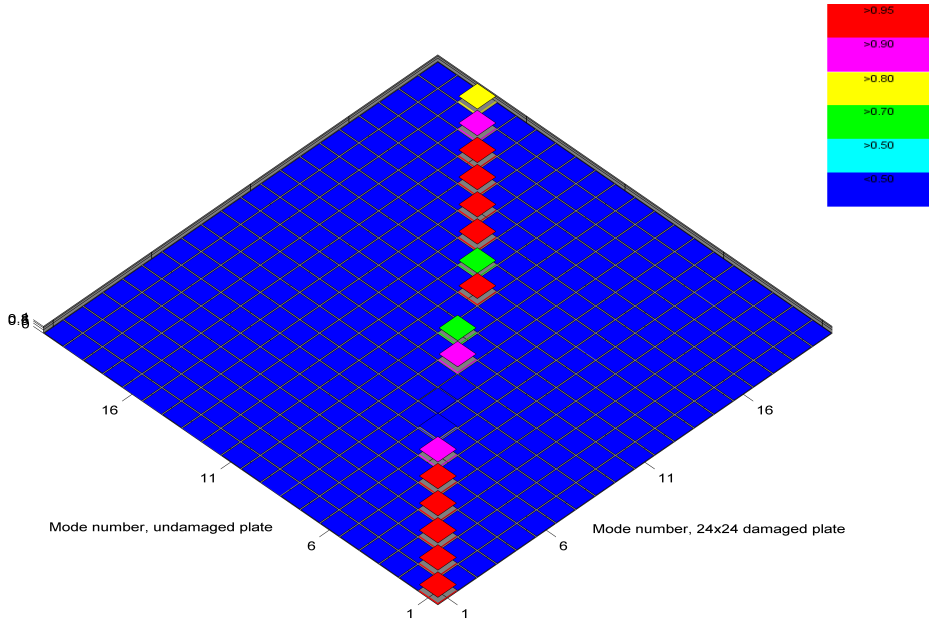

Figure B.0.1: *Visual representation of MAC matrix entities*

Table B.0.2: Eigenfrequencies for different through-thickness delamination locations in Hertz [Hz]. Delamination size equals 24×24 mm.

	Undamaged	z = 1.04 mm	z = 1.43 mm	z = 1.95 mm
Mode 1	510.86	510.64	510.66	510.81
Mode 2	1000.4	999.61	999.68	1000.2
Mode 3	1083.6	1083.1	1083.2	1083.4
Mode 4	1481.6	1480.6	1480.6	1480.4
Mode 5	1793.4	1792.1	1792.5	1792.6
Mode 6	1979.8	1978.6	1978.9	1977.8
Mode 7	2193.2	2190.8	2191.2	2169.6
Mode 8	2325.3	2321.4	2322.2	2284.8
Mode 9	2851.8	2843.8	2846.9	2347.9
Mode 10	2939.9	2932.8	2933.2	2851.3
Mode 11	3170	3158.8	3160.5	2942.9
Mode 12	3218	3198.4	3205.2	3063.2
Mode 13	3475.8	3451.3	3453.5	3166.9
Mode 14	3858.4	3834.8	3839.7	3221.4
Mode 15	4047.9	4023.6	4028.3	3469.1
Mode 16	4160	4145.3	4150	3858.6
Mode 17	4494.5	4461.6	4471.3	4043
Mode 18	4634.6	4612.8	4614	4160.5
Mode 19	4848.7	4834.2	4835.3	4495.2
Mode 20	4916.4	4874.7	4879	4626.1

Table B.0.3: Eigenfrequencies for different delamination locations in xy-plane in Hertz [Hz]. Delamination size equals 24×24 mm.

	Undamaged	x = 0.02 m	x = 0.06 m	x = 0.1 m
Mode 1	510.86	510.61	510.76	510.47
Mode 2	1000.4	999.97	999.58	999.06
Mode 3	1083.6	1083.2	1081.7	1083.4
Mode 4	1481.6	1480.7	1474.1	1481.3
Mode 5	1793.4	1793.3	1791.5	1787.4
Mode 6	1979.8	1977.9	1973.5	1962.1
Mode 7	2193.2	2183	2132.6	2167.8
Mode 8	2325.3	2220.5	2277.2	2203.4
Mode 9	2851.8	2330.6	2343.7	2385
Mode 10	2939.9	2851.8	2851.5	2851.1
Mode 11	3170	2940.4	2941.6	2949.1
Mode 12	3218	3158	3151.1	3160.3
Mode 13	3475.8	3171.6	3168.9	3167.7
Mode 14	3858.4	3218.6	3227.6	3218.3
Mode 15	4047.9	3475.5	3473.1	3471.2
Mode 16	4160	3858.8	3858.1	3859.8
Mode 17	4494.5	4047.5	4046.4	4045.3
Mode 18	4634.6	4160	4160.8	4161.6
Mode 19	4848.7	4494.5	4495.9	4494.4
Mode 20	4916.4	4633	4634	4634.4